

**POLYMERS FOR PASSIVE TUMOR TARGETING:
A CONTRIBUTION TO ENLIGHTEN THE EFFECT OF
POLYMER NATURE AND ARCHITECTURE ON THE
BIODISTRIBUTION**

Dissertation

zur Erlangung des
Doktorgrades der Naturwissenschaften (Dr. rer. nat.)

der

Naturwissenschaftlichen Fakultät I – Biowissenschaften –

der Martin-Luther-Universität
Halle-Wittenberg

vorgelegt

von Herrn Dipl.-Pharm. Stefan Hoffmann
geb. am 15. November 1984 in Halle

Gutachter:

1. Prof. Dr. rer. nat. habil. Karsten Mäder
2. Prof. Dr. med. habil. Oliver Thews
3. Prof. Ing. Karel Ulbrich, DrSc.

Datum der öffentlichen Verteidigung: 07.05.2014

***Scientific progress is always
evolution and rarely revolution.***

Ruth Duncan, Maria J. Vicent¹

Table of Content

Table of Content	C
List of Abbreviations.....	E
German Summary.....	G
Preface	J
1 Introduction.....	1
1.1 Cancer and Cancer Therapy.....	1
1.2 The EPR-Effect.....	4
1.3 Polymer Therapeutics	5
1.3.1 Polymers in Cancer Therapy.....	6
1.4 Imaging of Cancer.....	7
1.4.1 Fluorescence Imaging.....	8
1.5 Aims and Objectives	10
2 Experiments	11
2.1 Materials	11
2.1.1 Origin of Polymer Precursors	11
2.1.2 Fluorescence Dyes	11
2.1.3 Origin and Specifications of Animals	12
2.2 Methods.....	13
2.2.1 Conjugation Chemistry.....	13
2.2.2 Lyophilization	14
2.2.3 ¹ H-NMR-Spectroscopy.....	15
2.2.4 Particle Size and Molecular Weight Distribution	15
2.2.5 <i>In Vitro</i> Toxicity Experiments.....	17
2.2.6 Multispectral Fluorescence Imaging	19
2.2.7 <i>In Vivo</i> Experiments and Animal Care.....	22
2.2.8 Therapy Study	24
2.2.9 Histology.....	25
2.2.10 Confocal Laser Scanning Microscopy (CLSM)	26
3 Results and Discussion.....	27
3.1 HPMA Copolymers (OPB Spacer)	27
3.1.1 Synthesis of Dual Fluorescent HPMA Copolymers with pH-Sensitive Drug Release (OPB-Spacer) and Physicochemical Characterization	28
3.1.2 Optimization of Measurement Settings.....	30
3.1.3 Biodistribution and Elimination in Mice	32
3.1.4 <i>Ex Vivo</i> Fluorescence Imaging: Extracted Organs	35
3.1.5 Characterization of Kidney Accumulation	36
3.1.6 Tumor Accumulation Studies (<i>In Vivo</i>)	40
3.1.7 Characterization of the Tumor Accumulation <i>Ex Vivo</i>	49
3.1.8 Summary	54

3.2	HPMA Copolymers with Modified Release Rate.....	55
3.2.1	Synthesis of Dual-Fluorescent HPMA Copolymers with Modified Release Rate of a pH-Sensitive Drug model.....	55
3.2.2	<i>In Vivo</i> Characterization in Tumor-Bearing Mice	56
3.2.3	<i>Ex Vivo</i> Fluorescence Imaging of Autopsied Organs.....	64
3.2.4	Summary	65
3.3	HPMA Copolymers: Therapy Study.....	67
3.4	Carbohydrate Plasma Volume Expanders.....	71
3.4.1	<i>In Vitro</i> Cytotoxicity and Immunogenicity.....	72
3.4.2	Synthesis of NIR-Fluorescent Polymer-Dye Conjugates	74
3.4.3	Particle Size and Molecular Weight Distribution	77
3.4.4	Biodistribution and Elimination Studies	79
3.4.5	Tumor Accumulation Studies	82
3.4.6	Summary	85
3.5	Polymers from Glutamic Acid (PGA)	87
3.5.1	Characterization of Molecular Weight Distribution	88
3.5.2	Hemolytic Activity Assay	91
3.5.3	Synthesis of NIR-Fluorescent PGA-Dye Conjugates.....	91
3.5.4	Biodistribution and Elimination in Mice: TB-PGA-200.....	93
3.5.5	TB-PGA-200: Tumor Accumulation.....	96
3.5.6	Tumor Accumulation: Variation of PGA Structures.....	98
3.5.7	Summary	101
4	Summary and Perspectives	102
5	Appendix	I
5.1	List of Chemicals, Reagents and Solvents	I
5.2	References	II
5.3	Publications	XXI
5.3.1	Peer Reviewed Articles	XXI
5.3.2	Quotable Abstracts	XXI
5.3.3	Conference Contributions	XXII
5.4	Acknowledgements.....	XXIV
5.5	Curriculum Vitae	XXVI
5.6	Declaration of Original Authorship.....	XXVII

List of Abbreviations

^{18}F FDG	^{18}F -fluorodesoxyglucose
AF4	Asymmetric flow field-flow fractionation
AGU	Anhydrous glucose unit
CCD	Charge-coupled device sensor
CLSM	Confocal laser scanning microscopy
CRC	Colorectal cancer
CT	Computed x-ray tomography
DEX	Dextran
DLS	Dynamic light scattering
DMF	Dimethylformamide
DNA	Deoxyribonucleic acid
DOX	Doxorubicin
EDCI	1-Ethyl-3-(3-dimethylaminopropyl)carbodiimide
Em	Emission maximum
EMA	European Medicines Agency
EPR	Enhanced permeability and retention
EtOH	Ethanol
Ex	Excitation maximum
FDA	U.S. Food and Drug Administration
FI	Fluorescence intensity
FLI	Fluorescence Imaging
FR	Far red
GPC	Gel permeation chromatography
HA	Hyaluronic acid
HCl	Hydrochloric acid
HE	Haematoxylin and eosin
HER-2	Human epidermal growth factor receptor 2
HES	Hydroxyethyl starch
HPMA	N-(2-hydroxypropyl)-methacrylamide
i.p.	Intraperitoneally (injection)
i.v.	Intravenously (injection)
IFP	Interstitial fluid pressure
IL	Interleukin
IPB	4-isopropyl-4-oxobutyric acid
LCTF	Liquid crystal tunable filter
LPS	Lipopolysaccharide
MALLS	Multi angle laser light scattering
MEM	Minimum essential medium
M_n	Number-averaged molecular weight
MP	Megapixels

MRI	Magnetic resonance imaging
MTD	Maximum tolerated dose
MTT	3-(4,5-Dimethylthiazol-2-yl)-2,5-diphenyltetrazoliumbromide
M_w	Weight-averaged molecular weight
MW	Molecular weight
MWCO	Molecular weight cut off
M_z	Z-average mean square diameter weighted molecular weight.
NHS	N-Hydroxysuccinimide
NIR	Near infrared
NMR	Nuclear magnetic resonance
Nude Fox	Hs1Cpb:NMRI- <i>Foxn1</i> ^{nu/nu} from Harlan Winkelmann
OI	Optical imaging
OPB	4-(2-oxopropyl)benzoic acid
p.i.	post injectionem
PAMAM	Poly-amidoamine
PBMCs	Peripheral blood mononuclear cells
PBS	Phosphate buffered saline
PCS	Photon correlation spectroscopy
PDI	Polydispersity index
PEG	Polyethylene glycol
PES	Polyethersulfone
PET	Positron emission tomography
PGA	Polyglutamic acid
PVE	Plasma volume expander
Px	Pixel
PYR	4-oxo-4-(2-pyridyl)butyric acid
RAFT	Reversible addition fragmentation chain transfer polymerization
RBC's	Red blood cells
RC	Regenerated cellulose
RES	Reticuloendothelial system
R_H	Hydrodynamic radius
RI	Refractive index
ROI	Region of interest
s.c.	Subcutaneously (injection)
SD	Standard deviation
SKH1	SKH1- <i>Hr</i> ^{hr} from Charles River Lab
SNR	Signal to noise ratio
SPECT	Single photon emission spectroscopy
TAV	Tumor accumulation value
TNF	Tumor necrosis factor
VEGF	Vascular endothelial growth factor

German Summary

Polymerkonjugaten als Arzneiform zur gezielten Tumorthherapie gilt in der medizinischen Forschung ein besonderes Interesse, jedoch ist bisher der Zusammenhang zwischen Polymerstruktur, Molekulargewicht und dem Geschehen im lebenden Organismus immer noch nicht genau verstanden. Diese Arbeit leistet einen Beitrag zum Verständnis dieses Zusammenhangs. Dazu wurden drei strukturell unterschiedliche Polymerklassen untersucht um einen geeigneten Kandidaten für die zielgerichtete Tumorthherapie basierend auf dem EPR-Effekt zu finden: HPMA-Copolymere, Kohlenhydrate und Polyglutamate. Die Molekulargewichtsverteilung wurde genau bestimmt und mögliche Bedenken hinsichtlich der Toxizität wurden experimentell untersucht. Einige Polymere aus jeder Klasse wurden mit besonderem Augenmerk auf die Verteilung und Elimination *in vivo* in Nacktmäusen untersucht. Dafür wurden fluoreszenzmarkierte Polymere verwendet, die entweder von Kooperationspartnern bereitgestellt wurden (HPMA-Copolymere) oder aber im Rahmen dieser Arbeit selbst fluoreszenzmarkiert wurden (Kohlenhydrate und Polyglutamate).

Die Beurteilung der Verteilung aller Polymere im Körper wurde durch nicht-invasive nahinfrarote multispektrale Fluoreszenztomographie ermöglicht. Das beobachtete Verteilungsmuster war vor allem abhängig von der verwendeten Polymerklasse, aber weniger vom Molekulargewicht oder der Polymerarchitektur. So akkumulierten HPMA-Copolymere vor allem in den Nieren, wohingegen die Kohlenhydrate eine leichte Akkumulation in der Leber und den Lymphknoten zeigten. Die Polyglutamate reichert sich spezifisch im Knochen und Knorpel an, was möglicherweise im Hinblick auf die Entwicklung von Arzneiformen zur gezielten Anreicherung im Knochengewebe interessant sein könnte. Trotz aller Unterschiede zeigte bis auf Dextran keines der untersuchten Polymere eine ausgeprägte Akkumulation in der Leber, wie es beispielsweise für Nanopartikel oder Nanokapseln oft beobachtet wird. Zweifellos scheint dies ein großer Vorteil von wasserlöslichen Polymeren zu sein, da die Gefahr einer möglichen Hepatotoxizität minimiert wird und die Verweildauer eines potentiellen Wirkstoffs im Blut erhöht wird. Ebenso zeigte keines der untersuchten Polymere eine spezifische lokale Akkumulation in den Ovarien, die kürzlich für nanopartikuläre Arzneiformen berichtet wurde.

Die Kohlenhydrate und Polyglutamate wurden jeweils mit einem Fluoreszenzfarbstoff konjugiert um die Eigenschaften im Körper zu untersuchen, wohingegen die HPMA-

Copolymere von Kooperationspartnern mit zwei verschiedenen Fluoreszenzfarbstoffen mit unterschiedlichen Emissionsspektren konjugiert wurden. Ein Farbstoff dient dabei als ein nicht-abspaltbarer Marker des Polymers und der andere stellt ein Modell für einen pH-abhängig abspaltbaren Wirkstoff dar. Auf diese Weise war es möglich, die Verteilung des Polymers und des Wirkstoffmodells gleichzeitig mit multispektraler Fluoreszenztomographie zu beobachten. Nachdem Verteilung und Elimination charakterisiert worden waren, wurde die aufgrund des EPR-Effekts vermutete Tumorakkumulation in Mausmodellen humaner Kolonkarzinom-Xenografttumoren gezeigt. Wie schon die Verteilung zuvor, konnte auch die Akkumulation in den Tumormodellen hervorragend mittels Fluoreszenztomographie dargestellt werden. Interessanterweise haben sich alle untersuchten Polymere in den Tumormodellen angereichert. Die Anreicherung in den DLD-1-Tumoren war immer besser als in den HT-29-Tumoren, was der gesteigerten Wachstumsrate und der damit verbundenen Tumormikrostruktur zugeschrieben werden kann, die histologisch nachgewiesen wurde. Am Beispiel von unterschiedlichen HPMA-Copolymeren wurde mittels Fluoreszenztomographie *in vivo* nachgewiesen, dass eine Freisetzung des fluoreszierenden Wirkstoffmodells von den HPMA-Copolymeren durch die chemische Umgebung des Spacers beeinflusst werden kann.

Eine bedeutende Herausforderung bei der optischen Bildgebung ist die schwierige Quantifizierbarkeit der Daten. Dabei müssen einige Effekte, wie beispielsweise Streuung, Absorption, Autofluoreszenz und Quenching in Betracht gezogen werden. Quenching-Effekte sind in komplexen Matrices oder *in vivo* nur sehr schwer vorherzusehen. Es erwies sich daher als unmöglich aus den gemessenen Fluoreszenzintensitäten *in vivo* Konzentrationen zu berechnen. Die Tumoranreicherung wurde in dieser Arbeit dennoch quantifiziert, nachdem dafür ein relativer Ansatz entwickelt worden war. Somit konnte die Tumoranreicherung von verschiedenen Polymeren und verschiedenen Mäusen verglichen werden. Prinzipiell stellt sich natürlich die Frage, ob die Fluoreszenztomographie eine geeignete Methode zur Charakterisierung von Polymeren *in vivo* ist, da die Eigenschaften dieser durch die verwendeten Farbstoffe verändert werden können, insbesondere bei den eher niedermolekularen Polyglutamaten und dem linearen HPMA-Copolymer. Dies kann sicherlich als Nachteil der Methode angesehen werden und die Ergebnisse dieser Arbeit sollten daher in weiteren Untersuchungen mit anderen bildgebenden Verfahren, wie zum Beispiel MRI oder CT verifiziert werden. Dennoch zeichnet sich die multispektrale

Fluoreszenztomographie als einfache und preiswerte Methode aus, was sie speziell für Screening-Untersuchungen in der präklinischen Anwendung sehr wertvoll macht.

Die vielversprechenden Ergebnisse der Tumoranreicherungsuntersuchungen mit HPMA-Copolymeren mündeten schließlich in eine Therapiestudie mit einem Doxorubicin-konjugiertem HPMA-Copolymer in Xenograft-Tumormäusen. Obwohl das humane Kolonkarzinom-Tumormodell in dieser Studie therapieresistent gegenüber Doxorubicin war, konnte eine verbesserte Wirksamkeit und reduzierte Toxizität des Polymerkonjugats im Vergleich zu freiem Doxorubicin nachgewiesen werden. Die Ergebnisse dieser explorativen Studie müssen jedoch durch weitere Untersuchungen in anderen Tumoren bestätigt werden. Aufgrund des längeren Beobachtungszeitraums sind Tumormodelle mit geringerer Wachstumsgeschwindigkeit dafür empfehlenswert. Es muss betont werden, dass die subkutanen Tumormodelle in dieser Arbeit einfach zu messen und zu beobachten sind, aber nur eine geringe klinische Relevanz haben. Twan Lammers kommentierte subkutane Tumormodelle auf der European Summerschool of Nanomedicine 2011 in Wittenberg mit der Aussage (übersetzt aus dem Englischen): „Niemand stirbt an einem lokalen soliden Tumor, denn diese würden einfach durch eine Operation entfernt werden. Die Menschen sterben an den Metastasen.“ Vor diesem Hintergrund müssen die Ergebnisse dieser Arbeit in klinisch relevanteren orthotopen und metastasierenden Tumormodellen, die realistischere biologische Eigenschaften wie Vaskularisierung und Infiltration widerspiegeln, bestätigt werden.

Im Rahmen dieser Arbeit zeigten sich Hinweise, dass eine Mehrfach-Applikation zu höherer Tumoranreicherung führen kann. Dieser Effekt sollte in nachfolgenden Arbeiten weitergehend untersucht werden. Ein Punkt der im Zusammenhang dieser Arbeit nicht experimentell untersucht wurde, ist die Aufnahme der Polymerkonjugate in die Tumorzellen. Die Prinzipien der Wirkstofffreisetzung basieren meist auf intrazellulären Mechanismen, wie zum Beispiel der Abspaltung in den Endosomen. Die Polymerkonjugate müssen daher zunächst in die Zellen aufgenommen werden. Es wird aber nicht alles mit einer Größe im Nanometerbereich automatisch von Tumorzellen internalisiert. Diese würden sonst zum Beispiel mit Plasmaproteinen aus dem Blut überflutet werden. Daher sollten weitere Studien unternommen werden, welche die Aufnahme der verschiedenen Polymere in die Zellen mit Inkubationsexperimenten nachweisen und den genauen Mechanismus untersuchen.

Preface

The scientific work which is presented in this thesis covered three subprojects: First, the cooperation with the Institute of Macromolecular Chemistry in Prague (Czech Republic) about HPMA copolymers. Second, the project about carbohydrate polymers, and third, the cooperation with the CIPF in València (Spain) about polymers from polyglutamic acid.

The focus of this work was on preclinical *in vivo* experiments in rodents. For that reason, extensive *in vitro* toxicity experiments, which always have to precede preclinical animal studies, have been either laid into the responsibility of the cooperation partners or – if conducted within this work in own responsibility – have been limited to a necessary minimum. All *in vivo* experiments complied with regional regulations and guidelines and were approved by the local authority in Saxony-Anhalt.

Owing to the variety of polymers investigated in this study, the groups were limited to three-four animals in most cases. Although not tested with the small number of animals, Gaussian distribution was assumed and the results were calculated as means. Taking the lower statistical power of small groups into account, the range was used as error bars instead of the usually applied standard deviation, unless it was stated otherwise.

Several parts of this thesis have been published previously in peer-reviewed articles in leading scientific journals. These parts have been adequately cited and referenced at the beginning of the respective chapters.

1 Introduction

1.1 Cancer and Cancer Therapy

Cancer has become one of the most common causes of death in the world with an estimated number of 7.6 million cancer deaths in 2008.²⁻⁴ A particular high incidence can be found in the developed countries, whereas the highest mortality is reported for the developing countries.³ About half of the cancer prevalence burden is ascribed to the most developed areas of the world, representing only one sixth of the world's population.⁵ The latest WHO world statistics report an increasing number of cancer morbidity and mortality with 14.1 million new cancer cases and 8.2 million cancer related deaths in 2012.⁶ Solely in Germany, about 450,000 – 500,000 people get cancer every year and one quarter of all deaths are ascribed to cancerous diseases, which were 216,000 people in 2009.⁷ Thus, cancer is the second most common cause of death in Germany, outnumbered only by cardiovascular diseases.^{7,8} The most common types of cancer were reported to be breast cancer (woman) and prostate cancer (men) followed gender-independently by colorectal cancer.^{3,7,9} Cell lines from colorectal cancer were chosen as tumor model in this thesis. The prevalence of cancer and the number of cancer associated deaths are steadily increasing, which can be explained with generally increased life expectancy, improved diagnostics and more successful therapy of other diseases, e.g. stroke or myocardial infarction.^{10,11} For 2015, a total of 220,000 cancer deaths per year are expected in Germany.¹² The high number of patients in combination with the disease's seriousness and expensive therapies is an enormous economic burden. The total costs to the economies of the European Union caused by cancer are estimated to be € 117 billion per year (including therapy costs, lost earnings and premature mortality).¹³ Thus, tremendous efforts are made to develop new cancer therapies resulting in 29 new cancer drug approvals by the European Medicines Agency (EMA) for use in Europe in the years 2006 – 2011.¹⁴ Solely in the last two years, 21 new oncology drugs were approved by the U.S. Food and Drug Administration (FDA) for use in the USA.^{15,16} However, cancer mortality is still high and there are certain types of cancer with very poor prognosis (e.g. pancreatic cancer, glioblastoma multiforme and stomach cancer).^{9,17}

Development of Cancer

The fundamental cause of cancer is continuous and unregulated cell division.¹⁸ Several factors have been identified to increase the risk for developing cancer.¹⁹ Amongst others, most certainly correlated cancer risks are radiation,²⁰⁻²² smoking,²³⁻²⁶ nutrition and obesity,^{27,28} and infectious diseases caused by oncoviruses like hepatitis C virus²⁹ or the human papilloma virus.³⁰ All of these risks share the property to lead – directly or mediated – to alterations in the genetic code of the DNA in cells. Indeed, genetic alterations in multiple genes of the cancerous cells are the reason for the pathologic unregulated cell growth.^{18,31} These alterations can basically occur in every tissue and cell type, leading to a broad variety of cancers. The type of cancer developed from these altered cells is particularly dependent on the genes affected and on following genetic mutations influencing the properties of the cells. *Hanahan* and *Weinberg* describe several hallmarks which need to be fulfilled to develop malignant cancer: sustaining proliferative signaling, evading growth suppressors, activating invasion and metastasis, enabling replicative immortality, inducing angiogenesis, resisting cell death, reprogramming energy metabolism and evading the immune system.^{32,33} The tumors being formed from proliferative cells exhibiting these hallmarks are highly complex and interact with other cells like fibroblasts, endothelial cells and leucocytes, which are involved in the tumor biology and structure.³⁴ A more detailed insight into the development of cancer is certainly beyond the scope of this thesis and – as far as it is understood yet – cancer genesis has been described comprehensively in literature previously.^{32,33}

Cancer Therapy

Cancer therapy basically aims at the removal of cancerous cells, whereas for a lasting therapy success all cancer cells have to be effectively removed, killed or kept dormant. The central pillars of cancer treatment are surgery, radiation therapy and chemotherapy, depending on the cancer type and stage. The first substantial chemotherapeutic for cancer therapy was chlormethine, a nitrogen mustard derivative, which was intentionally developed as a chemical warfare agent based on the sulfur mustard poison used during the World War I.³⁵⁻³⁷ The anti-tumor activity of this substance was discovered in 1942 and chlormethine (Mustargen[®]) as well as a number of derivatives (e.g. cyclophosphamide, ifosfamide) are used as chemotherapeutics down to the present day. Many other substance classes have been discovered since then. However, for

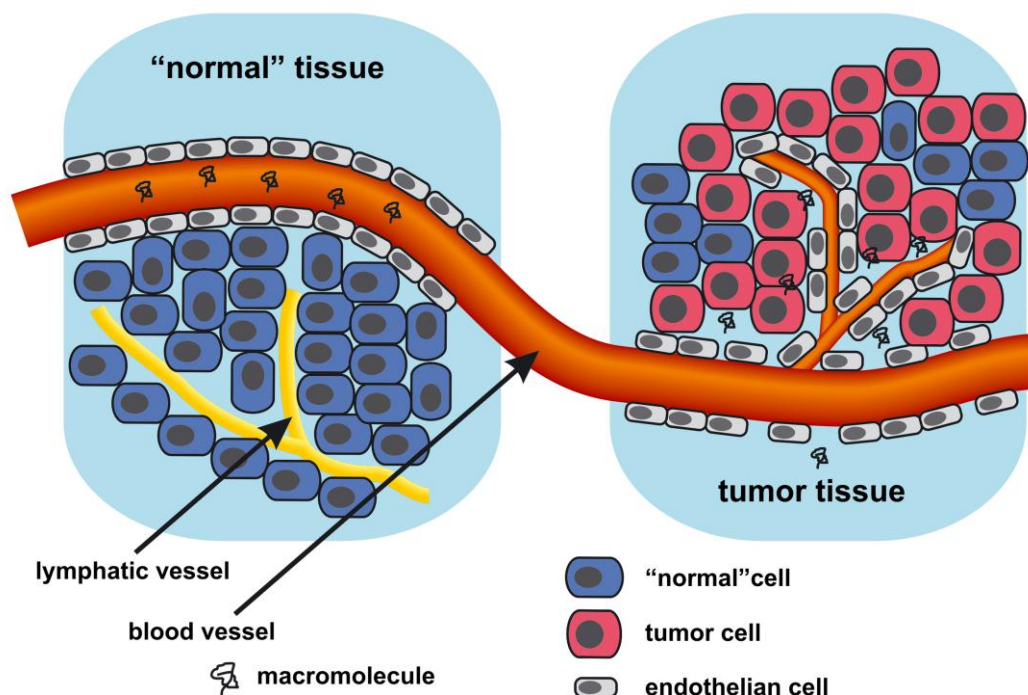
decades cancer therapy was limited to classical cytotoxic substances inhibiting cell division and leading to apoptosis. But in recent years, besides new classical chemotherapeutics, also alternative therapeutic approaches have been developed or are under research. Examples include for instance molecularly targeted drugs,³⁸ stem cell therapy,^{39,40} gene therapy,^{41,42} cancer vaccines^{43,44} and others. From all these approaches, molecularly targeted drugs have been the most successful in the last years, leading to market authorizations of drugs (often monoclonal antibodies) targeting for instance tumor-specific tyrosine kinases (e.g. Gleevec[®]) or growth factor receptors like VEGF (Avastin[®]) or HER-2 (Herceptin[®]).⁴⁵⁻⁴⁷

Besides researching new chemotherapeutic compounds and molecular targets, efforts have been made to improve tumor-specific drug delivery and pharmacokinetics of the chemotherapeutics, which resulted in several approved products (e.g. Abraxane[®] or Caelyx[®]). By conjugation of radionuclides or cytotoxic agents with tumor cell specific monoclonal antibodies, efficient therapeutics against certain types of cancer could be developed (e.g. Bexxar[®] or Ontak[®]); however these actively targeted therapies are – like all antibody related therapeutics – only effective for certain tumors, expressing the specific antigen. It is the advantage of passive tumor targeting that the therapeutic response is not dependent on the presence of specific antigens. Many types of nanocarriers like nanoparticles,⁴⁸⁻⁵⁰ liposomes,⁵¹⁻⁵³ micelles⁵⁴⁻⁵⁶ or polymer conjugates⁵⁷⁻⁵⁹ have been extensively investigated for efficient passive delivery of chemotherapeutics to the tumor. The principle behind all those drug delivery systems is passive accumulation in the tumor due to the enhanced permeability and retention effect (EPR).

All these efforts in drug discovery, molecular target identification and drug delivery resulted in a steadily improved cancer therapy in the recent years, but nonetheless many patients die from cancer due to resistance of cancer cells to chemotherapeutic therapy. Whether or not a cancer is therapy-resistant is based on a variety of mutations of the cancer cells.⁶⁰⁻⁶² In Germany, the relative 5-year survival of patients suffering from colorectal cancer (CRC) – which was chosen as model cancer in this work – was 62 % in 2008, meaning that two out of five patients die from CRC within five years after diagnosis. Solely in 2008 this meant approximately 27,000 people having died from CRC in Germany.⁹ This clearly emphasizes the need of continuous research in this field.

1.2 The EPR-Effect

The enhanced permeability and retention effect (EPR) has become a popular model to describe the specific property of the tissue in solid tumors. Due to extensive angiogenesis, high blood vessel density and many other morphological differences, the blood vessel endothelium is more permeable to macromolecules or other nano-scaled structures than “normal” blood vessels.^{63,64} On the other hand, the lymphatic system is insufficiently developed, which may result in retention of extravasated carriers or macromolecules in the tissue.⁶³⁻⁶⁶ The principle of EPR is presented in Scheme 1. The effect has been first described by *Yasuhiro Matsumura* and *Hiroshi Maeda* more than 25 years ago for proteins of different size, although it was not called EPR at that time.⁶⁷



Scheme 1. Principle of the EPR effect inspired from previous publications^{59,68,69} (schematic and not true to scale). Whereas the endothelium in “normal” tissue is tight, tumor tissue has a high density of leaky blood vessel endothelia and lacks of functional lymphatic system. Thus, macromolecules can be extravasated and retained in tumor tissue.

The principle of EPR as a driving force has been proven by i.v. injection of Evans Blue dye into tumor bearing mice. The dye tightly binds to albumin, and the dye extravasation to tumors can be regarded as macromolecular extravasation.^{67,70} The EPR effect has been extensively investigated and enlightened in the last decades.⁷¹⁻⁷³ It has been claimed as driving force for the development of all kinds of nanocarriers for passively

targeted tumor therapy.^{69,74-77} Today the effect is more critically discussed, even by its discoverer *Hiroshi Maeda*.^{71,72} Especially the increased interstitial fluid pressure (IFP), which can be regarded as consequence of lacking lymphatic function that has been observed in several tumors⁷⁸⁻⁸⁰ is discussed as a hurdle for EPR-based tumor targeting.⁸¹ Also notable is the fact that even more than 25 years after the first description of this effect no products were approved for the market, for which EPR could be seriously considered as a driving force, except from Doxil[®], Abraxane[®] and SMANCS (in Japan only). Nevertheless, several products have been and still are evolved in clinical studys. However, it had turned out that EPR may be exploited by artificial hypertension.^{70,73,82}

1.3 Polymer Therapeutics

Many drug delivery systems and medical devices consist of polymers and thus may be regarded as polymer therapeutics, including hydrogels, wound-adhesives, nanoparticles and many others. Within this work the term “polymer therapeutics” is used for water-soluble polymers which might be used for drug delivery or diagnostic purposes in injectable solutions, which reflects only one part of polymers in medicine.

In fact, polymers have been already used in medicine and pharmacy for centuries considering for example polymers from natural sources as excipients in tablets, pills or gels. However, “polymer therapeutics” is also used as a collective term for all modern polymer-related drug delivery systems, for instance rationally designed macromolecular drugs, polymer conjugates, polymeric micelles or polyplexes for gene delivery.^{58,83} First clinical experiences with polymers as active pharmaceuticals were made in the 1940's, mainly with plasma expanders (PVP and dextran) or as antiseptics (PVP-iodine).⁸⁴ The beginning of rational polymer synthesis with the aim to develop nano-scaled drug delivery systems can be ascribed to a few pioneers who established fundamental knowledge in the field already in the 70s and 80s of the last century, particularly *Helmut Ringsdorf*,⁸⁵⁻⁸⁷ *Ruth Duncan*,⁸⁸⁻⁹⁰ *Jindřich Kopeček*,⁹¹⁻⁹³ and *Karel Ulbrich*.⁹⁴⁻⁹⁷ Based on the work of these pioneers a broad variety of polymer structures has been investigated for their potential as drug delivery systems in the last decades, including amongst many others polyethylene glycols,⁹⁸⁻¹⁰⁰ N-(2-hydroxypropyl)-methacrylamide,¹⁰¹⁻¹⁰³ polyglycerol polymers,^{104,105} poly-(2-oxazoline)s^{106,107} and polypeptides¹⁰⁸⁻¹¹⁰.

All these polymeric drug delivery systems consist of natural or synthetic water-soluble polymers and have a small size in common, which is usually below 100 nm.⁸³ Thus, polymer therapeutics can be of course regarded as a part of nanomedicine with all its unique features, opportunities and challenges. Undoubtedly, most often polymer therapeutics are researched and developed for the treatment of cancer, but many other indications have been also addressed, for instance hepatitis B and C (pegylated interferon α 2a; Pegasys[®]), cancer associated neutropenia (PEGylated filgrastim; Neulasta[®]) or multiple sclerosis (copolymer of alanine, lysine, glutamic acid and tyrosine; Copaxone[®]).^{84,111} Further, polymer conjugation presents to be a possibility to affect pharmacokinetics by enhancing body circulation time or could be used to reduce immunogenicity of proteins.^{111,112}

1.3.1 Polymers in Cancer Therapy

The research in polymer sciences of the recent decades contributed strongly to the achievements in cancer therapy – whether in consideration of chemotherapy wafers (Gliadel[®]), polymer-drug conjugates (Zinostatin Stimalmer[®]) or PEGylated Liposomes (Doxil[®]).^{68,113} In current research polymers are used to design various vehicles for the delivery of chemotherapeutics with the aim to increase the therapeutic efficacy and to reduce undesired side effects.¹¹⁴ Polymer-derived nanoparticles and micelles have been intensively studied,^{54,74,114-118} but also water-soluble polymer-drug conjugates gained particular interest in the recent years.^{68,119-123} The broad interest raises the question: What are the benefits of polymer drug conjugates compared to other drug delivery systems? Answering this question, three advantages are very important:

- First, in polymer-drug conjugates tumor-specifically degradable linker are often used, whereas the partition equilibrium of the drug at the particle-solvent interface is a crucial limiting factor for drug release from nanoparticles or nanocapsules. Usually, the – often lipophilic – chemotherapeutic drug is incorporated in carriers, which also often exhibit pronounced lipophilicity, which results in poor drug release.
- Second, the small and hydrophilic polymer-drug conjugates often have extended body circulation without showing the typical blood-removal effects of particulate drug delivery systems (strong accumulation in liver or spleen).

- Third, polymer–drug conjugates provide the opportunity of optimized combination therapy by conjugation of more than one drug in an optimized ratio.¹²⁴⁻¹²⁶

Nonetheless, the transfer of these advantages to approved market products is very challenging. To satisfy regulatory requirements, detailed and validated understanding of polymer purity and heterogeneity as well as extensive knowledge about toxicity issues is required.¹²⁷⁻¹²⁹ However, more than ten polymer–drug conjugates for the treatment of cancer have been already taking the step from the preclinical to the clinical stage.^{75,84,130} The most promising candidates currently investigated are given in Table 1. Although Opaxio™ has been demonstrated to be a very promising candidate in several clinical studies, a market authorization application in Europe for the treatment of lung cancer was withdrawn by the manufacturer.^{131,132}

Table 1. *Examples of recently developed promising polymer–drug conjugates that managed the leap to be investigated in clinical studies.*

Substance	Company	Composition	Indication	Stage
Opaxio™ (Xyotax)	Cell Therapeutics, Inc.	PGA-paclitaxel	non-small-cell lung cancer, ovarian cancer and others	Phase III
ProLindac™	Access Pharmaceuticals, Inc.	HPMA- copolymer- DACH-platinat	metastatic and/or unresectable recurrent head and neck cancer	Phase II
(HA)iri	Alchemia Ltd.	HA-Irinotecan	metastatic colorectal cancer	Phase III

PGA: polyglutamate; **HPMA:** N-(2-hydroxypropyl)-methacrylamide; **DACH:** diaminocyclohexane; **HA:** hyaluronic acid

1.4 Imaging of Cancer

Imaging technologies are used in a variety of diseases today. In cancer diagnostics, imaging is probably the most important diagnostic tool to detect cancer in its early stages, which is an important criterion for effective cancer therapy.¹³³ Without imaging techniques, early cancer diagnosis as well as observation of cancer therapy success and metastasis formation would be impossible. Several technologies have been developed and each has its unique field of application, strengths and limits. The most common imaging technologies that have become indispensable diagnostic tools in the clinic are computed X-ray tomography (CT), magnetic resonance imaging (MRI) and

ultrasound.¹³³ Functional imaging of metabolic processes or pathologic events has been achieved by use of emission tomography technologies like positron emission tomography (PET, using β -rays) or single photon emission computed tomography (SPECT, using γ -rays).^{134,135} For example, ¹⁸F-fluorodesoxyglucose (¹⁸FDG) is used as PET tracer to specifically detect tumor cells with enhanced glucose metabolism.^{136,137} However, tissue morphology cannot be displayed using PET and SPECT and therefore these techniques are nowadays combined with CT or MRI for diagnostic purposes.¹³⁸⁻¹⁴² Besides these clinically well-established imaging methods, fluorescence imaging (FLI), also often termed as optical imaging (OI), has recently also attracted increased attention in cancer research.

1.4.1 Fluorescence Imaging

Fluorescence imaging belongs to a series of imaging methods that use visible or near-infrared light as information medium.¹⁴³ In fluorescence imaging, light is emitted from fluorophores – which may be fluorescent proteins, quantum dots or small molecules – during exposure with excitation light. Thereby, the emitted light has usually less energy (resulting in longer wavelength) than the excitation light (Stokes shift). The fluorescence of the molecules can be isolated with appropriate filters and detected from a complex matrix, i.e. a living animal. It has been shown that there is an optimum wavelength for FLI in the near infrared (NIR) range of the spectrum due to low tissue absorbance, which leads to high light penetration.¹⁴⁴⁻¹⁴⁷

Further, the autofluorescence in animals (e.g. from nutrition and proteins) is lowest in this range, providing an optimum signal to noise ratio (SNR). However, the accuracy decreases by the use of NIR-light due to multiple scattering events.¹⁴⁶ As there are many influences on the measured fluorescence (for instance absorption, scattering and quenching effects), quantification is a difficult task in FLI. Although the interpretation of the results is not trivial, it is much more useful for screening purposes than other non-invasive imaging techniques (e.g. radionuclide-based approaches or MRI) due to its easy setup.^{148,149} For more detailed and quantitative results, fluorescence imaging has been recently combined with CT.^{150,151}

Fluorescence imaging has been shown to be a versatile tool for tracking the *in vivo* fate of nanoscaled drug delivery systems in preclinical animal studies.¹⁵¹⁻¹⁵⁵ One of the major advantages of FLI compared to other imaging techniques is an overall easy set-up: for instance, neither are radioactive labels required (like in PET or SPECT) nor is

radioactivity used for the measurement (like in CT or X-ray), nor is expensive cooling required (like often in MRI). Further, based on the variety of available fluorescent molecules a conjugation of any molecule is feasible and due to the stability of many fluorophores long-term observation even for several months is possible with nontoxic fluorescent probes. Beyond simple fluorescence imaging, the development of multispectral imaging algorithms provide the possibility to observe two or more fluorescent probes simultaneously and to increase the SNR by autofluorescence spectrum subtraction.

In the recent years strong efforts have been made to transfer the experience made with preclinical fluorescence imaging towards a clinical application. Amongst others, research was focused on the development of an optical mammography scanner for detection or therapy monitoring of breast cancer.¹⁵⁶⁻¹⁶¹ Further, progress in clinical applications has been achieved in the detection of liver cancer^{162,163} or in the development of a hand-scanner for the detection of inflammation in patients with arthritis (Xiralite[®]).¹⁶⁴⁻¹⁶⁶ However, the use of fluorescence imaging in the clinic is difficult due to the limited penetration depth even of NIR light. The most promising use of fluorescence imaging is undoubtedly preclinical *in vivo* imaging in small animals.

1.5 Aims and Objectives

Although polymers have been investigated as potential drug delivery systems for years, systematic knowledge about the relationship of polymer structure and the fate in the living organism is often rare. This turned out to be a major obstacle on the road towards authorized products. This work focuses on multispectral fluorescence imaging as a preclinical method to evaluate the body fate of potential polymeric drug carriers. Therefore, structurally different polymer classes are investigated for their potential as drug delivery system for targeted cancer therapy within this work: HPMA copolymers, carbohydrates and polyglutamates. All polymers were obtained either from cooperation partners or provided by a company. In particular, the following major objectives are addressed:

- Characterization of the polymers *in vitro* and selection of suitable candidates for *in vivo* multispectral FLI. In this regard, the molecular weight distribution and particle size are of special interest. If necessary, the potential toxicities are also addressed.
- Selection of suitable fluorescent dyes for multispectral FLI and synthesis of stable fluorescent polymer-dye conjugates from the carbohydrates and the polyglutamates.
- Evaluation of the potential of multispectral FLI as a preclinical tool to characterize and compare the biodistribution and elimination of various polymers in a nude mouse model with a special focus on the structure and architecture dependent accumulation in certain organs. The use of multispectral FLI to characterize the distribution of a polymer and a releasable fluorescent drug model simultaneously.
- Investigation of the potential of the most promising candidates from each polymer class for passive tumor targeting and use of FLI to prove the accumulation in subcutaneous human colon carcinoma xenograft models.
- Development and evaluation of a comparable quantification method for the multispectral FLI to analyze and describe the tumor accumulation of different polymers.
- Confirmation of the predictive tumor accumulation results of one polymer in a therapy study to demonstrate the beneficial effect of passive tumor targeting.

2 Experiments

2.1 Materials

A variety of chemicals, reagents and solvents has been used for conjugation chemistry and for the experiments described in this thesis. A complete listing of all substances and its origin is given in appendix 5.1.

2.1.1 Origin of Polymer Precursors

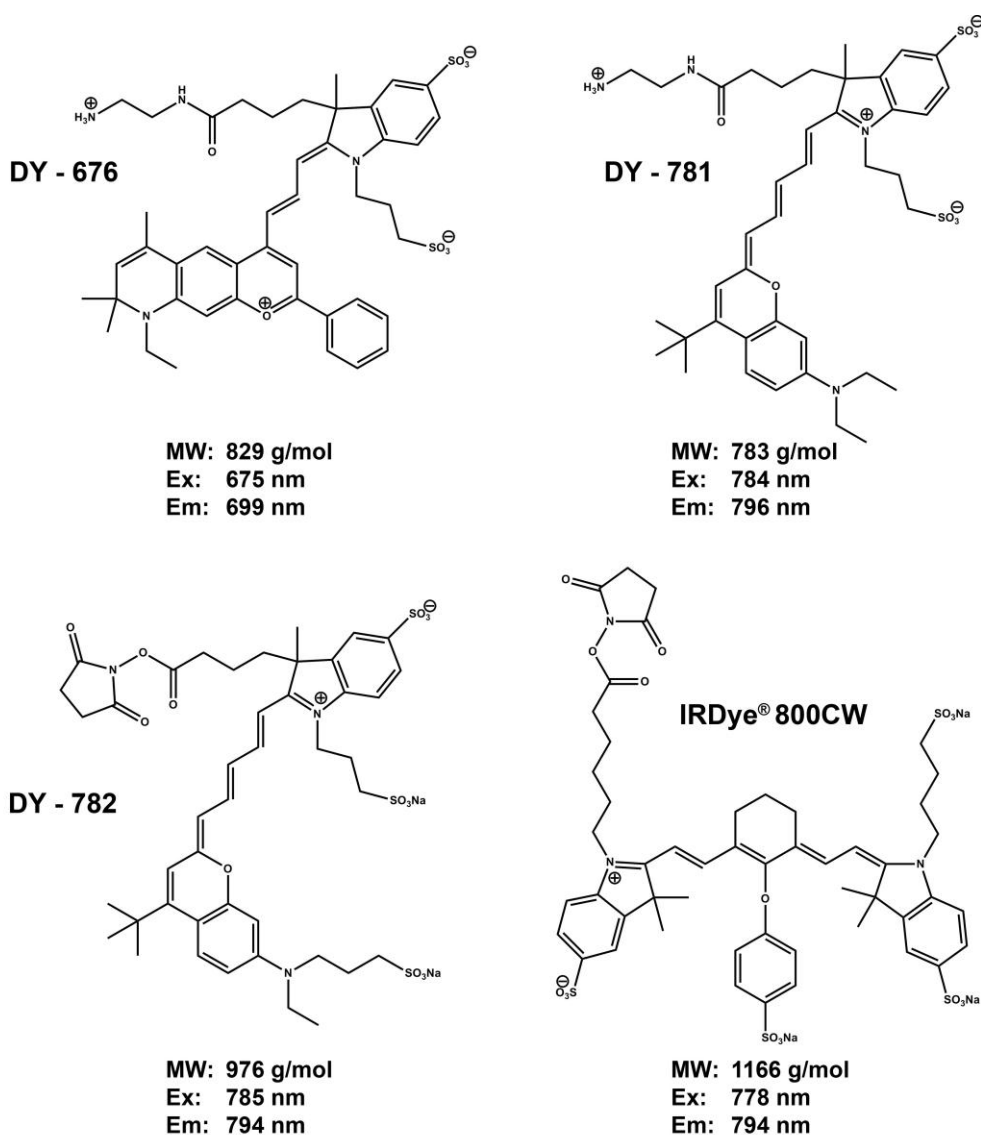
All polymers based on *N*-(2-hydroxypropyl)-methacrylamide (HPMA) have been originally synthesized by radical copolymerization of monomers by cooperation partners in Prague, Czech Republic.^a The polymer precursors based on polyglutamic acid (PGA) have been originally synthesized by RAFT polymerization of monomers from cooperation partners in Valencia, Spain.^b The synthesis of these polymer classes is not part of this thesis. The carbohydrates polymers used within this work have been kindly provided by Serumwerk Bernburg AG, Germany.

2.1.2 Fluorescence Dyes

Fluorescence dyes used for polymer labeling were purchased either from Dyomics, Germany (DY-676-Amine, DY-781-Amine and DY-782-NHS ester) or from Li-Cor, USA (IRDye[®] 800CW-NHS ester). An overview of the structures and fluorescent properties is presented in Scheme 2. The fluorescent dyes used in this work are cyanines, exhibiting stable and pronounced fluorescence emission in the far red or near infrared part of the electromagnetic spectrum. Amines or *N*-Hydroxysuccinimide esters (NHS) were chosen as reactive groups for conjugation reactions with the polymers (Scheme 2).

^a Institute of Macromolecular Chemistry AS CR, v.v.i., Heyrovský Sq. 2, 162 06 Prague 6, Czech Republic (T. Etrych, L. Schindler (née Vystrčilová), P. Chytil)

^b Centro de Investigación Príncipe Felipe, C/ Eduardo Primo Yúfera 3, 46012 Valencia, Spain (M.J. Vicent, R. England, F. Canal)



Scheme 2. Structure and properties of the fluorescence dyes used for polymer conjugation as published by the manufacturers. MW: molecular weight; Ex/Em: excitation maximum and emission maximum in ethanol (DY-676, DY-781, DY-782) or methanol (IRDye® 800CW).

2.1.3 Origin and Specifications of Animals

Two strains of nude mice were used for *in vivo* and *ex vivo* experiments. The strain SKH1-*Hr^{hr}* was used for the characterization of polymer biodistribution and elimination. Unless otherwise stated, these mice were taken as females (2-6 months old) from the breeding of the ZMG of the Martin-Luther-University Halle-Wittenberg (originally ordered from Charles River Laboratories). All tumor-experiments were carried out in male athymic nude mice (Hs1Cpb:NMRI-*Foxn1^{nu}*), which were ordered from Harlan Winkelmann, Germany. Tumors were inoculated at an age of 6-8 weeks.

2.2 Methods

2.2.1 Conjugation Chemistry

2.2.1.1 HPMA Copolymers

All HPMA based polymers were synthesized and conjugated with the fluorescent dyes DY-676 and DY-782 by cooperation partners in Prague (Czech Republic) based on previously published methods.

2.2.1.2 Carbohydrate Polymers

The carbohydrates used in this work present solely hydroxyl-group as reaction site. To provide a stable and under physiological conditions non-cleavable polymer-dye conjugate, amine functions were introduced to the polymers prior to conjugation with the dye IRDye[®] 800CW to provide a stable amide bond. For this purpose all polymers were activated with p-toluenesulfonyl chloride based on a previously described method.¹⁶⁷

1 g of HES 200 or HES 450 respectively was dissolved in 20 mL dimethylformamide (DMF). 1 g Dextran 500 was dissolved in 20 mL borax buffer (pH 10) as the reaction in DMF did not work here. Tosyl-activation in aqueous media was already previously described.¹⁶⁸ All solutions were cooled to 2-4 °C and 2 mL triethylamine were added. 0.3 g (HES 200 and 450) and 0.2 g (DEX 500) toluenesulfonyl chloride were dissolved in 2 mL DMF in the dark and dropwisely added to each polymer solution, which was then stirred for 2 h in the dark at 2-4 °C. The polymers were precipitated by pouring the solutions into 100 mL cold acetone (4 °C), washed 3 times with each 20 mL cold acetone, dried, dissolved in 30 mL water and dialysed against 1.5 L water for 72 hours (3.5 kDa membrane, medium was changed five times). The resulting solutions were lyophilized afterwards and the reaction success was evaluated by ¹H-NMR spectroscopy. 300 mg of the tosyl-activated polymers were dissolved in a 50 mL mixture of borax buffer (pH 9.5) and DMF (2:1 v/v). 1.5 g ethylenediamine (500 fold molar excess) were added and the solution was stirred for two days at 40 °C (HES 200 and HES 450) or for one day at 70°C (DEX 500) in the dark. The amine-modified polymers were precipitated in a mixture of methanol and 2-propanol (1:1 v/v, 200 mL), washed 3 times with 20 mL methanol/2-propanol, dried, dissolved in 30 mL water, dialysed against water for 72 hours as described above and lyophilized.

After amine modification, the modified polymers were conjugated with an amine-specific NHS ester of the fluorescent dye IRDye[®] 800CW. Therefore, 100 mg of the amine-modified polymers were dissolved in bi-distilled water (50 mL) and reacted with 0.6 mg dye IRDye[®] 800CW-NHS ester in the dark for two hours at 4 °C and a pH of 8.5 and subsequently dialysed against water and lyophilized afterwards. Unmodified dextran 500 (60 mg) was conjugated with 0.4 mg IRDye[®] 800CW-NHS ester to serve as an ester control using the same reaction parameters. The polymer solution was frozen in liquid nitrogen immediately after the reaction and subsequently lyophilized to avoid ester hydrolysis.

2.2.1.3 PGA Polymers

Polymers based on polyglutamic acid present carboxylates as reactive site. Once again, an amide bond was chosen to be formed because of the *in vivo* stability. Thus the carboxyl-groups were activated with NHS and the NHS-activated polymer was conjugated with an amine reactive fluorescent dye (DY-781-NH₂). The following reaction procedure was used for each of the polymers:

60 mg of the PGA polymers (sodium salts) were dissolved in 20 mL purified water. 12 mg NHS (TB-PGA-200 and S-PGA-200) or 20 mg Sulfo-NHS (DB-PGA-150 and L-PGA-400) were added, respectively. The pH was dropwisely adjusted with 1 mM HCl to 5.0 and the solution was cooled on ice to 2-4 °C in the dark. 10 mg EDCI was added to the solution in two equal portions with a time delay of five minutes. The pH of the solution increased immediately and was kept constant at pH 5.0 ± 0.5 by addition of 1 mM HCl. When the pH remained constant, immediately 0.5 mg dye (DY-781-NH₂) in 1 mL methanol was added to the solution and the pH was raised to 8.5 - 9.0 by addition of 1mM NaOH. The solution was stirred for 2-3 hours at 4 °C and the pH was constantly checked and kept at 8.75 ± 0.25. Afterwards, the solution was dialyzed against 2 L water for 3-5 days (3.5 kDa membrane, medium was changed 5-8 times) to remove unreacted dye, NHS and solvents and afterwards subsequently lyophilized.

2.2.2 Lyophilization

Lyophilization of the polymer-dye conjugates and synthesis intermediates was carried out after rapid freezing of the polymer solutions (polymers in bi-distilled water) in liquid nitrogen in 250 mL round flasks. A Christ ALPHA 1-2 freeze drying system was

combined with a Vacubrand RZ 2 vacuum pump for the Lyophilization process, which lasted 24-48 h.

2.2.3 ¹H-NMR-Spectroscopy

Success of the activation reactions of the carbohydrate polymers with toluenesulfonyl chloride and the following cleavage of the tosyl-groups was proven by nuclear magnetic resonance spectroscopy (¹H-NMR). Therefore, 7 mg polymer were dissolved in 700 μL D₂O and ¹H-NMR spectra were recorded at 400 MHz using a Gemini 2000 spectrometer (Varian Inc., France).

2.2.4 Particle Size and Molecular Weight Distribution

Particle size distributions were measured by dynamic light scattering (DLS) and by asymmetric flow field-flow fractionation (AF4), which additionally exhibited precise molecular weight distribution of the polymers.

2.2.4.1 Dynamic Light Scattering

DLS, also known as photon correlation spectroscopy (PCS), is a routinely used method to determine hydrodynamic radii of particles. The principle of this technique is the correlation of time dependent intensity fluctuations of scattered laser light with the Brownian motion of the particles. The theory behind this technique is reviewed in the literature.¹⁶⁹⁻¹⁷¹ Particle size distributions were measured by dynamic light scattering on a Nano-ZS instrument Zetasizer (ZEN3600, Malvern, UK). Samples were dissolved in bi-distilled water (10 mg/mL) and filtered (0.45 μm) prior to measurements at 25 °C in the backscattering mode at 173° (n=4). The refractive index of 1.33 and a viscosity of 0.89 mPa*s were used for the medium (water at 25 °C). Z-average values and polydispersity was calculated using the instrument software (version 6.30).

2.2.4.2 AF4/MALLS

Field-flow fractionation is a separation method for particles and macromolecules. The difference to chromatographic separation techniques is that a field of separation force is applied to the particles in the mobile phase and this field replaces the stationary phase in chromatographic techniques.^{172,173} In asymmetric flow field-flow fractionation (AF4), an

asymmetric cross-flow is used as field of force to separate the particles or molecules in a separation channel having a permeable wall.¹⁷⁴ This technique has attracted attention especially for characterization of molecular weight distributions of polymers.¹⁷⁵⁻¹⁷⁸ The basic separation principle of AF4/MALLS has been adequately described previously.^{179,180}

With the aim to determine the molecular weight distribution, asymmetric flow field-flow fractionation (AF4, Eclipse F) was combined with a multi-angle light scattering detector (MALLS, DAWN EOS) and an RI detector (Shodex 101). The length of the trapezoidal channel was 265 mm and its height was 350 μm . Polyethersulfone (PES) with a MWCO 5k (Wyatt, Germany) was used as a channel membrane for analyzes of the carbohydrates and regenerated cellulose (RC, MWCO 5 kDa, Microdyn Nadir GmbH, Germany) was used for the polymers based on polyglutamic acid. PBS preserved with 0.02 % sodium azide and filtered through 0.1 μm served as carrier liquid. 100 μL of polymer solution (1 mg/mL) in PBS were injected over two minutes (injection flow: 0.20 mL/min, focus flow: 2 mL/min) and then eluted with a constant detector flow (1 mL/min) and decreasing cross flow (Figure 1).

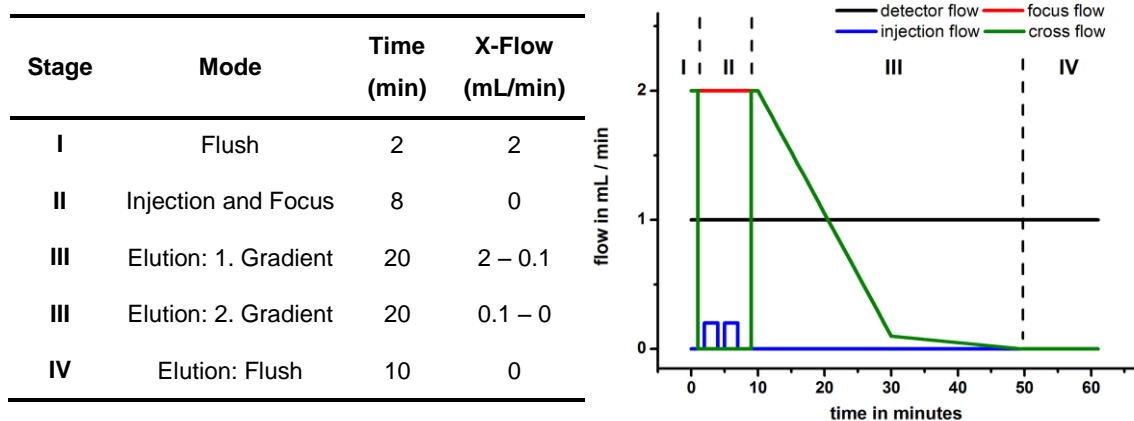


Figure 1. Flow regime used for separation in the AF4/MALLS analyses.

The molecular weight distribution of the polymers was calculated with the ASTRA software (version 4.90, Wyatt, Germany) based on the angle-dependent light scattering signals and the RI signals (RI signals were baseline corrected with the software Corona v.1.40), using the Debye fit model (5th order polynomial). The incremental change of the refractive index (dn/dc), which is needed to calculate the concentration at each elution time and thus the molecular weight, was determined in PBS at 25 °C by injection of different concentrations in the range of 0.2 mg/mL to 1 mg/mL to the RI detector. The

polymer size was calculated as z-average mean square diameters (D_z) and the molecular weight was calculated as weight averaged molar mass (M_w). All measurements were carried out at least in duplicate and results are given as average.

2.2.5 *In Vitro* Toxicity Experiments

2.2.5.1 Hemolytic Assay

Hemolytic assays with minor variations have been often described in literature.¹⁸¹⁻¹⁸⁴ In this work, a hemolytic assay was performed in a 2 % (V/V) dispersion of red blood cells (RBC's) in phosphate buffer saline (PBS, pH 7.4, osmolarity 310 mosm/L), according to a previously described principle.¹⁸⁵ 15 mL Human EDTA-blood from healthy donors was centrifuged ten minutes at 4000 rpm (~2000 g, Heraeus Labofuge 300). The supernatant was aspirated and the RBC's were washed four times with PBS and subsequently centrifuged ten minutes at 4000 rpm to be afterwards diluted with PBS to ~ 100 mL of a 4 % RBC dispersion (v/v).

20 mg of the PGA-based polymer were dissolved each in 1000 μ L PBS. 250 μ L of the solution (5 mg accordingly) were added to Eppendorf[®] reaction vessels, containing each 250 μ L 4 % RBC suspension (carried out in triplicate). 200 μ L of the remaining volume were diluted with 600 μ L PBS and served as a reference solution in the photometer. The reaction vessels containing 2 % (v/v) RBC's and 1 % (m/v) polymer were thereafter incubated for 1 h in an end-over-end shaker at 37 °C and 10 rpm and subsequently centrifuged five minutes at 6700 g (10.000 rpm, Minispin[®], Eppendorf, Germany). RBC's in pure PBS served as a negative control and a 2 % (m/v) solution of sodium dodecyl sulfate (SDS) instead of a polymer served as a positive control. The supernatant was aspirated after incubation and all sample supernatants were diluted with PBS (1:1).

Hemoglobin absorption was measured spectrophotometrically on a Spekol 1200 using the Aspect Plus v1.5 software (Analytik Jena AG, Germany) in the absorption maximum at a wavelength of 415 nm against the reference solution. Hemolytic properties were described as the ratio of sample hemoglobin absorption compared to the total hemoglobin absorption of the SDS-solution, which had to be diluted with PBS (1:50). All measured absorptions were in a range between 0.2 and 0.8 (except of Kolliphor[®] P188 control: A=0.1). Thus, a linear correlation of the absorption and concentration was expected.

2.2.5.2 *In Vitro* Cytotoxicity

The cytotoxicity of the carbohydrates was investigated by the MTT assay. The polymers were dissolved in phosphate buffered saline (PBS) at stock concentrations of 200 mg/mL and 20 mg/mL. The solutions were diluted 1:10 (v/v) with minimum essential medium (MEM) with Earl's salt and phenol red (supplemented with 10 % FBS, sodium pyruvate solution, non-essential amino acid solution and gentamicin-glutamine solution). HepG2 cells (3×10^4 cells/well) were grown at 37 °C and 5 % CO₂ atmosphere in a 96-well plate in the same supplemented MEM. After 24 h, the medium was removed and 100 µL of the polymer solution were added to each well. After incubation for 24 h or 48 h, the supernatant was removed and cells were incubated with 100 µL solution of MTT (500 µg/mL) in indicator-free MEM medium without supplements for 3 h. Cells were lysed subsequently with 100 µL lysis medium (5 g sodium dodecylsulfate, 0.3 mL acetic acid and 49.7 mL DMSO) for 1 h and absorption was measured with a microplate reader (BMG Labtech Polarstar Omega) at 570 nm. Non-treated cells were used as a reference (negative control) and cells treated with 100 µL DMSO (30 % v/v in MEM) were the positive control.

2.2.5.3 Cytokine Activation Assay

Stimulation of inflammatory cytokines was investigated in human peripheral blood mononuclear cells (PBMCs). Heparinized blood was obtained from 3 healthy donors and PBMCs were isolated by density gradient centrifugation (2000 g, Heraeus Biofuge Stratos) in lymphocyte separation medium (LSM 1077). After washing with PBS, cells were resuspended in RPMI 1640 medium containing 10 % inactivated human serum from the same donor and seeded in a 24-well plate at a concentration of 5×10^5 cells per well. 10 µL of the carbohydrate polymer solutions (200 mg/mL in PBS) were added to the sample wells. 20 µL solution of lipopolysaccharide from *Escherichia coli* (LPS, 1 µg/mL) were used as positive control and 10 µL PBS as negative control. RPMI 1640 medium containing 10 % inactivated human serum was added to the wells to give a total volume of 1 mL per well and the cells were incubated at 37 °C in a 5 % CO₂ atmosphere. After incubation for 4 h or 24 h, supernatants were aspirated, centrifuged 3 minutes at 18,500 g (Hettich Mikro 200R) and immediately frozen in liquid nitrogen. Cell viability was checked after 4 h and 24 h by Trypan blue exclusion and was found to be > 95 %. Inflammatory cytokines (IL-1β, IL-6, IL-8, IL-10, IL-12p70 and TNF) were analyzed by a cytometric multibead assay using the BD CBA human inflammatory

cytokines kit and following the kit instructions. A 10-point calibration curve was measured between 20 pg/mL and 5,000 pg/mL. Measurements of the beads were performed on a BD LSR II Fortessa™ Cell Analyzer on FL2 and FL3 channel using the FACS Diva™ Software and the results were analyzed using FCAP Array™ Software (Version 3.0). All measurements were performed with independent duplicates and the results are given as a mean of 3 different blood samples, each measured in duplicate.

2.2.6 Multispectral Fluorescence Imaging

2.2.6.1 Instrumentation and Specifications

Multispectral FLI was carried out with the Maestro™ imaging system from Cambridge Research & Instrumentation Inc. (now: Perkin Elmer Inc., USA). It was combined with a small animal gas anesthesia system. The imaging system contained an internal 300 W xenon lamp as light source and suitable excitation light was created by the use of a bandpass excitation filter. The light was transferred by fiber-optics to the illumination module and the region of interest (ROI) was illuminated from four illuminator arms. Image magnification was adjustable by different table stages and the lamps were as well adjustable to ensure an optimum illumination of the ROI. The emitted fluorescence light was pre-filtered by a suitable longpass emission filter, which prevented bleeding of excitation light to the camera. An example of possible excitation and emission filter sets is given in Table 2 and an overview of the Maestro™ imaging system is presented in Figure 2.

Table 2. *Excitation and emission filter sets for the Maestro™ imaging system (selection) and the auto-exposure time of a nude mouse (due to autofluorescence).*

Filter set	Excitation bandwidth	Emission bandwidth	Auto-exposure time (nude mouse)
Green	503 nm – 555 nm	580 nm longpass	~ 400 ms
Yellow	570 nm – 610 nm	645 nm longpass	~ 800 ms
Red	615 nm – 665 nm	700 nm longpass	~ 1500 ms
NIR	710 nm – 760 nm	800 nm longpass	5000 ms

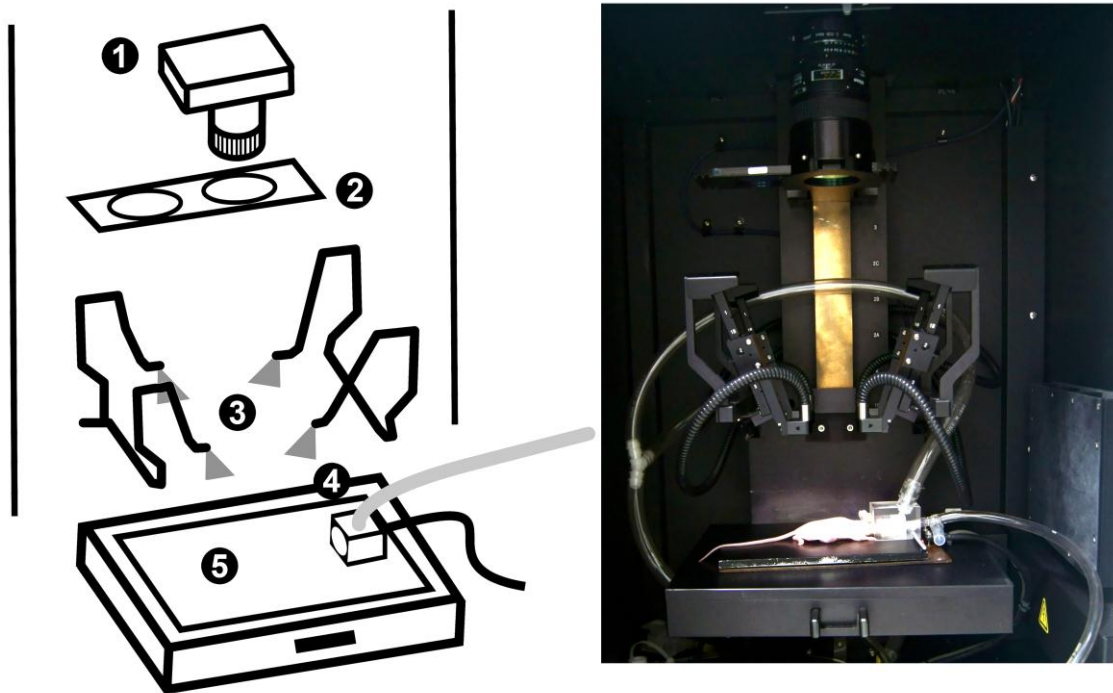


Figure 2. Overview over the Maestro™ imaging system. **Left:** schematic illustration. **1:** CCD-camera with lens; **2:** emission filter; **3:** excitation light illumination module with four arms **4:** small animal anesthetic mask with suction; **5:** table with heated plate. **Right:** corresponding photograph of the imager with an anesthetized mouse.

After having been pre-filtered by the emission filter, the fluorescence light passes a liquid crystal tunable filter (LCTF), before it is detected by a cooled (8 °C) 1.5 MP CCD camera as a 12 bit grayscale image. The LCTF was software-controlled and allowed the camera to acquire grayscale images at predefined wavelength steps. The step-bandwidth was set to 10 nm in all experiments. The software (Maestro v. 2.10) calculated one single data file (“cube”) from the acquired 12 bit grayscale images, containing the complete spectral information for each pixel of the images.

2.2.6.2 Cube Acquisition

To keep the data manageable and to increase the signal intensity, the resolution of the cubes was decreased by a factor of 4 by software-summation of the fluorescence signal from each four pixels (binning 2x2). Thus, all images had a length of 696 px and a width of 520 px, which provided detailed images by a 4-fold decreased exposure time and 4-fold decreased file size. The exposure time was always set automatically by the software before grabbing each cube to ensure highest possible data content without over-exposure. FLI was preferably done with fluorescent dyes emitting light > 700 nm,

because the autofluorescence of the mouse was lowest in that range of the spectrum, leading to a good signal-noise ratio (SNR). For the experiments with carbohydrates and polyglutamates, the NIR filter set was used. For the experiments with dual labeled HPMA copolymers, the red and NIR filter set were combined for acquiring one cube with two different filter sets successively.

2.2.6.3 Data Processing and Fluorescence Image Extraction

The information contained in the fluorescence image cube was analyzed using a library of previously recorded reference fluorescence spectra. Reference spectra of the fluorescence dyes in bi-distilled water, of the background and of the mouse autofluorescence were used. Thus it was possible to separate the dye-signal from the background and mouse autofluorescence (except for dual-labeled HPMA copolymers, cp. chapter 3.1.2, p. 30 ff.). Single spectral components were unmixed from the cube by the Maestro™ software based on the reference spectrum and were displayed in a grayscale “spectral component image”. These images could be merged in a “pseudo-colored composite image” to display the distribution of several species in one image (Figure 3). For comparison of the spectral component images from different cubes, the images were displayed using the “compare images” tool of the Maestro™ software. Thus, a color profile could be chosen for better visualization and the influence of different exposure times could be eliminated. Further, a scale bar was exhibited correlating the image color with the measured fluorescence intensity using the “compare images” tool. Within this thesis all presented images with scale bars were created by spectral deconvolution and use of the “compare images” tool of the Maestro™ software. The “hot” color profile was chosen for better visualization of the grayscale image. The scale unit of the scale bars displayed in all fluorescence images within this work is “scaled counts / second”, a value which is calculated from the fluorescence counts by the Maestro™ software as follows:

$$\text{scaled counts} / \text{s} = \frac{\text{counts}}{2^{\text{bit depth}}} * \frac{1}{\text{exposure time (s)}} * \frac{1}{\text{binning}^2} * \frac{1}{\text{gain}}$$

A fixed bit depth (12 bit), binning (2x2) and camera gain (3) was used in all experiments. The measured fluorescence intensity in each image pixel could be extracted from the spectral component images by the Maestro™ software. Thus it was possible to display the time dependent change of the fluorescence intensity in graphs. Therefore, a region of interest was specified in the spectral component images either manually (the tumor

ROI in the tumor accumulation experiments) or automatically by setting a threshold (used for all whole mouse fluorescence intensity measurements). The intensity normalized by exposure time, binning and camera gain (scaled counts/s) as well as the area of the ROI was thereafter displayed by the software. These values were used to calculate normalized fluorescence intensities from the images, which are independent from the area and exposure time. Unless otherwise stated, these intensities were displayed in the graphs within this thesis.

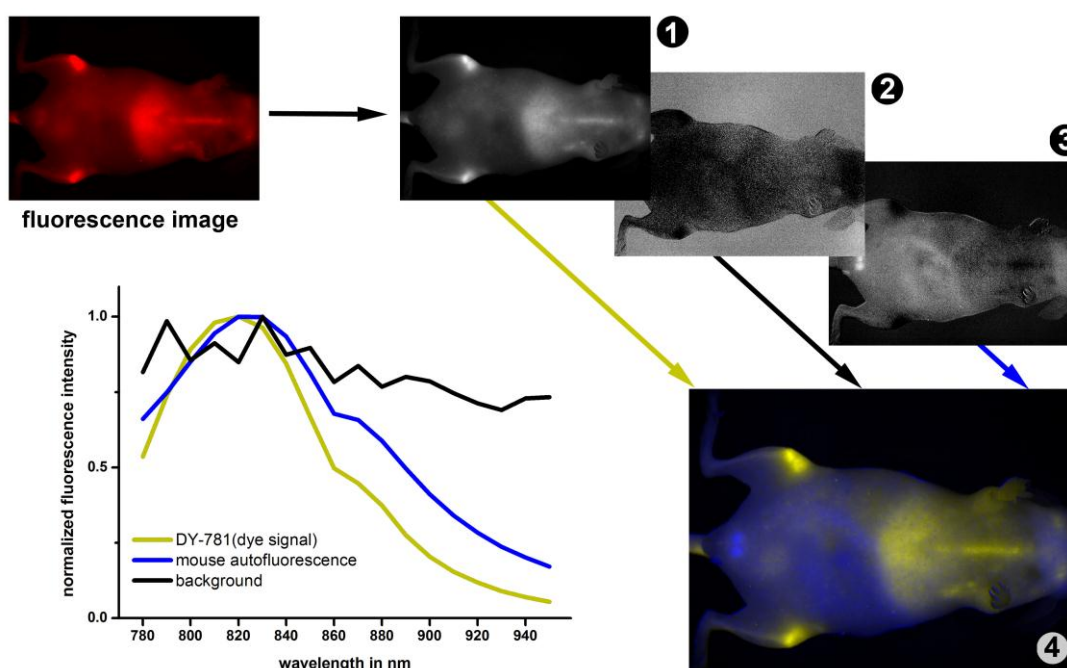


Figure 3. Illustration of the spectral deconvolution process of the fluorescence images based on previously recorded signal and autofluorescence reference spectra. The fluorescence image is deconvoluted into the dye signal component (1), background signal component (2) and autofluorescence signal component (3). Thereafter the component images can be merged and displayed as a pseudo-colored fluorescence image (4). This image is discussed in chapter 3.5.4, p. 93.

2.2.7 In Vivo Experiments and Animal Care

2.2.7.1 Animal Care

All *in vivo* experiments complied with regional regulations and guidelines and were approved by the local authority in Saxony-Anhalt (Approval No. 203.h-42502-2-920 and 203.h-42502-2-1186). Nude mice with albino background were used for the *in vivo* experiments as hairs would have scattered the light. All mice were kept under controlled conditions (12 h day/night cycle, 24 °C, 65 % relative humidity) in groups of 2-4 animals per box. For the imaging process, the mice were anesthetised with an initial dose of

2.5 % isoflurane for veterinary use (Forane[®], Abbott) in oxygen at a flow of 2 L per minute and a continuous dose of 1.5 - 2.5 % isoflurane in oxygen at a flow of 2 L/min, which was individually adjusted to the reaction of each animal. During the anaesthesia, mice were placed on a tempered plate (35 °C) to avoid decreasing body temperature.

2.2.7.2 Polymer Distribution and Elimination in Nude Mice

The *in vivo* biodistribution experiments have been carried out in groups of four nude female mice (strain: SKH1-*Hr^{hr}*, 2 – 4 month old). A total of 10 mg or 15 mg of each polymer-dye conjugate was dissolved in 1 mL isotonic sorbitol solution (5% m/m), respectively. The solution was sterile-filtered (0.2 µm Millex, Millipore, US) and 100 µL were injected into the tail vein of each mouse (n=4, 1 mg or 1.5 mg polymer per mouse, respectively). The injected polymer solutions were sterile, particle-free and isotonic and thus fulfilled the major requirements for parenteral preparations according to the European Pharmacopoeia.¹⁸⁶ Mice were imaged, until the polymers were excreted (several days up to 3 month) at a table position 1C and lamp position 2 in the Maestro[™] imaging system. The fluorescence image cubes were grubbed and processed as described in chapter 2.2.6, p. 19 ff. The total fluorescence intensity of the spectral component images was measured and analyzed (threshold set to 0). The highest measured intensity was defined as 100 % value and all other intensities were related to that.

2.2.7.3 Tumor Accumulation in Athymic Nude Mice

Investigation of tumor accumulation was performed in human xenograft colon carcinoma models (DLD-1 wild type and HT-29 wild type), which were inoculated in athymic nude mice, ordered from Harlan Winkelmann, Germany (Hs1Cpb NMRI-*Foxn1^{nu}*, five weeks old, male). After two weeks of setting in period, mice were short term anesthetised using isoflurane and tumor cells suspended in 150 µL PBS were subcutaneously injected to the left (HT-29, 4-5*10⁶ cells) and right (DLD-1, 4-5*10⁶ cells) flank of the mice.^c

Mouse weight and tumor size was constantly measured (every 2-3 days) and the tumor volume (V) was estimated based on length (l) and width (w) using the equation according to the results of *Euhus et al.* and *Tomayko et al.*^{187,188}:

^c Tumor cell culture and preparation of cell suspensions by Dr. Henrike Caysa and Dr. Thomas Mueller, Department of Internal Medicine IV, Oncology/Hematology, Martin-Luther-University Halle-Wittenberg, 06120 Halle, Germany

$$V = l * w^2 * \frac{\pi}{6}$$

Polymer solutions were injected 18 – 20 days after tumor cell inoculation. The mice were randomized into two groups according to their tumor size 1-2 days before polymer injection. Thus comparable and homogeneous groups were guaranteed. The polymer-dye conjugate solutions were intravenously injected to the tail vein (100 μ L of isotonic sorbitol solution containing 1.5 % polymer, sterile filtered before injection).

2.2.7.4 Autopsy and *Ex Vivo* Experiments

Ex vivo FLI of autopsied organs is an interesting addition to the *in vivo* measurements. One mouse of each group of the *in vivo* biodistribution and elimination studies was sacrificed and autopsied one day after injection of the polymer solution to obtain a more detailed view on the organ distribution of the fluorescence signal. Relevant mouse organs were placed in a well-plate (24 wells) and imaged at table height 1C and lamp stage 2 in the Maestro™ imaging system.

Contrary to previously published analyses of organ fluorescence intensities in a well-plate,^{118,154} the fluorescence intensity was related with the respective organ areas after manual drawing of an appropriate ROI. The advantages of this method are averaged intensities within single organs and area-normalized intensities. In some cases more detailed organ images were required and certain organs were therefore imaged on a plastic plate at a higher magnification by adjusting the table height to 2-3.

2.2.8 Therapy Study

The therapy study was performed with a subcutaneous human colon carcinoma xenograft model (DLD-1) in 30 athymic nude mice, (Hs1Cpb NMRI-*Foxn1^{nu}*, five weeks old, male). After two weeks of setting in period, mice were short term anesthetised with isoflurane and $5 \cdot 10^6$ cells were injected to the right flank. Mouse weight was measured daily and the tumor length and width was measured every second day for calculation of the tumor volume. Mice were randomized into five comparable groups (n=6 per group) based on the tumor sizes measured 14 days after tumor cell inoculation. An overview of the groups of the therapy study is presented in Table 3.

Table 3. Overview of therapy groups. Mice were randomized according to their tumor size 14 days after inoculation. Tumor sizes are given in cm^3 as means \pm SD, 6 mice per group.

Group	Tumor size in cm^3	Treatment description	Concentration in mg / mL
Free DOX	0.34 ± 0.17	5 mg DOX-HCl per kg body weight = 4.69 mg DOX	0.83
DOX-HPMA	0.33 ± 0.13	46 mg DOX-HPMA per kg body weight containing 10.2 % DOX (m/m) equivalent = 4.69 mg DOX	11.5
3x DOX-HPMA	0.33 ± 0.23	138 mg DOX-HPMA per kg body weight containing 10.2 % DOX (m/m) equivalent = 14.07 mg DOX	34.5
HPMA Control	0.33 ± 0.19	41.3 mg HPMA per kg body weight (equivalent to the amount of HPMA in the DOX-HPMA group)	10.4
NaCl Control	0.34 ± 0.18	solution of 0.9 % sodium chloride	-

Treatment was started 16 days after tumor cell inoculation with the star-like HPMA copolymers (200 kDa). Injectable solutions were prepared in 0.9 % NaCl solution at a concentration yielding in 150 μL ("Free DOX"-group) or 100 μL (all other groups) injection volume for a 25 g mouse. The amount of injected volume was adjusted for each individual mouse depending on its weight, to assure the target-concentration of 5 mg DOX per kg body weight. All solutions were sterile filtered (0.2 μm) prior to intravenous injection into the tail vein. The mice were continuously monitored during the study to evaluate the toxicity and tumor burden. A weekly dosing regimen was planned. The study was aborted for a group when individuals showed a tumor size $> 2 \text{ cm}^3$ or when severe toxicity occurred, necessitating the cessation of the experiment for ethical reasons.

2.2.9 Histology

The autopsied tumors from tumor bearing mice treated with dual-fluorescently labeled HPMA copolymers (OPB-spacer) were characterized after HE-staining by light microscopy. These tumors were axially bisected. Pieces of high and low drug model fluorescence were cut from the one half of the tumor, whereas the other one was left original. The pieces and the axial section were fixed in a solution of 4 % paraformaldehyde, embedded in paraffin and sliced with a Leica RM 2245 microtome (4 μm). The slices were placed on microscope slides, heated to 50 $^{\circ}\text{C}$ and dewaxed by

immersion (each five minutes) into the following solution series: Roti[®] Histol (twice), iso-propanol, 96 % EtOH, 80 % EtOH, 70 % EtOH, 50 % EtOH, and bi-distilled water. Dewaxed slices were stained with haematoxylin (Dako REAL[™]) for one minute (subsequently immersed in tap water five minutes twice and rinsed with bi-distilled water) and eosin (0.1% in diluted acetic acid solution) for five minutes (subsequently immersed in bi-distilled water for 3 minutes, twice). Stained slices have been dehydrated by ascending alcohol series and permanently fixed with Roti[®]-Histokitt. The stained slices have been observed by light microscopy (Zeiss AxioLab microscope with Zeiss AxioCam color CCD camera and AxioVision software v.3.1.2.1, all Carl Zeiss AG, Germany), which allowed the observation of differentiated tumor structures. The histological characterization of kidney structures was realized following the same procedure with kidney cross slices.

2.2.10 Confocal Laser Scanning Microscopy (CLSM)

Confocal laser scanning microscopy is a widespread microscopic technique that allows measuring of focused and detailed fluorescence images with high resolution also from thick and light-scattering objects.¹⁸⁹ It was used for various pharmaceutical questions in the recent years.¹⁹⁰⁻¹⁹² CLSM imaging was carried out on a LSM 710 microscope (Carl Zeiss MicroImaging GmbH, Germany). Slices of freshly excised organs were prepared for the imaging procedure with a razor blade (app. 0.5 mm thick). Far red or NIR fluorescent dyes were excited with a 633 nm HeNe Laser (5 mW). The images were acquired using the ZEN 2009 software. As no excitation laser with longer wavelength than 633 nm was available, the fluorescence emission of the NIR fluorescent dyes was poor and it was thus impossible to measure NIR and far red fluorescent dyes simultaneously. However, NIR dyes could be measured alone by increasing the excitation laser power to 15 % (DY 676 was measured with 0.5% - 1%).

3 Results and Discussion

3.1 HPMA Copolymers (OPB Spacer)^d

Polymer drug carriers based on *N*-(2-hydroxypropyl)-methacrylamide (HPMA) copolymers belong undoubtedly to the most intensively studied water-soluble synthetic polymers.^{127,193-196} Although various applications have been investigated,¹⁹⁷ most HPMA polymer drug conjugates were studied for the treatment of cancer, with a special focus on the site-specific delivery of cytotoxic and anti-inflammatory agents into tumor tissues or cells.^{127,195} The potential of the polymeric prodrugs, especially those intended for treatment of solid tumors, could be significantly improved by increasing the molecular weight (M_w) of the polymer carriers.^{198,199} Sufficiently high M_w of the polymer carrier is supposed to cause passive accumulation of the polymer drug conjugate in solid tumor tissues due to the EPR-effect.^{67,71}

Although efficient passive tumor accumulation of polymer drug conjugates is a prerequisite for tumor-targeted therapy, the efficacy of the treatment is also dependent on tumor specific drug release. Various conjugation strategies have been developed to increase the tumor specificity of polymer drug conjugates, leading to an enhanced efficacy and reduced toxicity of the polymer conjugate prodrugs.^{127,200,201} The most common ones are hydrazone spacer or acetal spacer for pH sensitive release,²⁰²⁻²⁰⁵ disulfide spacer for reductive release^{206,207} and peptide spacer for release by tumor-specific enzymes like cathepsin B^{208,209}. In the last decade it has been demonstrated that synthetic conjugates based on HPMA copolymers containing the cytotoxic drug doxorubicin (DOX) bound via pH-sensitive and hydrolytically degradable hydrazone bond are highly potent drug-delivery systems for chemotherapy.^{205,210} These DOX-containing conjugates were stable in aqueous solution at a physiological pH of 7.4 but the drug was rapidly released in buffers at pH 5 - 6.5, simulating acidic pH in endosomes and lysosomes of cancer cells. Later on, high-molecular-weight (HMW) HPMA copolymer drug conjugates with branched, grafted or star-like architecture and

^d These results have been published:

Hoffmann S, Vystřilová L, Ulbrich K, Etrych T, Caysa H, Mueller T and Mäder K. Dual Fluorescent HPMA Copolymers for Passive Tumor Targeting with pH-Sensitive Drug Release: Synthesis and Characterisation of Distribution and Tumor Accumulation in Mice by Non-invasive Multispectral Optical Imaging. *Biomacromolecules* 2012; 13(3): pp. 652-663.

with pH-sensitive drug release mechanism have been synthesized and tested for anticancer activity.²¹¹

Polymers with star-like architecture arouse particular interest in biomedical applications and several structures have already been synthesized in the last decade.^{57,212,213} Higher molecular weights of such branched HPMA conjugates improved their therapeutic efficacy notably.^{199,214,215} This effect can be ascribed to higher accumulation of the polymers in tumor tissue due to the more pronounced EPR effect. However, the detailed *in vivo* fate of those drug delivery systems is not completely understood yet. Several studies were realized to elucidate the *in vivo* fate of polymeric drug delivery systems, but the use of imaging techniques as SPECT and PET allowed only an observation of the biodistribution for few hours to days, due to the short half-life of the used tracers.^{103,216,217} In this work multispectral FLI has been used to follow the long term *in vivo* fate of several HPMA copolymer based drug delivery systems, which allowed long observation times up to several months.

3.1.1 Synthesis of Dual Fluorescent HPMA Copolymers with pH-Sensitive Drug Release (OPB-Spacer) and Physicochemical Characterization^e

Two different structures of HPMA-based polymer drug carriers have been synthesised: a linear structure with a molecular weight of ~30 kDa and a star-like structure of ~200 kDa (Table 4).

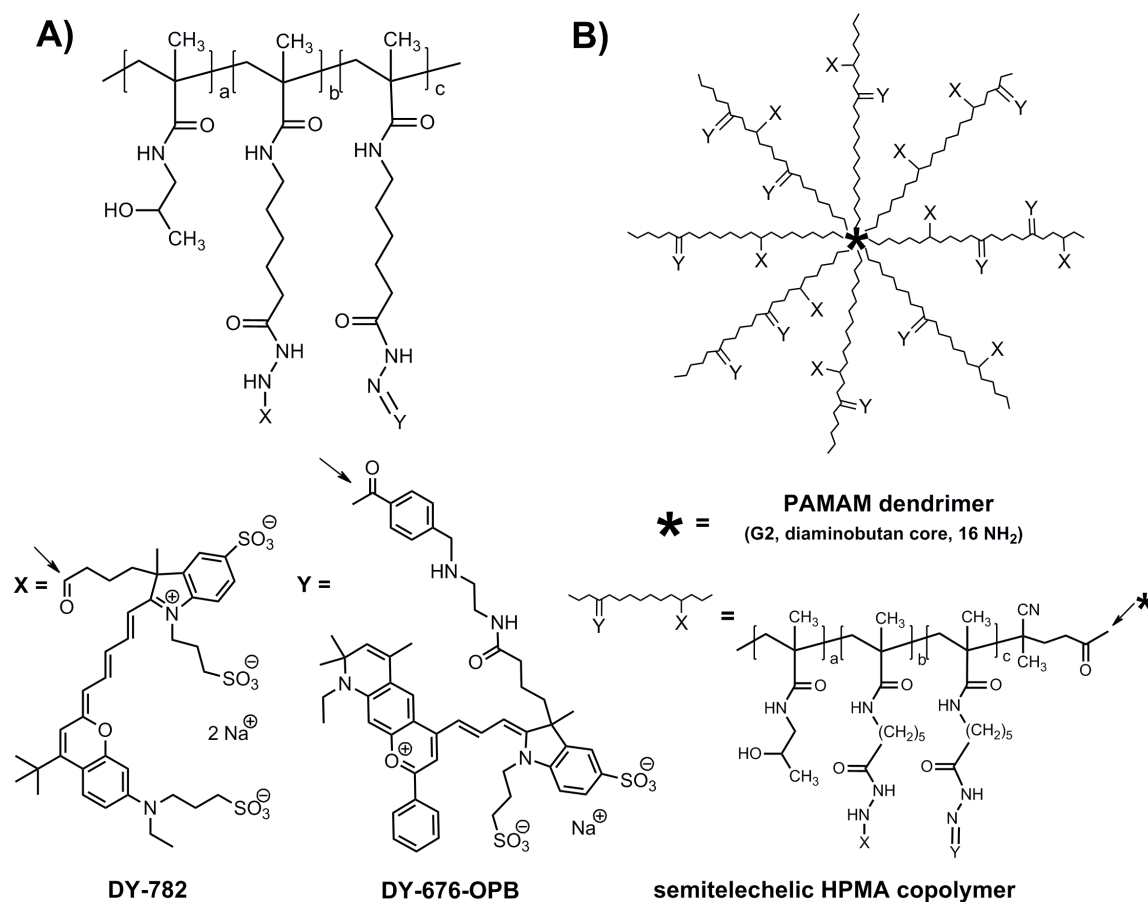
Table 4. Characteristics of HPMA precursors and conjugated polymers.

Architecture	HPMA precursors			Dye content (wt. %)	
	M_w (Da)	M_w/M_N	R_H (nm)	DY-676	DY-782
Linear polymer	27,200	1.74	4.3	1.6	0.7
Star-like polymer	186,000	1.76	12.7	1.4	0.7

The high molecular weight (M_w) fulfilled the prerequisite criteria for enhanced accumulation of the polymers in solid tumors due to the EPR effect.²¹⁸ The elimination of

^e Synthesis of polymers, all physicochemical characterizations and *in vitro* release experiments: Institute of Macromolecular Chemistry AS CR, v.v.i., Heyrovský Sq. 2, 162 06 Prague 6, Czech Republic (T. Etrych and L. Schindler, née Vystrčilová).

these polymers is considered to be notably different because the linear structure has a molecular weight below renal excretion threshold, whereas the star-like structure cannot be excreted by the kidneys. Two fluorescent dyes with different emission wavelength maxima in the near-infrared (NIR) and far red (FR) part of the spectrum were coupled to HPMA copolymer precursors. The general structures of the used polymers are presented in Scheme 3. Using NIR and FR fluorescent dyes allowed to obtain information about the distribution also from deep tissues like liver, spleen and kidneys in the following imaging experiments.¹⁴⁶ The FR-fluorescent dye DY-676 was conjugated with the polymers via a pH-sensitive hydrolytically degradable hydrazone bond and served as a pH-dependent cleavable drug model. 4-(2-oxopropyl) benzoic acid served as a spacer between the polymer and the releasable dye. The NIR-fluorescent dye DY-782 was conjugated with the copolymer carrier backbone via a noncleavable hydrazide bond to serve as a noncleavable polymer label. A detailed description of the polymer synthesis has been described in the literature.²¹⁹



Scheme 3. Structures of linear (A) and star-like (B) HPMA copolymer-dye conjugates.

The cooperation partners determined molecular weights, polydispersity and hydrodynamic radii by GPC / HPLC Shimadzu system equipped with UV-VIS (Shimadzu SPD-10AVvp), refractive index Optilab-rEX and multi-angle light scattering DAWN EOS detectors (both Wyatt Technology Co). The eluent was 0.3 M sodium acetate buffer pH 7.4 for the Superose 6 HR 10/30 column and methanol - sodium acetate buffer (80:20 v/v) for the TSKgel G4000SWxl column; flow-rate 0.5 mL/min. The total content of the dyes in polymer conjugates was determined spectrophotometrically on a Helios α spectrophotometer (Thermochem). Molar absorption coefficients of the DY-782 ($\epsilon_{782} = 170\,000\text{ L mol}^{-1}\text{ cm}^{-1}$ (ethanol)) and DY-676 ($\epsilon_{676} = 180\,000\text{ L mol}^{-1}\text{ cm}^{-1}$ (ethanol)) were used to calculate the dye content. The R_h of the polymer coil of the star-like polymer precursor in aqueous solution was 3-fold higher than that of the linear polymer precursor (Table 4). The molecular weights and hydrodynamic radii were determined from the polymer precursors (non-conjugated polymers), as a determination of these values was impossible with the final conjugated polymers due to interferences of the fluorescent dyes with the instruments laser.

The principle of pH-dependent release of the cleavable drug model was proven *in vitro* at 37 °C.²¹⁹ As expected, the drug model release was observed to be much higher at pH 5 than that observed at pH 7.4 (76 % of DY-676-OPB released within 1 h at pH 5 in comparison with only 12 % released in a buffer of pH 7.4). There was no significant difference observable in the release rates from the carriers differing in polymer architecture. There was no hint for any release of the polymer chain label DY-782 during the incubation of the conjugate in the buffers, proving the stability of the hydrazide bond between DY-782 and the polymer carrier *in vitro*.

3.1.2 Optimization of Measurement Settings

The absorption maxima of the fluorescent dyes used in this work differed by more than 100 nm (DY-676 has an absorption maximum of 676 nm and DY-782 has an absorption maximum of 782 nm, the respective fluorescence spectra are red-shifted). Thus the resulting fluorescence spectra should be clearly separable by the instruments software. However, the fluorescence spectra of 2 $\mu\text{g/mL}$ dye in PBS depended notably on the used instruments filter sets (Figure 4). The reason is based in the properties and sensitivity of the instruments tunable liquid crystalline filter. Furthermore, a bathochromic spectral shift of approximately 5 nm was observed when the dyes were bound to the

polymer. These shifts were too small to be analyzed by the software and this effect has neither been further investigated in detail nor considered in further analyses.

An optimum separation and sensitivity for both dyes was found by using a combined measurement with “Red” and “NIR” filter sets (Figure 4). Unfortunately, when measuring a combination of both fluorescent dyes, it was impossible to subtract the autofluorescence from the measured fluorescence image, as the shape of the autofluorescence spectrum was too close to the combined spectra of both dyes to be separated by the underlying software algorithm (Figure 4C). The mouse autofluorescence is negligible in the NIR part of the spectrum, but in the following *in vivo* experiments it contributes about 5 % of the initial fluorescence intensity to the DY-676 signal (measured after administration of 1 mg polymer).

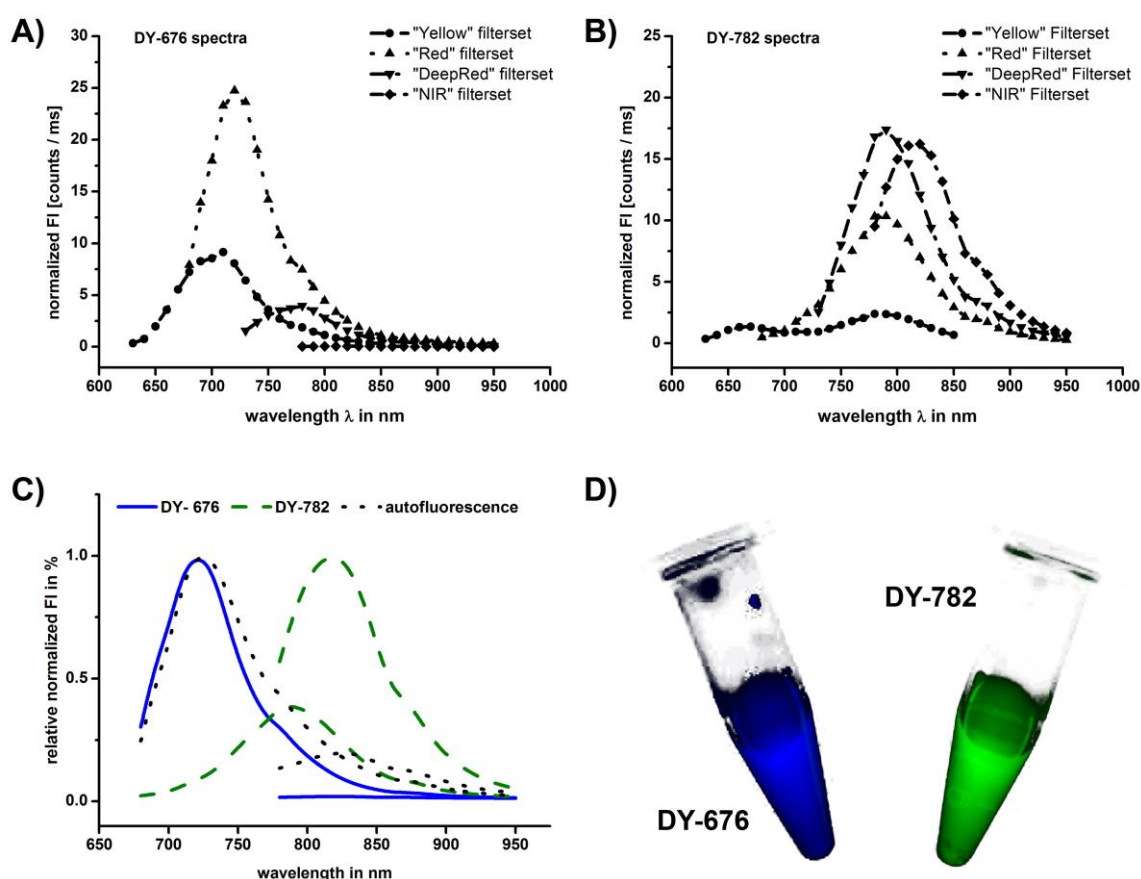


Figure 4. Fluorescence emission spectra from the drug model (A: DY-676) and the polymer label (B: DY-782) depended on the instruments filter set. The fluorescence image from a solution of both dyes (D) could be clearly separated into its spectral species using a combination measurement with the “Red” and the “NIR” filter set (C).

3.1.3 Biodistribution and Elimination in Mice

HPMA copolymers are investigated for years in preclinical and clinical studies.^{127,194,195} These polymers can be regarded as safe in experimental animal studies. Therefore, characterizations concerning the *in vitro* toxicity, safety and biocompatibility of the developed polymer conjugates are not addressed in this work.

The use of two different fluorescent dyes in combination with multispectral FLI allowed non-invasive characterization of the accumulation of the polymer carriers and of a pH-sensitive bond-coupled fluorescent drug model at the same time. Thus it was possible to obtain simultaneous information on biodistribution and elimination from both, the drug model and the carrier backbone from the polymers. The biodistribution was investigated after intravenous administration of 1 mg polymer per mouse in groups of four nude female mice (SKH1-*Hr^{hr}*, 2 – 4 month old). One mice of each group was sacrificed one day after polymer injection for a more detailed view on the biodistribution of the polymers in autopsied organs, whereas the other 3 mice were constantly imaged over a period of 80 days. This long observation time is clearly an advantage compared to other studies that were limited to few hours.^{103,216,217} The fluorescence image cubes were processed as described previously (cp. chapter 2.2.6.3, p. 21). Typical intensity weighted fluorescence component images are presented in Figure 5.

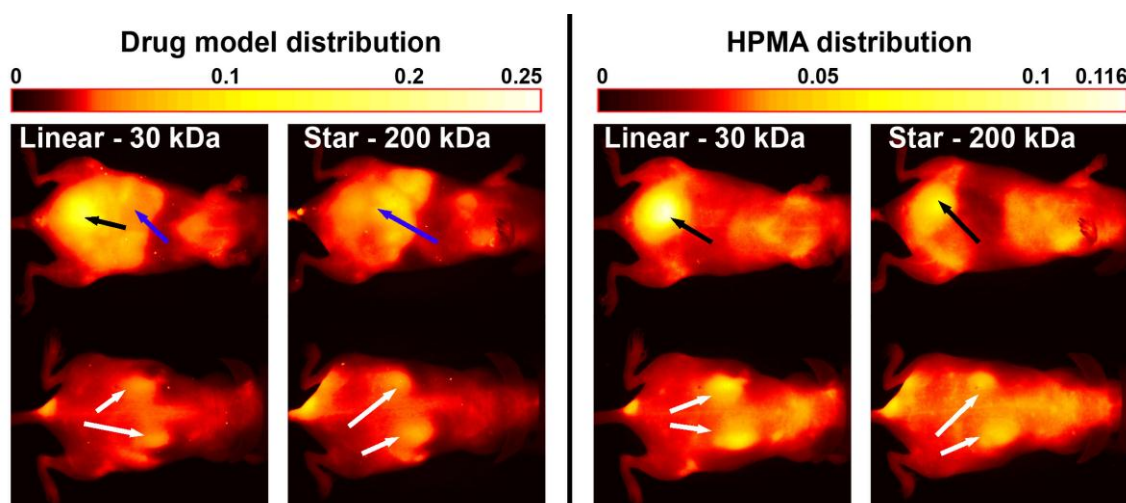


Figure 5. Distribution of the cleavable drug mode (left) and the HPMA copolymers (right) in mice six hours after *i.v.* administration of 1 mg linear HPMA (30 kDa) or star-like HPMA (200 kDa) in abdominal (top) and dorsal (bottom) images. Arrows mark bladder (black), kidneys (white) and intestine (blue).

After injection, both polymers immediately distributed all over the mouse body. Already five minutes after injection, an intensive fluorescence signal from both dyes (polymer label and cleavable drug model) was detectable in the bladder, indicating renal elimination. In case of the star-like HMW polymer the bladder fluorescence could be ascribed to the small portion (up to 15%) of semitelechelic polymer, which was not grafted to the central dendrimer core. After two hours, an intensive signal of the drug model was detectable from the intestine. As there was no signal for the polymer-attached fluorescent dye (DY-782) from the intestine, it can be concluded that the drug model is quite rapidly splitted off the polymer and that it is excreted via hepatic and renal elimination pathways. Interestingly, there was no particular accumulation in liver and spleen detectable compared to other organs, which is a major advantage over most nanoparticulate drug delivery systems that often show very strong accumulation in liver and spleen due to uptake of the drug delivery systems by the reticulo-endothelial system.^{154,220,221}

Both polymers showed intensive accumulation in the kidneys already five minutes after injection. To exclude the possibility of a specific accumulation of the fluorescent dyes, three mice were treated with free DY-676-OPB and free DY-782 (control). Although a slight kidney accumulation was observed during the first hours due to excretion of the dyes, both dyes were rapidly excreted and the fluorescence intensity decreased to the autofluorescence level of the mice within 26 hours. It can be concluded that the kidney accumulation is likely a property of the investigated HPMA copolymers. Kidney accumulation was already previously observed for various other HPMA copolymers.^{216,217,222} No mouse showed any pathologic effects from this accumulation. Interestingly, in dorsal images a polymer accumulation in kidneys was still observable, when the abdominal images did not show any accumulation in the bladder. This indicates a specific interaction between the polymer and the kidneys.

The fluorescence intensity of the cleavable drug model decreased independently from the polymer architecture. 22 hours after injection the fluorescence intensity decreased to 9.5 % of the highest measured intensity for the linear polymer and 12.3 % for the star-like polymer. After 46 hours the signal decreased to about 5 % of the initial intensity, which is the autofluorescence level of the mice in this part of the spectrum (Figure 6). It can be concluded that the drug model was completely eliminated during two days after injection. Its elimination is controlled by the rate of its release from the polymer carrier during circulation. Interestingly, the fluorescence intensity of the polymer and drug model increased during the first hours after injection especially for the star-like polymers.

This could be explained either by a time dependent distribution into small blood vessels in the skin, which would result in higher fluorescence or by the possibility of quenching effects, when the drug model is bound to the polymer. The elimination of the drug model could be fitted for both polymers assuming a 1st order exponential decay. The calculated half-life was comparable for both polymers (0.3 days for both polymers, Figure 6).

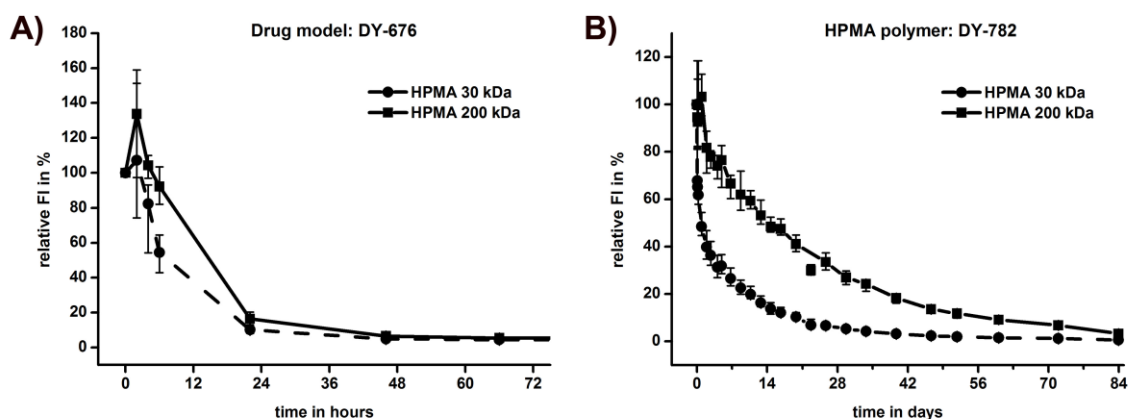


Figure 6. Elimination of the cleavable drug model (A) and the HPMA carriers (B) after intravenous administration of 1 mg polymer to healthy nude mice ($n=3$, the data represent means \pm minimum and maximum values).

An influence of the polymer structure on the body distribution was not detectable, but the elimination of the polymers was dependent on polymer architecture and size, as it had been observed in other studies.^{218,223} Whereas the fluorescence intensity of the non-cleavable dye (DY-782) from the linear polymer decreased below 50 % of the initial intensity after one day (48.5 %), 14 days were required for the bigger star-like polymer until the remaining fluorescence intensity decreased below this value (48.4 %, Figure 6). As expected, the circulation time was much longer for the HMW star-like polymer. This can be explained by the much higher average molecular weight of the star like polymer (~200kDa) and the more rigid polymer skeleton. Whereas the smaller linear polymer is still below renal elimination threshold, the star-like polymer cannot be directly excreted by the kidneys. The elimination kinetic of both polymers could be fitted assuming a 2nd order exponential decay that might be explained with both possible elimination pathways for the HPMA copolymers: renal (mainly in the first hours after injection and for the small molecular weight fraction) and hepatic clearance of the polymer. As the synthesized HPMA copolymers are not biodegradable, a major influence of hepatic elimination can be assumed, especially for the star-like polymer. However, the star-like polymer is composed of several linear chains that are conjugated to a PAMAM dendrimer core via

an amide bond that might be slowly degraded. The resulting linear chains would then be excretable by the kidney. This assumption is supported by the fact that the non-cleavable polymer label was detectable in the mouse bladder 6 h after polymer injection due to a small proportion of semitelechelic polymers (cp. Figure 5).

3.1.4 *Ex Vivo* Fluorescence Imaging: Extracted Organs

One mouse of each group was sacrificed one day after polymer injection and the organs were extracted and fluorescence images of relevant organs were recorded and analyzed (Figure 7).

At this time, the drug model fluorescence intensity decreased already to ~10 % of the initial intensity. Thus notable autofluorescence contribution to the drug model spectral component image needs to be taken into consideration. Further, it is obvious that dark colored organs with high blood content like liver, spleen and heart absorb more light from the drug model (DY-676) than the other organs. The difficult comparability of fluorescence images from differently colored objects seems to be an inherent disadvantage of FLI compared to other imaging techniques. However, the images reveal that both, drug model and polymer show increased fluorescence intensity from the kidney, which was not observable in the organs of a non-treated control mouse. The high intensity of the drug model in the kidneys may be measured due to excretion processes, but another possibility would be that the accumulated polymers do still contain conjugated drug model.

Further, no clear difference in drug model or polymer biodistribution is observable between the two polymer architectures, which confirms the *in vivo* results. Apart from the kidneys, the polymer carriers distribute quite homogeneously in the mouse organs. Especially liver and spleen do not show a more pronounced uptake of the polymers compared to the other organs. Accumulation in liver and spleen is a major disadvantage of most nanoparticulate drug delivery systems. These often extensively accumulate in these organs after removal from the blood stream by the reticuloendothelial system, mainly by macrophages and Kupffer cells. This effect is undesired as it will lead to increased elimination and liver toxicity.^{220,221} It is a clear advantage of HPMA copolymers to evade the nonspecific uptake into the liver or spleen, which can be attributed to the small size and flexibility and also to the very hydrophilic properties.^{224,225}

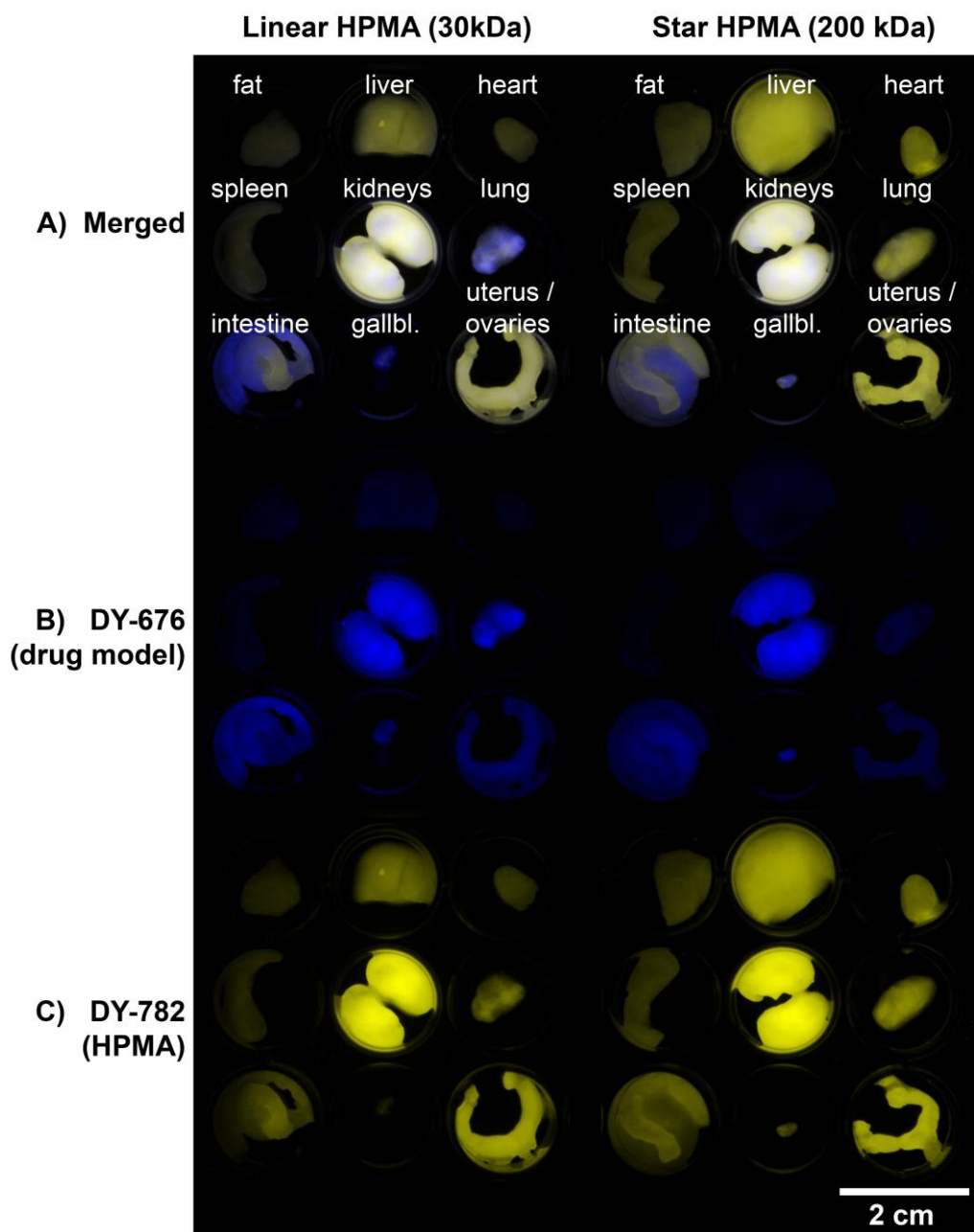


Figure 7. Pseudo-colored spectral component images of a fluorescence image from extracted mouse organs one day after polymer injection. **A:** mixed signal; **B:** drug model fluorescence signal; **C:** HPMA copolymer fluorescence signal.

3.1.5 Characterization of Kidney Accumulation

The biodistribution study in mice and the autopsied organs revealed a specific high intensity of the polymer bound fluorescence dye from the kidneys. This high local and specific fluorescence of the polymer label was still detectable after one week *in vivo*. To

enlighten the mechanism and the exact accumulation site, mice were injected with 1 mg of the polymers and the kidneys were extracted 22 h after injection to be imaged with the highest possible magnification (Figure 8).

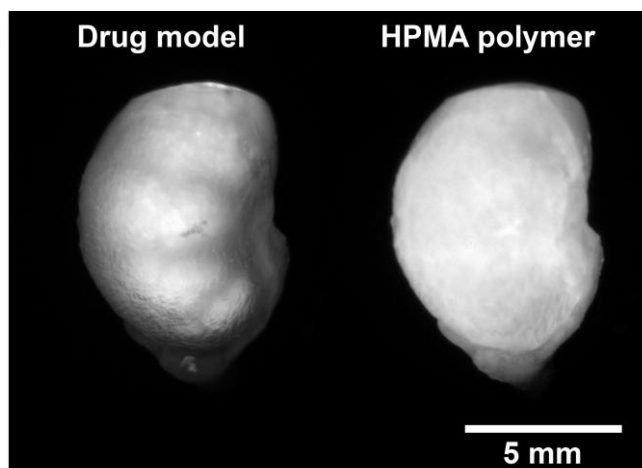


Figure 8. Fluorescence component images (grayscale) from the kidney of a mouse treated with 1 mg Star-HPMA (200 kDa) in highest possible resolution. **Left:** drug model signal, **right:** polymer signal.

Whereas detailed structures are visible from the red fluorescent drug model, the image resolution in the image from the NIR-fluorescent dye is coarse due to multiple scattering effects of NIR-light.¹⁴⁶ It is visible that the drug model fluorescence comes from specific regions inside the kidney, whereas the polymer fluorescence seems to be more homogeneously distributed in the kidney. This observation was confirmed in transverse kidney slices, which were produced with a razor blade and had a thickness of approximately 0.5 mm (Figure 9). The fluorescence signal of the drug model is located in specific structures in the medulla. Otherwise, the accumulation of the polymers is located mainly in the cortex of the kidney. It is very unlikely, that the polymer shows a high fluorescence in the kidney due to excretion processes, because a corresponding high fluorescence signal from the bladder is missing in the *in vivo* images. Most probably, it could be ascribed to the interaction of polymer with the glomerular basement membrane in the cortex. Most likely, hydrazide groups of the polymer could interact with the highly anionic membrane, which is composed of a collagen based network containing laminin, entactin and proteoglycan (with high heparin and chondroitin sulfate content).²²⁶

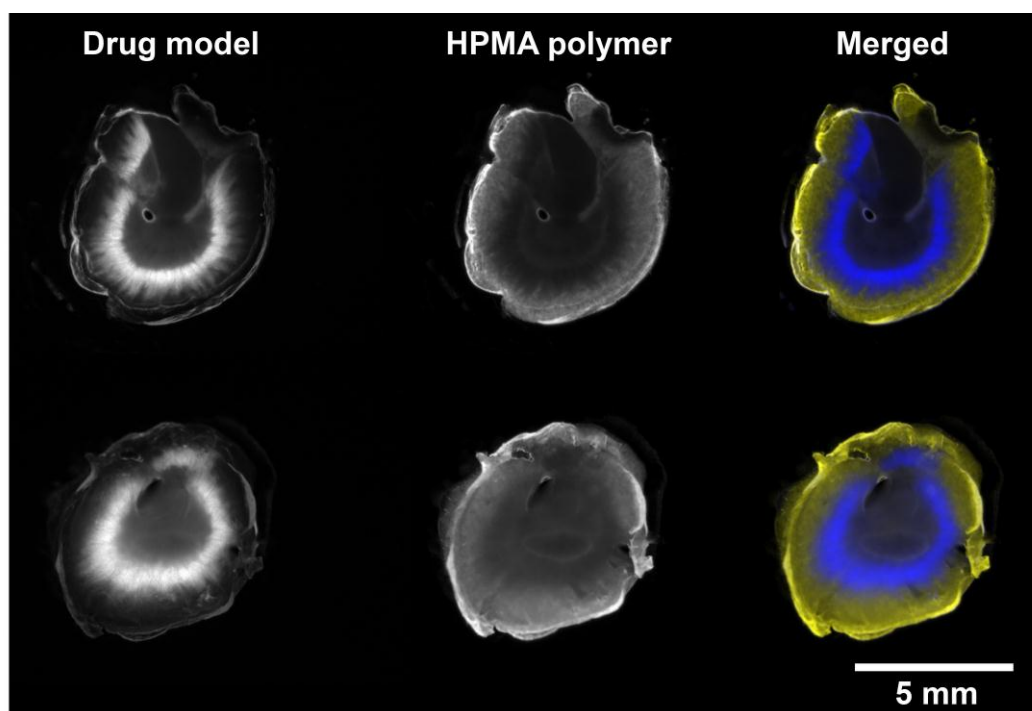


Figure 9. Fluorescence images from cross slices of the kidney from mice treated with the linear (top) or the star-like (bottom) HPMA copolymer. **Left:** drug model fluorescence signal; **middle:** polymer carrier fluorescence signal; **right:** pseudo-colored composite image (blue: drug model; yellow: polymer carrier).

Confocal laser scanning microscopy was done to confirm the MaestroTM imaging results. Fluorescence of the drug model was excited with a 633 nm HeNe-laser and measured at the emission range of DY-676 (639 nm – 758 nm). The polymer label could not be detected next to the drug model, as no laser with longer wavelength was available. The drug model was detected in specific structures in a central part of the kidney cross slice (Figure 10).

The images of kidneys from mice treated with the linear or the star HPMA were comparable. Unfortunately, the instrument set-up of the used confocal laser scanning microscope did not allow analyzing the sample with light microscopy. To compare the structures found in the CLSM image with a microscopic view, kidneys from mice treated with the polymers were extracted, sliced, fixed in a solution of 4 % paraformaldehyde, embedded in paraffin, dewaxed and stained with haematoxylin and eosin. Using light microscopy, morphologically comparable structures could be observed and identified as medullary rays (Figure 11).

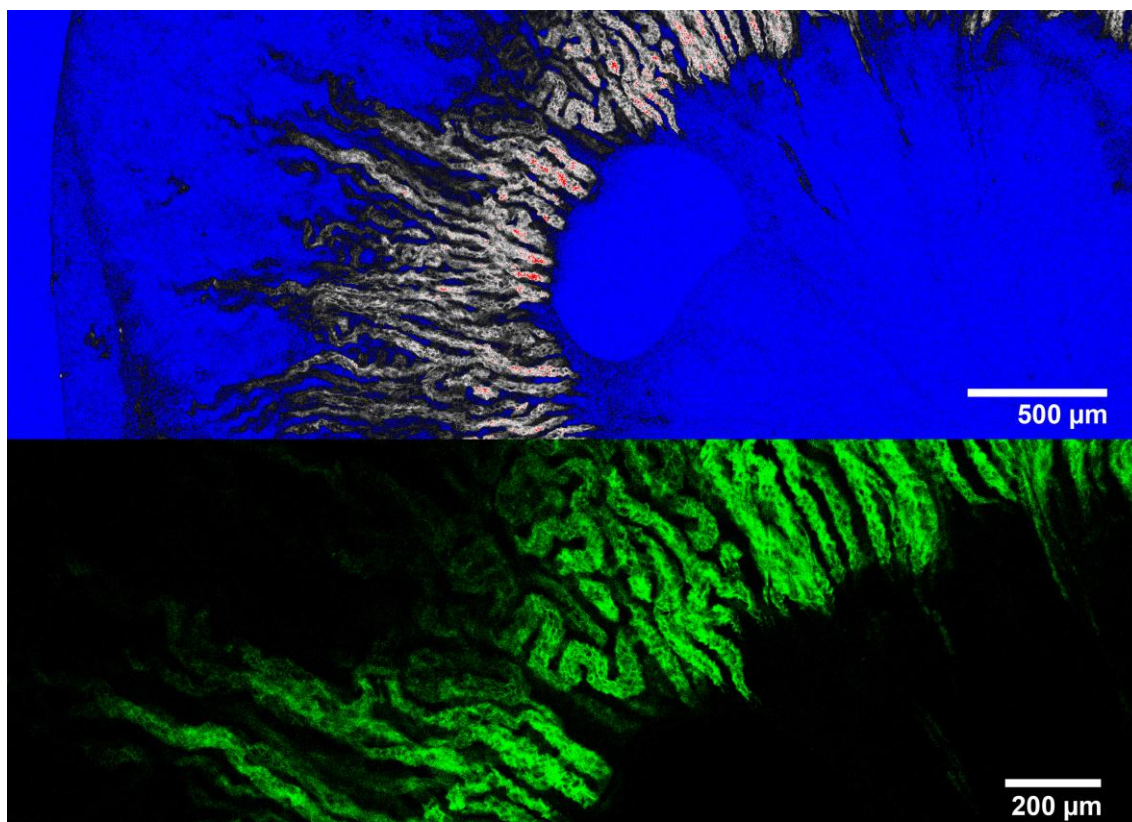


Figure 10. CLSM images of the drug model signal from kidney cross slices of a mouse treated with the linear HPMA copolymer conjugate (sacrificed one day after injection). **Top:** range-image of the slice (blue = no fluorescence, white = high fluorescence). Fluorescence is detected from specific central structures, most likely from the medullary rays. **Bottom:** pseudo-colored CLSM-image of fluorescent structures in the kidney.

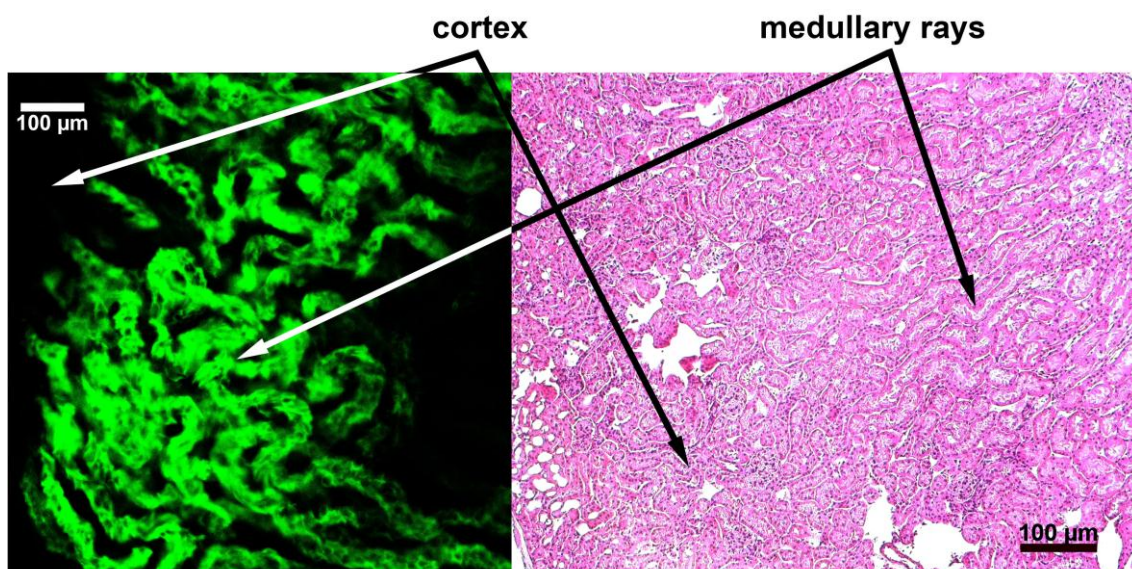


Figure 11. Kidney slices from a mouse that was sacrificed one day after injection of 1 mg star-like HPMA copolymer conjugate. **Left:** CLSM-image of specific fluorescent structures. **Right:** HE-stained microscopy image with comparable structures.

The fluorescence of the drug model was unfortunately lost during the embedding and staining procedure. However, from the combined results of the fluorescence imaging and confocal laser scanning microscopy with light microscopy the following facts can be concluded:

- The polymers accumulate in the kidney's cortex, likely due to a specific interaction of the hydrazides with the glomerular basement membrane.
- The drug model has already been cleaved from the polymer, as the fluorescent signals come from different parts of the kidney.
- The drug model is located in the medullary rays, which may be a consequence of excretion and / or a dye-specific interaction with the sub-microscopic structures of the medullary rays.

3.1.6 Tumor Accumulation Studies (*In Vivo*)

Passive tumor accumulation using HMW polymeric drug carriers due to the EPR effect of tumor vasculature has been first described more than 25 years ago⁶⁷ and is a well-accepted approach today.⁷¹ Due to the long circulation time in healthy mice a considerable accumulation of the new HPMA copolymers in solid tumors was expected. The passive tumor accumulation is based on the enhanced permeability of some of the blood vessels and on the retention in the tumor tissue due to insufficiently developed lymphatic clearance from the tissue. The morphological blood vessel abnormality in tumors is based on the increased growth rate and hasty and non-physiological neovascularization in tumors.²²⁷

3.1.6.1 Xenograft Tumor Models

Well known and accepted models to investigate tumors in animal studies are xenograft tumor models.²²⁸ In these models, immunodeficient mice or any other immunodeficient animals are injected with human tumor cells, which grow in the host body and form solid tumors due to the lacking immune response. The principle was first reported in 1971.²²⁹ Xenograft tumor models can be installed locally in an ectopic model (often non-metastasizing) for instance by subcutaneous (s.c.) or intraperitoneal (i.p.) injection of cell suspensions or they could be installed at the site of tumor cell origin (orthotopic model) or they could be intravenously injected (systemic model). Ectopic models lack of realism, as the site of action is artificial and no metastasis occurs. Orthotopic tumor models are a

more realistic model, as the tumors metastasize and grow at a clinically more realistic site in the body.²³⁰⁻²³³ However, testing substances at this early stage in explorative experimental animal studies requires an easier model for better accessibility and comparability. For instance, the site of tumor growth and vascularization should be comparable and tumor size should be easily accessible. Therefore, s.c. tumor models have been chosen to be installed in immunodeficient nude mice. Athymic nude mice were chosen as they have no cellular immune response and the human tumors are grown in the mouse host body. Human xenograft colon carcinomas (DLD-1 and HT-29) have been successfully inoculated in athymic mice (Figure 12). These tumors are known to develop necrotic areas due to insufficient vascularization, including acidic microenvironment due to enhanced metabolism. In principle, two release mechanisms of the drug model could be discussed: First, an enhanced cleavage of the acid-sensitive hydrazone-bond locally inside the tumors due to the acidic microenvironment. The second possibility is the internalization of extravasated HPMA copolymer drug conjugate by the tumor cells.²³⁴ Intracellularly, the drug model could be cleaved in endosomes and lysosomes. Both processes should result in a local accumulation of the drug model in the tumors.



Figure 12. Athymic nude mice which was subcutaneously inoculated with human colon carcinomas at the right (DLD-1) and left (HT-29) flank.

3.1.6.2 Imaging of Tumor Bearing Mice

The mice were randomized into two groups at day 19 after tumor injection according to their tumor size. The tumor sizes in both groups were comparable (Figure 13). 21 days after tumor cell inoculation, both dual fluorescent HPMA copolymers were intravenously injected at a concentration of 1.5 mg per mouse ($n=3$ per group). At this time the solid and palpable tumors had already a volume of $0.85 \pm 0.22 \text{ cm}^3$ (DLD-1) and $0.55 \pm 0.21 \text{ cm}^3$ (HT-29). After six days a second dose of 1.5 mg polymer per mouse

was administered. Two days after the second injection all mice had to be sacrificed due to the tumor burden. At this time, the mice had lost about 10 % of their initial weight due to the tumor growth. The elimination kinetic of the polymers and the drug model from the mouse body was observed in abdominal mouse images and found to be identically with biodistribution and elimination studies in SKH1 mice. However, it was found that the drug model accumulated in the tumors for a much longer time, which was evident in a high local fluorescence in the tumors (Figure 14).

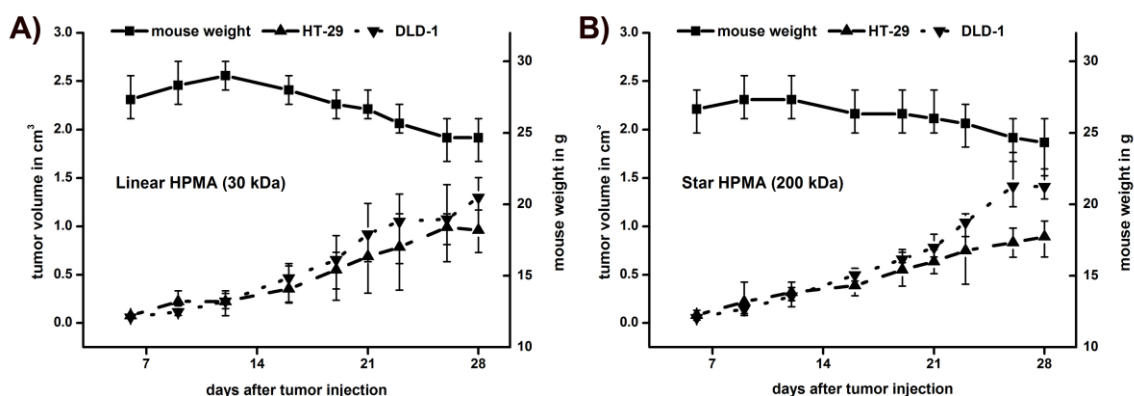


Figure 13. The size of the subcutaneous xenograft tumors was comparable in both mouse groups (A: linear HPMA 30 kDa and B: star-like HPMA 200 kDa). Data represent means \pm SD.

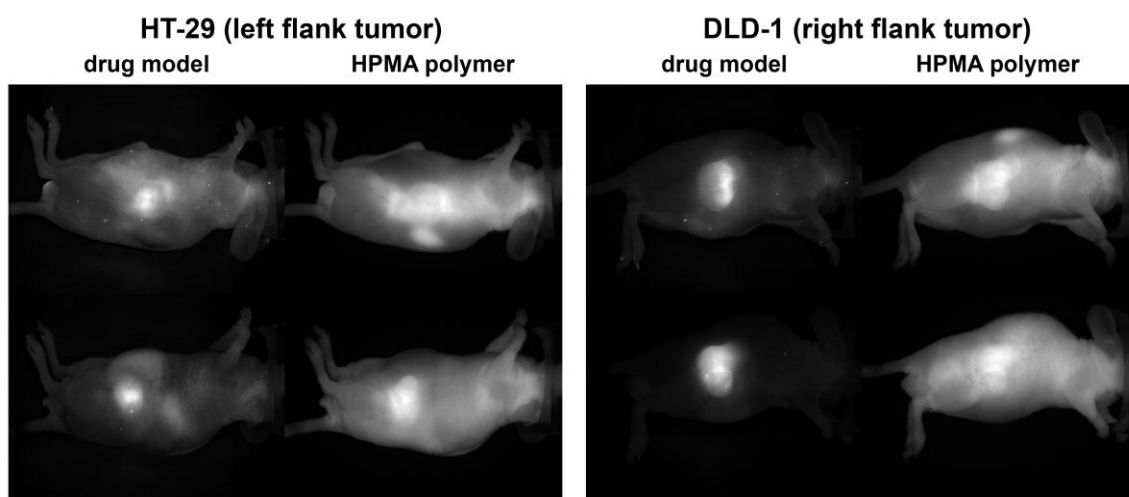


Figure 14. Grayscale fluorescence spectral component images of tumor bearing mice two days after polymer injection. Upper row: Linear HPMA, lower row: star-like HPMA. The polymers and the drug model are specifically delivered to the tumors but also accumulated in the kidneys.

Nonetheless, the total amount of drug model remaining in the tumor was comparably small, which can be certainly ascribed to the rather fast cleavage of the drug model from the polymer backbone. Further, the remaining drug model fluorescence intensity depended on the tumor model and on the polymer (Table 5). Obviously, more drug model is accumulated in the tumor models, when the star-like polymer was used. Apart from both tumors, the drug model was completely removed from the mouse body two days after injection (Figure 15). It can be concluded that a certain amount of the drug model is retained specifically in the tumors, whereas it is rapidly eliminated from the mouse body. This effect may be exploited by multiple dosing of the polymer. For that reason a second dose of polymer was administered six days after the first injection. Furthermore, the drug model was often found to be non-homogeneously distributed within the tumor and accumulated in specific central regions of the tumor, especially in the DLD-1 model (Figure 16). Structural differences of the tumors may be discussed as a reason. Interestingly, the polymer seemed to be more homogeneously distributed within the tumor. This effect could be discussed as a more homogeneous distribution or as consequence of the lower resolution due to multiple scattering events.

Table 5. Remaining drug model intensity 49 h after injection of 1.5 mg polymers compared to the initial drug model fluorescence (5 min p.i.). Data represent mean remaining relative intensity of the initial intensity \pm SD.

Tumor model	Linear polymer (30 kDa)	Star polymer (200 kDa)
DLD-1	9.6 % \pm 3.0 %	30.7 % \pm 5.2 %
HT-29	4.7 % \pm 0.5 % (autofluorescence)	14.7 % \pm 1.1 %

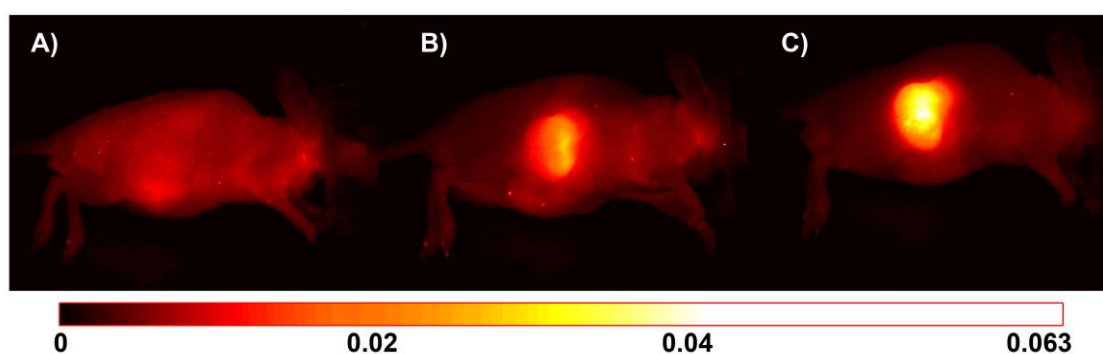


Figure 15. Drug model signal (DY-676) 49 h after injection. **A:** tumor bearing control mouse without injection (= autofluorescence), **B:** mouse treated with linear HPMA, **C:** mouse treated with star-like HPMA. The signal from the mice decreased to autofluorescence with exception of the tumor area (DLD-1).

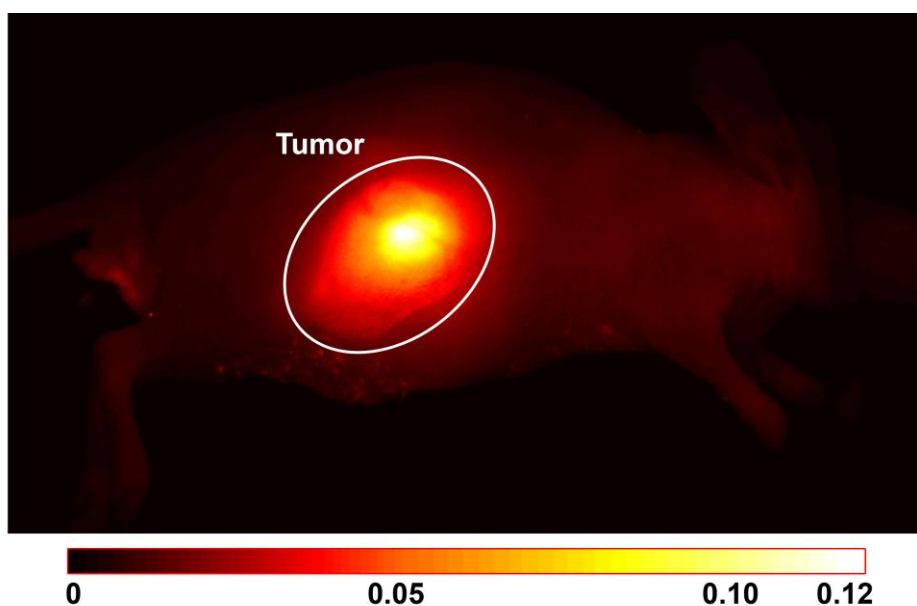


Figure 16. *In vivo* fluorescence component image of the drug model fluorescence from a mouse that was treated with the star-like polymer (24 h p.i.) The drug model fluorescence is non-homogeneously distributed within the tumor.

3.1.6.3 Development of a Method for Tumor Accumulation Comparability

For a better comparability of the tumor accumulation of the polymers and the drug model, it is not only necessary to compare the fluorescence images, but also to quantify the tumor accumulation in numbers. Therefore, a suitable method is required to extract a comparable value from the fluorescence images, describing the tumor accumulation.

It is one of the major disadvantages of FLI that there is no reliable quantification approach. This is based on the fact that too many variables like scattering effects, absorption, quenching effects and others like the position of the mice in the imager influence the measured fluorescence intensity. Consequently, a comparison of the tumor accumulations is possible only using a relative approach. The measured fluorescence intensity can be extracted from the image cubes either for each specific wavelength, or for the complete spectrum that was recorded. Using the full spectral component fluorescence intensity seems to be more suitable, as the fluctuations in the spectrum (e.g. due to different polarity of tissues) are eliminated. Thus, the area of the tumor can be selected and the fluorescence intensity measured from this area over the full spectrum can be extracted from the image. However, comparing these intensities between different mice is not advisable. For instance it is not guaranteed that the same amount of polymer circulated in each mouse. Although each mouse was injected with 100 μL polymer solution, the amount reaching systemic circulation varies due to the fact

that a small proportion of the solution remains locally in the surrounding tissue of the injection site.

Calculation of a Comparable “Tumor Accumulation Value” (TAV)

A specific relative calculation method was developed to analyze and compare the tumor accumulation of the HPMA copolymers and the drug model. The average fluorescence intensity (I) in the tumor region was normalized by the tumor area and exposure time (t_{exp}) and referred to the average fluorescence intensity of the remaining mouse body, which was also normalized with exposure time and area.

In detail, the TAV in this work is calculated as follows:

$$\textit{Tumour accumulation value TAV} = \frac{\textit{proportion of fluorescence signal}}{\textit{proportion of fluorescence area}}$$

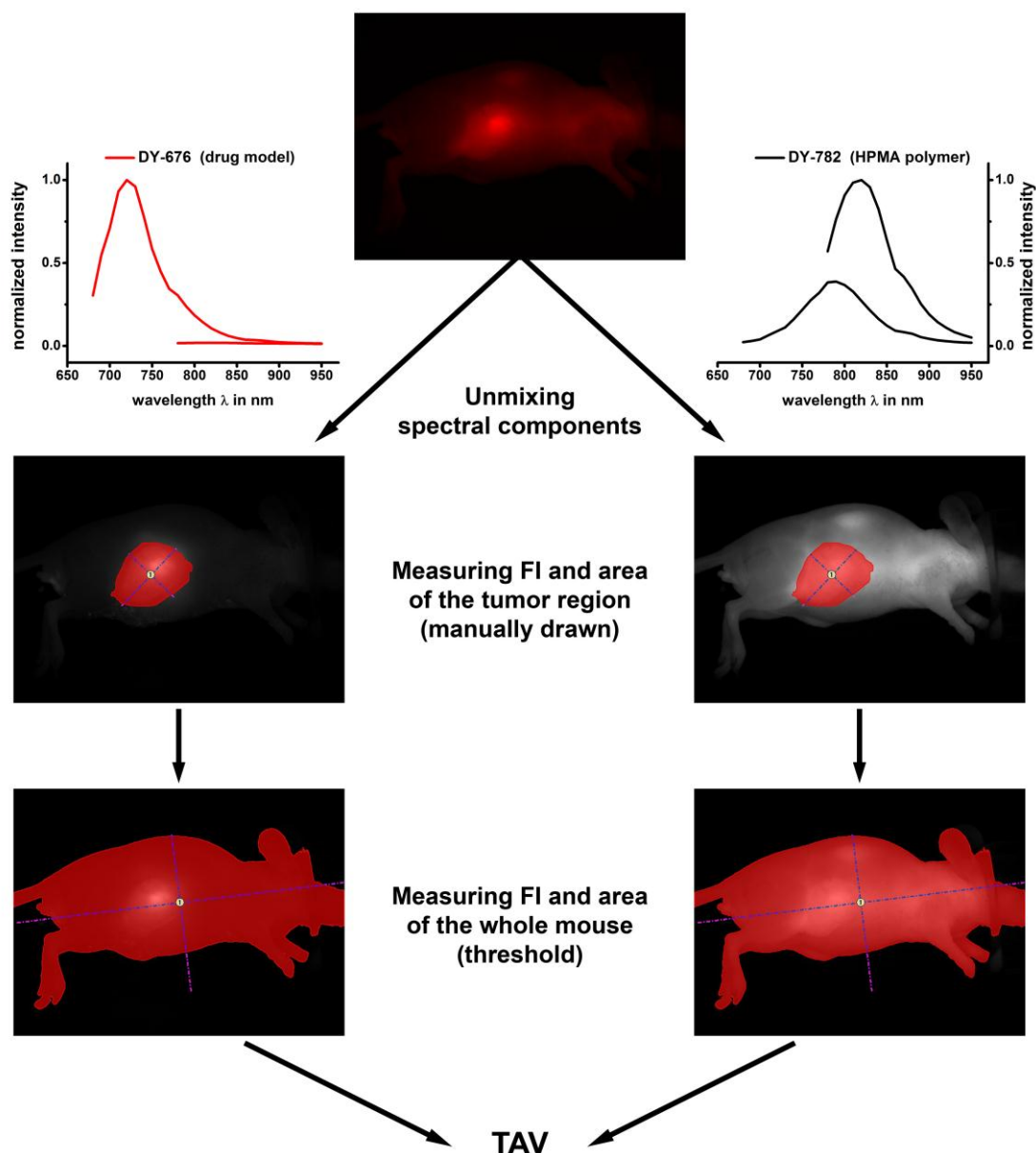
$$\textit{Proportion of fluorescence signal} = \frac{\frac{I_{tumor}}{t_{exp}}}{I_{mouse} - I_{tumor}} = \frac{I_{tumor}}{I_{mouse} - I_{tumor}}$$

$$\textit{Proportion of fluorescence area} = \frac{area_{tumor}}{area_{mouse} - area_{tumor}}$$

$$TAV = \frac{I_{tumor} * (area_{mouse} - area_{tumor})}{area_{tumor} * (I_{mouse} - I_{tumor})}$$

The calculated value is independent from the exposure time. It expresses in a comparable number, how much stronger the fluorescence in the tumor area is compared to the remaining mouse body. It is a more robust parameter than absolute fluorescence intensities, which are dependent on the amount of injected polymer and intensity variations within the tumor or mouse body. The basic principle of TAV calculation from fluorescence mouse images is presented in Scheme 4.

The tumor region is determined manually, according to the border which is visible in the image. As the bright tumor also scatters light to the surrounding body, a systematic error source could be the underestimation of the tumor accumulation. On the other hand, the tumor tissue is rather bright compared to other tissues and thus reflecting more light, than for example the liver, which slightly overestimates the TAV.



Scheme 4. Measurement principle for the calculation of the tumor accumulation value for the polymer and the drug model in mice.

3.1.6.4 TAV: Comparison of Tumors and Polymers

The calculated relative tumor accumulation (TAV) of both HPMA copolymers was comparable and not dependent on the polymer architecture (Figure 17). Interestingly, the detected tumor accumulation of the cleavable drug model was higher for the star-like polymer. Over the time, the tumor accumulation of polymers increased steadily (Figure 18). For example, four hours after injection the TAV in the group of the linear polymer (30 kDa) was calculated to be 1.6 ± 0.10 in DLD-1 and it increased to 2.48 ± 0.7 during the next five days. This can be explained with the EPR effect: as the polymer is long

circulating in the blood a small fraction of could always be extravasated into the tumor and is retained there.

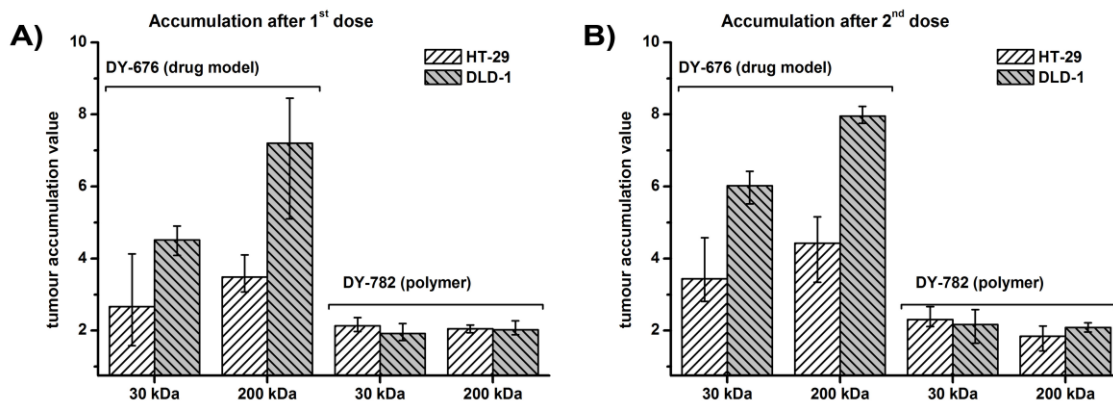


Figure 17. TAV two days after injection of the first dose (A) of linear and star-like polymer and two days after injection of the second polymer dose (B).

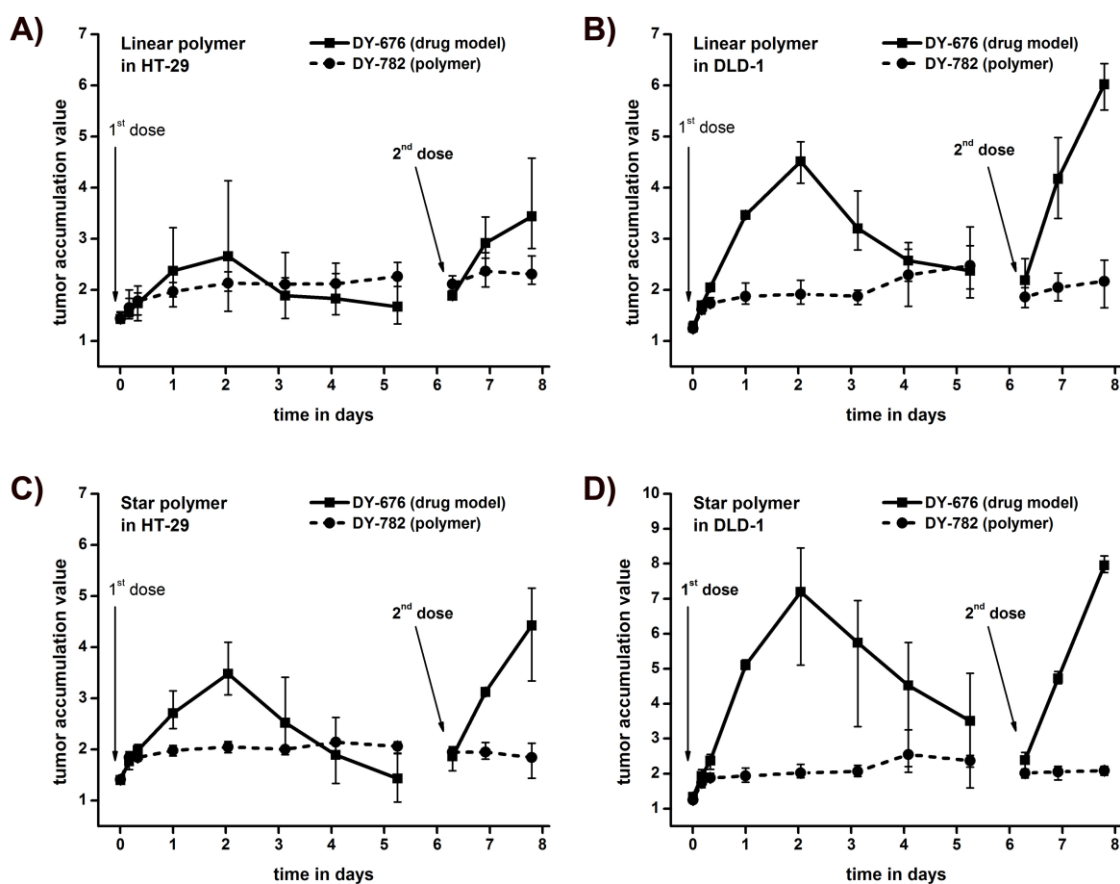


Figure 18. Time-dependent change of the TAV of the drug model and HPMA copolymers in DLD-1 and HT-29 xenograft model after administration of 1.5 mg linear (A and B) or star-like polymer (C and D) at day 0 and day 6.

The pH-sensitive coupled drug model (DY-676) showed a much stronger accumulation in the tumors, particularly in DLD-1, than the polymers (2 days after injection of the linear polymer 4.51 ± 0.40 for DLD-1 and 2.66 ± 1.30 for HT-29; two days after injection of the star-like polymer 7.20 ± 1.8 for DLD-1 and 3.48 ± 0.54 for HT-29). In opposite to the polymers there was an optimum drug model accumulation two days after injection and afterwards the TAV decreased, probably due to rapid elimination of the small molecule (Figure 18).

It may be supposed that due to an acidic microenvironment in the tumors the drug model is cleaved in the tumors and can diffuse inside the tissue. However, after two days most of the cleavable dye was already excreted and the overall amount in the tumor was rather small (cp. Table 5, p. 43). Administration of a second dose of polymer after six days even led to increased tumor accumulation of the drug model, because there was still drug model retained in the tumor, whereas it was eliminated from the blood stream already. However, an even better accumulation is expected if the drug model is released slower in the blood stream since the accumulation of the polymer took much more time than the release of the drug model.

Generally a better accumulation of the drug model can be observed in DLD-1 compared to HT-29. This may be ascribed to an increased growth rate of DLD-1 compared to HT-29 (cp. Figure 13, p. 42), which also results in a different tumor microstructure. The high tumor accumulation of the drug model after 49 hours (Figure 18) must be related to the low overall signal of DY-676 at this time (cp. Figure 6, p. 34). The images show that the drug model intensity in the mouse body at this time decreased to autofluorescence level already (cp. Figure 15, p. 43). While significant accumulation of polymer in tumors could be found after 12/24 h, in the same time interval more than 50-75% of drug model is already released. It is likely that the dye was cleaved before the polymeric carrier could accumulate in the tumor. Interpreting these results, an even better accumulation of the drug model is conceivable when the linker would be modified to be cleaved more slowly. Also, it is interesting that the polymer architecture seems to have no particular strong influence on the accumulation of the polymers in the tumor, but has an influence on the drug model accumulation.

3.1.7 Characterization of the Tumor Accumulation *Ex Vivo*

3.1.7.1 Maestro™ Fluorescence Imaging

The mice were sacrificed two days after administration of the second polymer dose due to tumor burden and the organs were immediately excised. At this time, the tumors had an average volume of $1.35 \pm 0.23 \text{ cm}^3$ (DLD-1) and $0.93 \pm 0.20 \text{ cm}^3$ (HT-29) and the mice had already lost about 10 % of their weight. Tumors and other selected organs were placed in a 24 well-plate and imaged using the Maestro™ imaging system with the automatic exposure function. Exemplary images are presented in Figure 19.

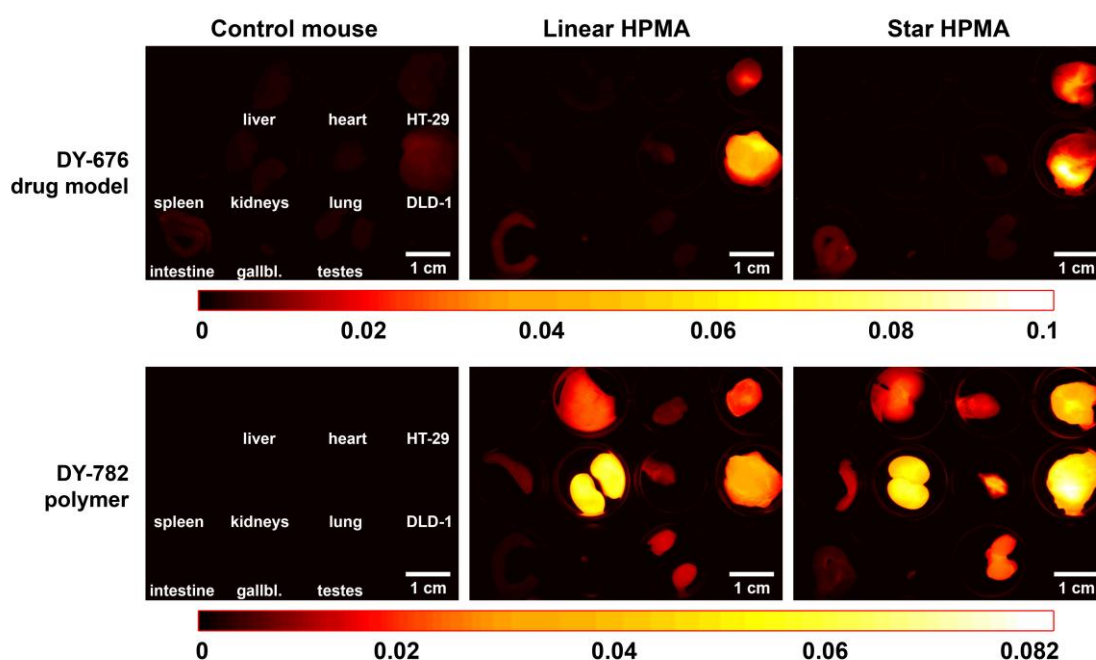


Figure 19. Excised organs of exemplary mice treated with the linear or star-like polymer two days after second polymer injection and excised organs from a non-treated control mouse. A drug model signal (DY-676) is observable only from the tumors.

The distribution of the polymer carrier fluorescence intensity in organs of tumor-bearing athymic nude mice was comparable to the distribution in organs of healthy mice (cp. Figure 7, p. 36). The fluorescence intensities were measured from the mouse organs of all mice and normalized with its area and exposure time. The drug model signal is almost exclusively detectable from both tumors whereas the polymer signal is also measurable in all other organs.

The results are in good agreement with the *in vivo* data and emphasize the high local accumulation of the drug model in the tumors. The relative distribution of the drug model

DY-676 is the same for both HPMA copolymers and thus independent on the polymer architecture. As it was already seen in the *in vivo* images, the highest drug model signal is detectable from the tumors, although the variability is rather high. The drug model is retained in the tumor tissue, whereas it is much more rapidly cleared from the blood and from other organs (Figure 20).

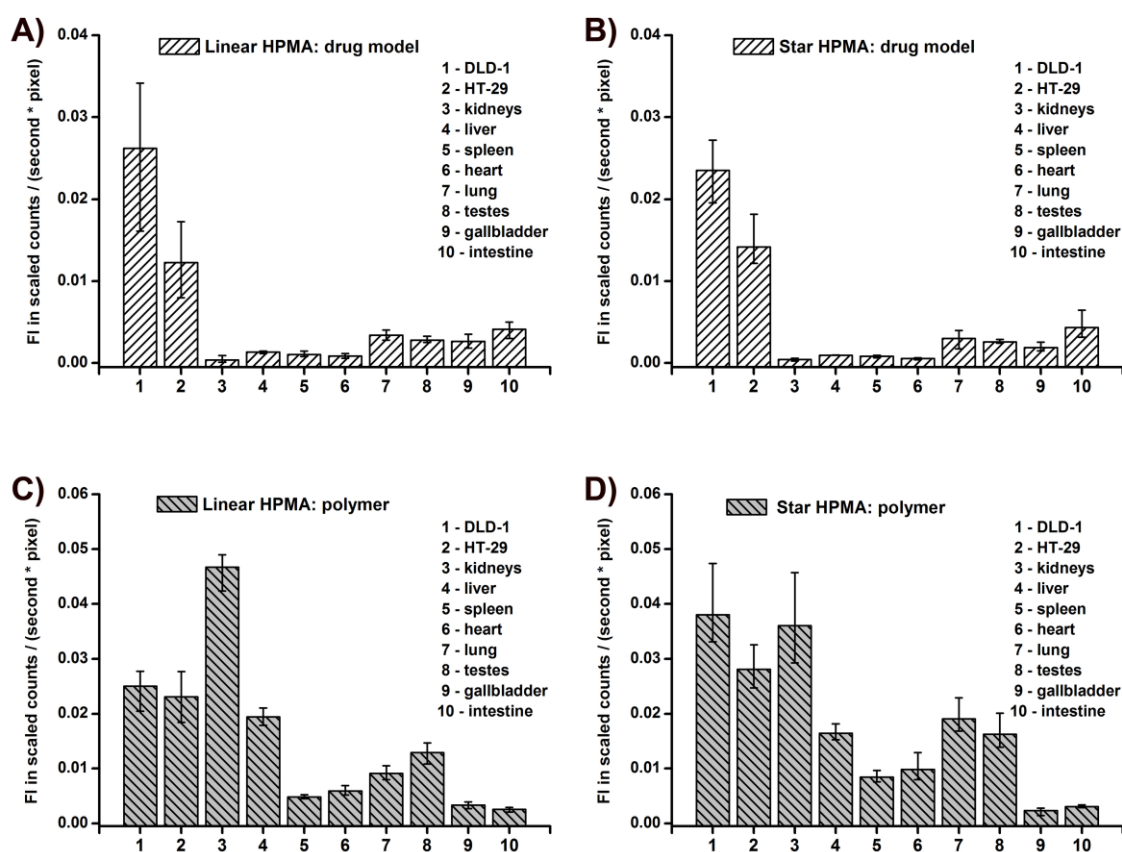


Figure 20. Distribution of drug model fluorescence signals (**A and B**) and HPMA copolymer fluorescence signals (**C and D**) in mouse organs two days after the second injection of 1.5 mg polymer. All data are means \pm minimum and maximum values.

The small remaining fluorescence can be ascribed to the organ autofluorescence. The non-cleavable polymer label was detectable in all mouse organs. Strongest fluorescence signals were measured from both tumors, the kidneys and also from the liver. The fluorescence intensity from the liver might be even underestimated, because of the high absorption from this organ. Although NIR light has optimum tissue penetration, the fluorescence might be repressed here. In comparison with other nano-scaled drug delivery systems, the accumulation of HPMA copolymers in liver and spleen can be considered as small. Most nanoparticles and nanocapsules are opsonized and removed

from the blood stream leading to a very strong accumulation in liver and spleen.^{220,221,224,235}

For a more detailed view, the tumors were sliced and imaged in higher magnification. Whereas the polymer carrier seemed to be quite homogeneously distributed in the tumors, the drug model showed notably increased fluorescence in specific parts of the tumors, especially in the central regions (Figure 21).

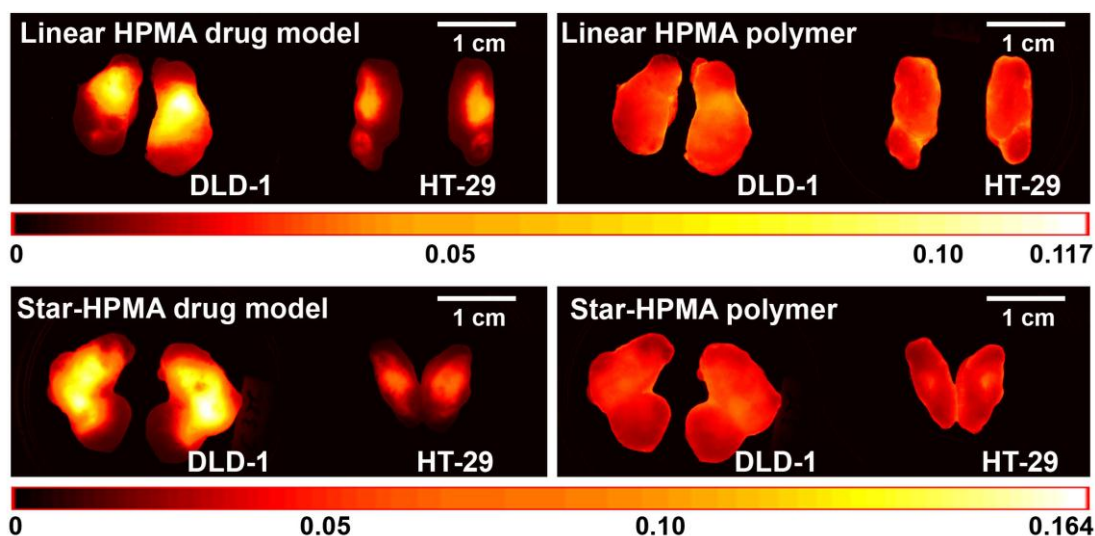


Figure 21. Drug model and HPMA copolymer distribution in axial tumor sections.

3.1.7.2 Confocal Laser Scanning Microscopy

Slices from the tumors were prepared by a razor blade (thickness app. 0.5 mm) and the drug model distribution was investigated by CLSM (Figure 22). The CLSM images were comparable for both tumor cell lines and both polymer groups. Diffuse fluorescent areas were observable next to non-fluorescent areas. It can be concluded that the composition of the tumor is not homogeneous, which influences the drug model distribution. However, no specific morphological structures could be detected, due to lacking brightfield overlay.

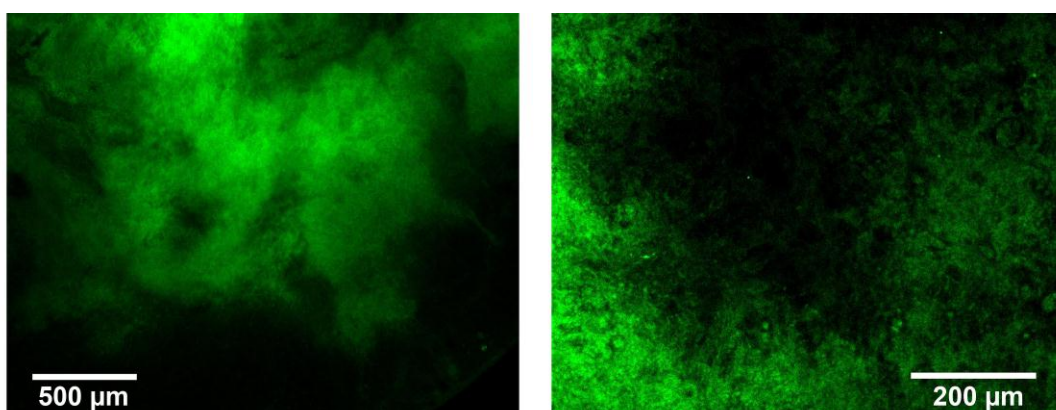


Figure 22. CLSM images of axial slices show fluorescent and non-fluorescent areas in the tumors (green pseudo-colored). **Left:** DLD-1 from linear HPMA group, **right:** HT-29 from star-HPMA group.

3.1.7.3 Histological Characterization

For a more detailed microscopic characterization, small pieces from tumors were extracted (app. 2 x 2 mm) from regions of the tumor showing either high or low drug model fluorescence. These slices and a complete axial section of each tumor were fixed in formaldehyde, embedded in paraffin, sliced (4 µm), dewaxed and stained with haematoxylin and eosin and subsequently observed by light microscopy, which allowed the observation of differentiated tumor structures. Vital, living tumor cells are intensively red colored in the microscope images, as structures in cytoplasm are stained with eosin. Necrotic and fibrotic domains without living cells are not particularly colored by the staining and present themselves much brighter. Inside living tumor cells large blue colored nuclei are visible. In some images also blood vessels with erythrocytes, mouse fibroblasts and connective tissue or muscle cells are detectable, which differ from tumor cells in shape, size and color.

Both tumors show necrotic fields of dead cells especially in their center, whereas living cells are more close to the border. Especially those slices from the tumors showing high drug model fluorescence (DY-676) had essentially more necrotic areas in the microscopic view than those having low fluorescence, which showed a much higher proportion of living tumor cells (Figure 23). A specific drug model accumulation in necrotic/fibrotic areas can be derived, which explains the non-homogeneous distribution of the cleavable drug model in the tumors. Particularly DLD-1 was characterized by widespread and frequent dead-cell areas in the center. These areas were smaller and less distinctive in HT-29, which can be explained with the increased growth rate of DLD-1 compared to HT-29 (cp. Figure 13, p. 42), leading to more insufficiently

vascularized areas. The different proportion of necrotic areas is likely an explanation of better drug model accumulation in DLD-1 than in HT-29 as well.

As an enhanced accumulation of the drug model in necrotic areas of the tumors is observed, it might be supposed that the local microenvironment (a lower pH than in normal tissues)^{59,227} in these areas increased the rate of drug model release. On the other hand, this effect could be ascribed to the insufficiently developed lymphatic system in these areas, leading to an inappropriate drug model clearance from these tissues.²³⁶ However, if a pharmacologically active cytotoxic agent was used instead of the drug model, it could diffuse into the tumor cells after it would have been cleaved from the polymer backbone and accumulated in these specific regions.

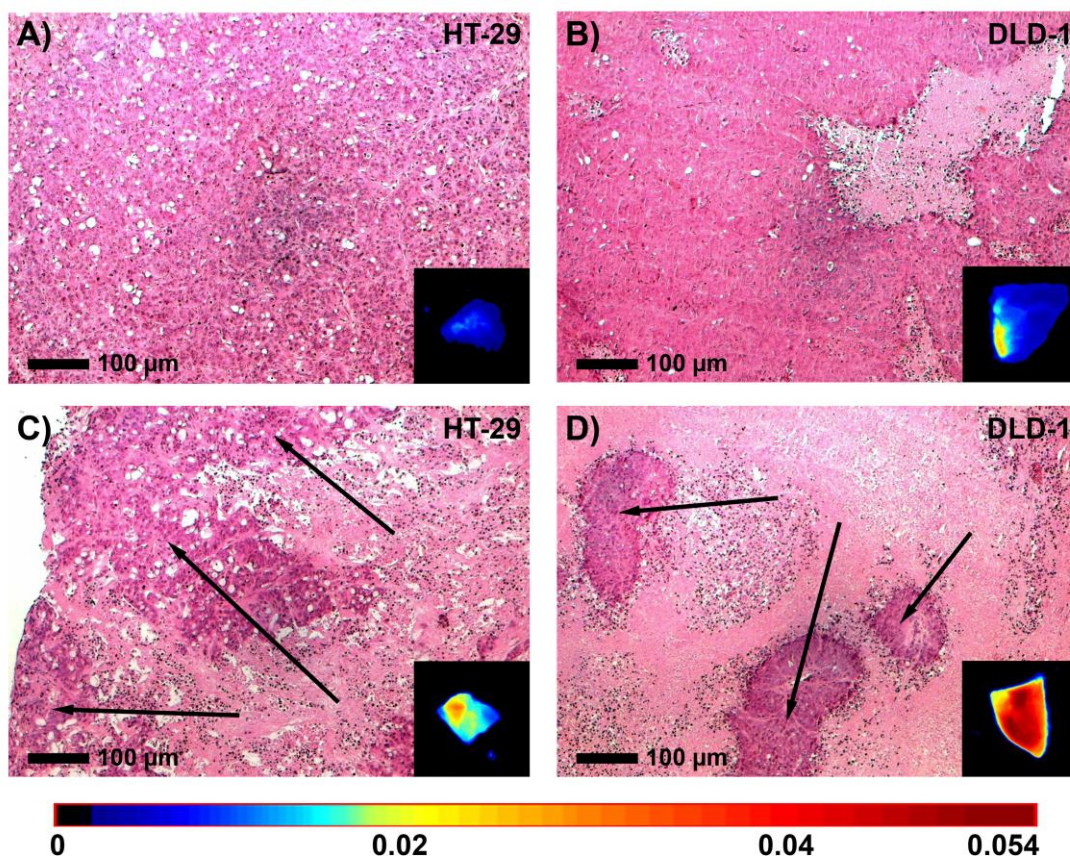


Figure 23. Microscopic sections of the tumors from a mouse that was treated with the linear HPMA copolymer (30 kDa). **A and B:** region of low drug model intensity. **C and D:** region of high drug model intensity (arrows point to regions of living tumor cells). The small images show the drug model fluorescence signal of the respective tumor region.

3.1.8 Summary

The distribution, elimination and tumor accumulation of HPMA copolymers conjugated with two fluorescent dyes was characterized in nude mice. In contrast to many previous studies, multispectral FLI enabled tracking the *in vivo* fate for several weeks and observing the distribution of the polymer and a conjugated drug model simultaneously. For that purpose HPMA copolymers differing in polymer architecture – linear and star-like – were successfully coupled with two fluorescent probes with different emission properties by cooperation partners. A difference in the relative qualitative biodistribution in the body between the 30 kDa linear and 200 kDa star-like polymers could not be detected. The star-like polymer circulated much longer compared to the smaller linear HPMA copolymer. Although the synthesized polymers were not biodegradable, even the 200 kDa star-like polymer was completely eliminated within 3 months. Comparable results have been observed already for 195 kDa poly (vinyl alcohol).²³⁷ A new calculation approach was developed to compare the accumulation of different polymers in tumors based on a reliable and reproducible method. The polymer carriers accumulated in the tumors as well as the cleavable drug model. The polymer accumulation was found to be quite slow. The time-dependent accumulation of the polymeric carrier emphasizes the importance of non-invasive long-term biodistribution and tumor accumulation studies. Moreover, the accumulation of drug model (cleavable dye) was smaller as it was already reported for doxorubicin in comparable HPMA copolymers.^{199,211,215} Most probably, this might be caused by the overlying fast rate of drug model release or additionally by a tumor cell line-dependent phenomenon. Low accumulation of HPMA copolymers was already reported for AT1 prostate cancer in rats,²¹⁶ whereas very high accumulation of HPMA copolymer delivered doxorubicin was found in EL4 T-cell lymphoma in mice.²¹¹ These varying findings suggest a high influence of the applied tumor models, which should be further investigated.

The *in vivo* data was confirmed by *ex vivo* imaging of the extracted organs. Histological characterizations demonstrated that the accumulation of the pH-sensitive releasable drug model is situated in local, necrotic areas of the tumors. It may be concluded from the data of the tumor accumulation experiments that not only the distribution of the polymer carrier plays a key role in delivery of the active drug to the tumors, but also the proper selection of the biodegradable spacer between polymer carrier and active drug. A much better accumulation of the drug model in the tumors is presumable when the release rate in blood is decreased.

3.2 HPMA Copolymers with Modified Release Rate^f

In addition to controlled delivery to tumors, specific local drug release from the polymer-drug conjugate is important for an effective tumor therapy. Several biodegradable spacers for tumor-specific drug release have been studied for this purpose.^{58,111,196,201} It is supposed that the release rate of the drug from the polymer strongly influences the amount of active drug delivered in the tumor.

This chapter enlightens the relationship between the structure of various pH-sensitive biodegradable spacers and the release rate of a fluorescent drug model conjugated to HPMA copolymers. The impact of the release rate on the tumor accumulation of both, the drug model and polymer carrier was investigated in tumor-bearing nude mice by non-invasive FLI. The already described polymer carrier structures were chosen: linear (~30 kDa) and star-like (~200 kDa) HPMA copolymers differing in molecular weight and architecture (cp. chapter 3.1, p. 27 ff.).

3.2.1 Synthesis of Dual-Fluorescent HPMA Copolymers with Modified Release Rate of a pH-Sensitive Drug model^g

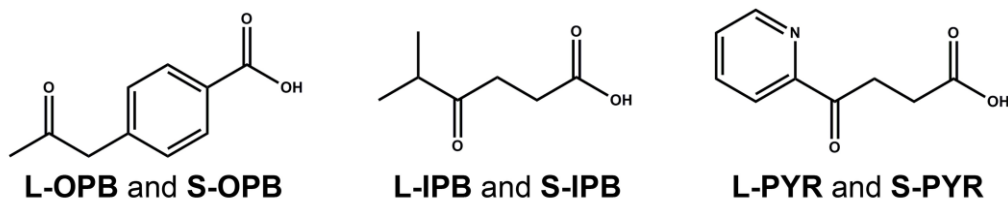
Polymers containing several spacers have been synthesized and characterized *in vitro* by the cooperation partners in Prague.²³⁸ A clear influence of the chemical environment of the hydrazone bond on the release rate in neutral and acidic (pH 5) buffer was found.²³⁸ The polymers containing the most promising spacers (IPB: 4-isopropyl-4-oxobutyric acid and PYR: 4-oxo-4-(2-pyridyl)butyric acid) were chosen to be investigated *in vivo* in tumor-bearing mice and to be compared with the previous results, which were obtained with polymers containing the drug model conjugated via the OPB-spacer (cp. chapter 3.1, p. 27 ff.). The main difference of the spacers is the variation in the structure close to the keto-group, which is necessary for the formation of the hydrolysable hydrazone bond (Scheme 5).

^f These results have been published:

Chytil P, Hoffmann S, Schindler L, Kostka L, Ulbrich K, Caysa H, Mueller T, Mäder K and Etrych T. Dual Fluorescent HPMA Copolymers for Passive Tumor Targeting with pH-Sensitive Drug Release II: Impact of Release Rate on Biodistribution. *J Controlled Release* 2013; 172(2): pp. 504-512.

^g Synthesis of polymers, all physicochemical characterizations and *in vitro* release: Institute of Macromolecular Chemistry AS CR, v.v.i., Heyrovský Sq. 2, 162 06 Prague 6, Czech Republic (T. Etrych, L. Schindler (née Vystrčilová) and P. Chytil)

In vitro release experiments showed a descending rate of drug model cleavage when the methyl-group in the OPB-spacer was replaced by an isopropyl-group (IPB) or by a pyridyl-group (PYR). The most stable hydrazone showing no release at pH 7 and slowest release at pH 5 in the *in vitro* experiments was prepared by use of the PYR-spacer.



Scheme 5. Structures of spacers used to form the pH-dependent cleavable hydrazone bond in linear (**L**) and star-like (**S**) HPMA copolymers.

The synthesis of the polymers followed the same principles for all spacers, leading to comparable dye contents and particle sizes of the polymers. It is in detail described in the literature.²³⁸

3.2.2 *In Vivo* Characterization in Tumor-Bearing Mice

Amongst the numerous synthesized polymers varying in the spacer structure between the polymer backbone and the drug model, those with the most interesting *in vitro* release profiles have been chosen to be characterized *in vivo* in tumor-bearing mice for comparison with the HPMA copolymers containing the OPB-spacer. The linear and star-like polymers containing the IPB-spacer (L-IPB and S-IPB) and the PYR-spacer (L-PYR and S-PYR) were investigated. A set of polymers containing DOX as a spacer between the polymer and the fluorescent drug model would have been very interesting to be investigated *in vivo*. Unfortunately, they were not applicable for biological evaluation using FLI because of the very poor fluorescence of the drug model. This poor fluorescence was probably a result of self-quenching of the two fluorophores because they were located close to each other (DY-676 and DOX). The fluorescence of DOX itself below 600 nm made it inappropriate for *in vivo* FLI because of insufficient light penetration.¹⁴⁴⁻¹⁴⁶

3.2.2.1 Biodistribution in Tumor-Bearing Mice

The four conjugates with modified drug model release rate were investigated in the same human colon carcinoma xenograft tumor models and basically following the same procedure as described already for the HPMA copolymers containing the OPB-spacer (cp. chapter 3.1.6, p 40 ff.). Analyzing the tumor accumulation, the size of the xenografts should have a relevant influence, as more necrotic/fibrotic areas are supposed to be found in larger tumors. Therefore, tumor size should be comparable, because the EPR-effect is more pronounced in later stages of tumor growth. The tumor sizes at the beginning of the experiment were comparable in all groups for DLD-1; HT-29 had a larger volume in the OPB-group (Table 6).

Table 6. Tumor sizes and mouse weights in each mouse group one day before polymer injection. The data represent the means \pm SD, $n=3$.

Spacer	Linear conjugates			Star-like conjugates		
	Volume of HT-29 (cm ³)	Volume of DLD-1 (cm ³)	Mouse weight (g)	Volume of HT-29 (cm ³)	Volume of DLD-1 (cm ³)	Mouse weight (g)
OPB	0.69 \pm 0.34	0.92 \pm 0.30	26.7 \pm 1.2	0.64 \pm 0.12	0.78 \pm 0.12	26.0 \pm 1.7
IPB	0.21 \pm 0.08	0.75 \pm 0.20	28.7 \pm 0.6	0.24 \pm 0.05	0.73 \pm 0.05	27.7 \pm 2.5
PYR	0.33 \pm 0.13	0.57 \pm 0.29	27.0 \pm 2.0	0.34 \pm 0.10	0.60 \pm 0.17	27.7 \pm 3.1

The biodistribution and elimination of the polymers were observable from the fluorescence signal of the non-releasable polymer label (DY-782). No significant difference in the polymer distribution between all 3 linear and all 3 star-like conjugates was observed. This result can be explained with the same precursors, which were used for the synthesis of the polymer conjugates. All linear polymers had the same size of about 30 kDa and all star-like polymers had the same size of about 200 kDa. The distribution and elimination of the linear and star-like polymers is presented in lateral fluorescent component images of the non-cleavable dye DY-782 from one exemplary mouse of each group (Figure 24). The images demonstrate a specific accumulation of all polymers in the tumors over the observation period of several days. An initial increase of the fluorescence intensity could be observed for all polymers with star architecture. This effect was already discussed previously (cp. chapter 3.1.3, p. 32 ff.) and is likely to occur due to quenching effects when the drug model is still bound to the polymer. As this effect is not observable for the linear polymers, it may be discussed that

the close arrangement of semitelechelic HPMA conjugated with the fluorescent dyes in the star-like architecture leads to fluorescence quenching. The elimination and distribution of the releasable drug model was dependent on the deployed spacer. An overview of the lateral fluorescent drug model component images from an exemplary mouse from each group is presented in Figure 25.

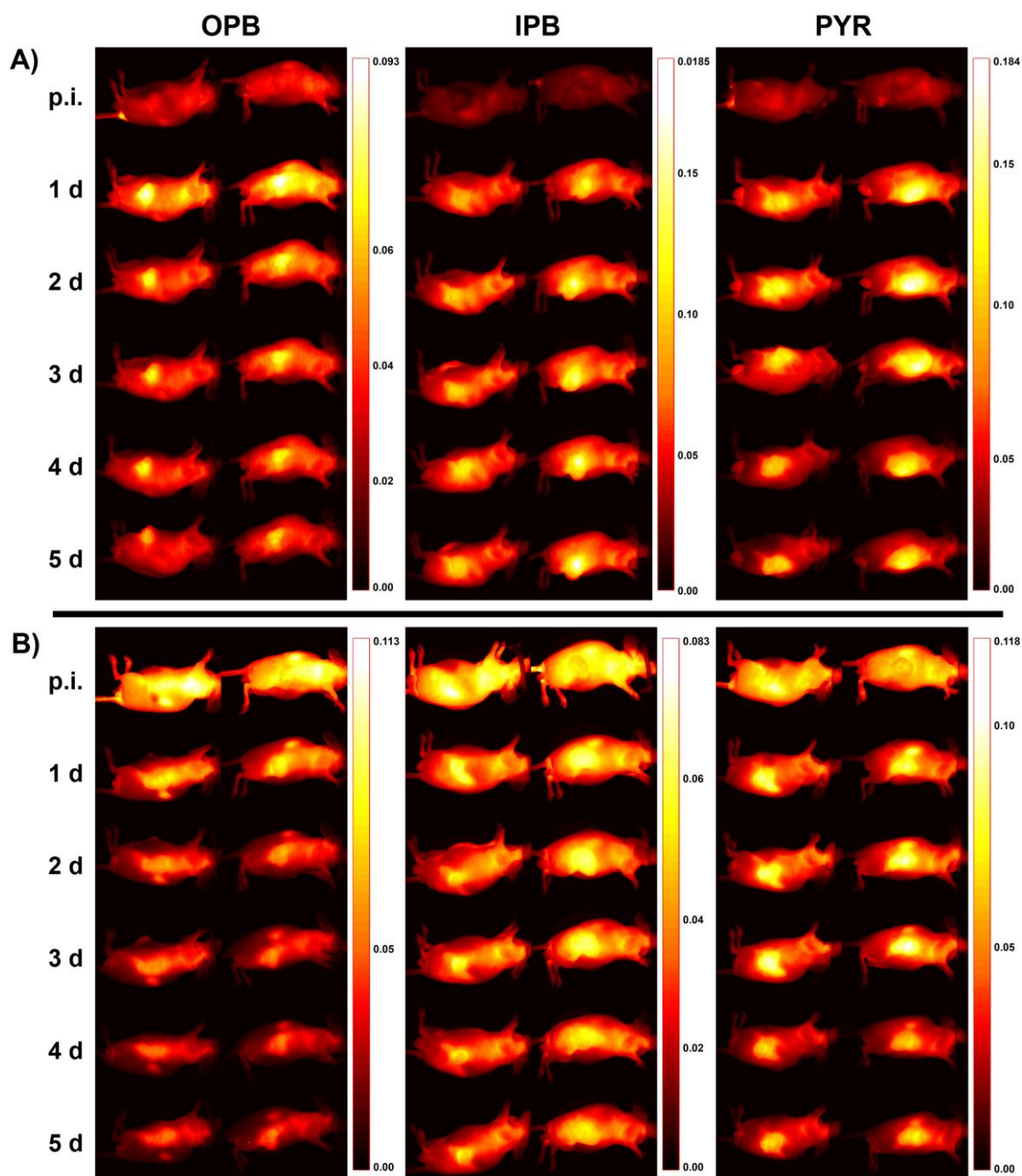


Figure 24. Polymer carrier distribution after injection of star-like (A) and linear polymers (B) containing different spacers (lateral images). A particular spacer-dependent difference in the biodistribution and elimination was not detected.

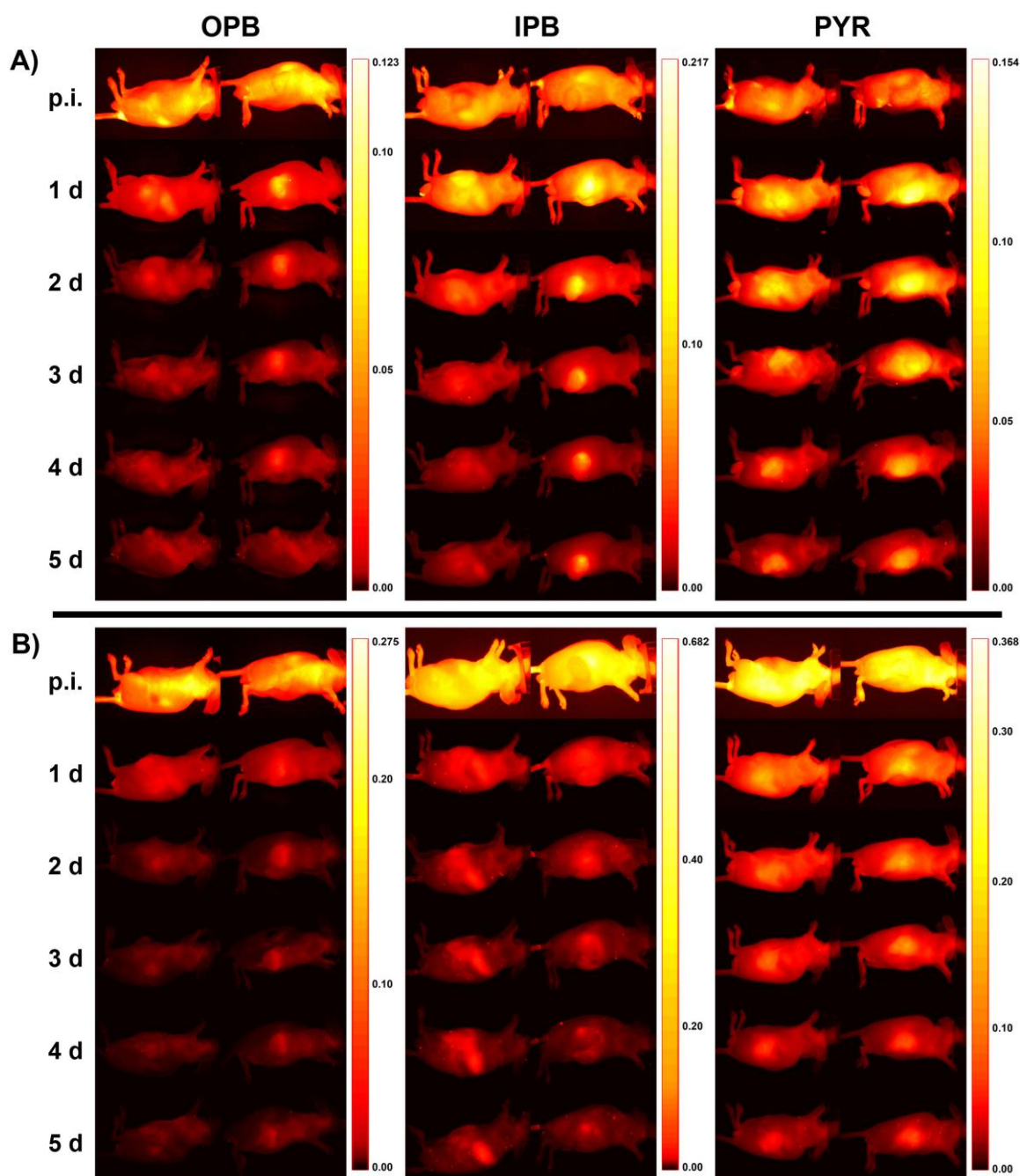


Figure 25. Drug model distribution after injection of star-like (A) and linear polymers (B) containing different spacers (lateral images). The elimination rate was found to be the highest for the OPB spacer and the lowest for the PYR spacer.

A low rate of drug model release (PYR spacer) led to longer circulation, while a rapid release (OPB) resulted in a short body circulation time of the drug model. The tumors showed the highest fluorescence intensity for the polymers containing the PYR spacer, indicating that the highest amount of drug model was transported to the tumor. Independently from the spacer-design the drug model seems to be eliminated much

faster from the body with linear polymers compared to star-like polymers (Figure 25). This effect may be explained by a significant elimination by the kidney of the relatively short linear polymers that contained a conjugated drug model as a result of the smaller polymer size (30 kDa) below the renal elimination threshold.^{219,239} Using the Maestro™ software, it was possible to measure the fluorescence intensities from the tumor area (Figure 26).

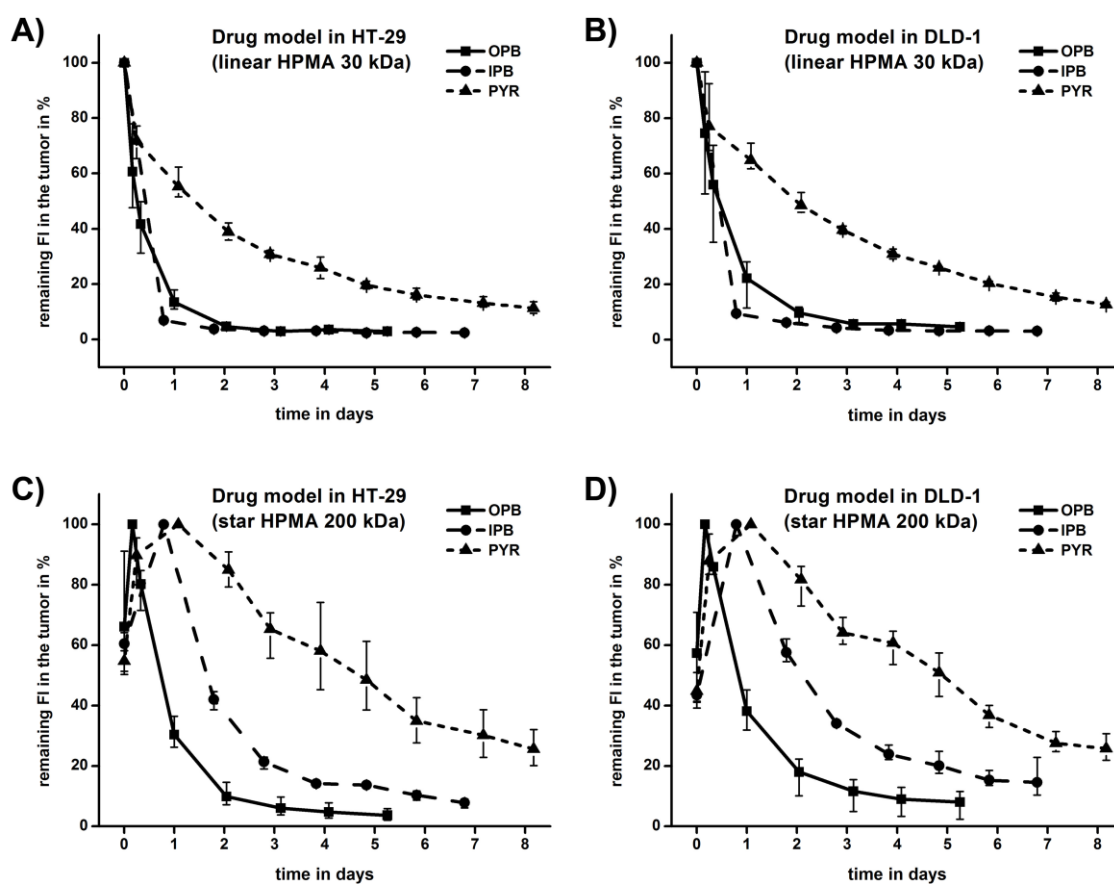


Figure 26. Relative fluorescence intensities of the drug model (DY-676) released from linear (A and B) or star-like (C and D) polymer architecture in both xenografts (normalized to tumor area). The data represent the means \pm minimum and maximum values.

The highest value is defined as 100 %. The fluorescence intensity decreased exponentially for all linear polymers in both tumors, while it increased initially for all star-like polymers (the initial fluorescence intensity is \sim 50 % lower than the highest measured intensity for IPB and PYR spacers after one day). This could be explained by a slower diffusion of the polymers into the small blood vessels of the skin or also by initial quenching effects, although these quenching effects were much less pronounced *in vitro* than the observed initial fluorescence increase *in vivo*. While linear polymers are

rapidly excreted by the kidney, star-shaped polymers circulate much longer; thus, there is more time for the extravasation and accumulation of the star polymer carriers in the tumor.

The uptake of star polymers in the solid tumor (based on the EPR effect) lasts for a longer period of time than that of the linear polymers, achieving maximum accumulation somewhere between 12 and 48 h.²¹¹ The data in Figure 26 show the significant dependence of the pharmacokinetic of the accumulated drug model on the hydrolytic stability of the polymer-drug model conjugate. A more stable spacer enabled prolonged circulation of the entire conjugate and thus led to higher accumulation of the drug model in the tumor. This finding was observed for both linear and star-like structures, but it was much more pronounced with the long-circulating high-molecular-weight star-like polymers.

3.2.2.2 Comparison of the Tumor Accumulation Value

For a better comparison of tumor accumulation, the TAV was calculated, which expresses the ratio of fluorescence intensity in the tumor to the fluorescence intensity in the area of the mouse body (cp. chapter 3.1.6.3, p. 44 ff.). A high TAV value represents good accumulation, whereas a TAV of 1 indicates the same concentration within the whole body. The TAV of the polymers (polymer label DY-782) was comparable for all of the investigated polymers (Figure 27) and increased with time regardless of the spacer and polymer architecture to values between two and three.

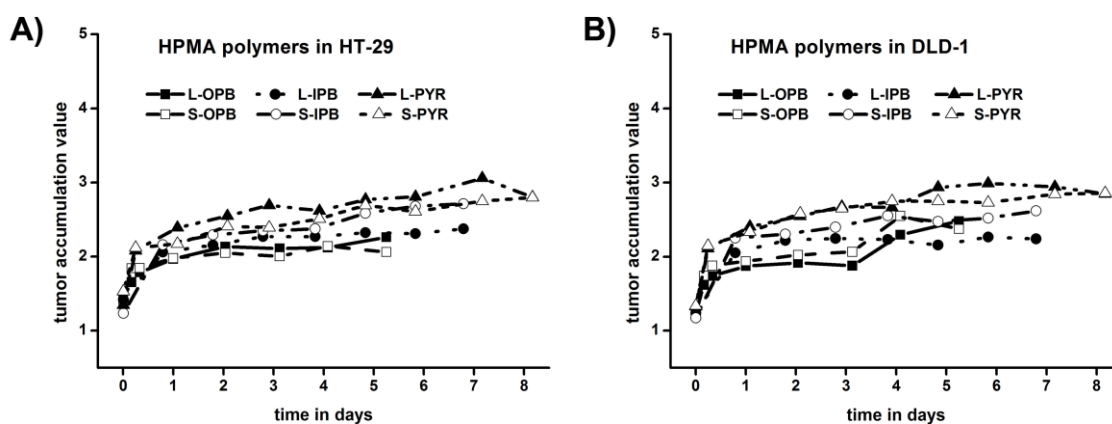


Figure 27. TAV of all polymers (non-releasable polymer label DY-782) in HT-29 (A) and DLD-1 (B). The data represent the means of $n=3$ per group. Error bars were omitted in these graphs for better perceptibility, but the variability was comparable in all groups.

Even only five minutes after injection the TAV is calculated to be slightly greater than 1, which is presumably not due to rapid tumor accumulation, but related to the more bright color of the tumor tissue compared to the mouse body. For both the linear and the star-like polymers, the relative tumor accumulation (tumor to body ratio) seemed to behave similarly. Slow drug model release is therefore important because the accumulation of the polymers in tumors is time dependent. Nevertheless, the total amount of DY-782 in the tumors was in all cases higher when using star-like polymers, which can be explained by the overall higher clearance of linear polymers (cp. Figure 24, p. 58). The TAV of the drug model was also independent of the polymer structure but did depend on the tumor model and spacer deployed (Figure 28).

Generally, a higher TAV was observed for DLD-1 compared to HT-29, most likely due to different tumor micro-environments (more acidic for DLD-1) or different tumor features like vascularization or the proportion of necrotic/fibrotic parts. This hypothesis was supported by the significantly increased number of necrotic areas, which were detected in the HE-stained histological slices of autopsied DLD-1 tumors compared to HT-29 tumors (cp. Figure 23, p. 53).

The highest TAV of the drug model in both tumor models was observed in conjugates with the OPB spacer. However, this did not directly translate to the greatest accumulation, as the TAV was high as a result of the negligible drug model levels in the blood stream (Figure 28 B). Obviously the TAV alone was not suitable for comparing the accumulation of the polymers containing different spacers, as it did not consider the absolute amount transported to the tumor (cp. Figure 26, p. 60). Similarly, the polymers containing the PYR spacer seem to be less effective when comparing the TAV values because of the high level of polymer-bound drug model still circulating in the blood, even after five days. However, a much higher level of drug model was also observed in the tumor, which can be ascribed to the time dependent polymer accumulation of polymers in the tumors still containing conjugated drug model.

From the comparison of polymers differing in the spacer structure used for the drug model conjugation to the polymer carrier it can be concluded that stabilization of the hydrazone bond with suitable substituents like the pyridyl-group (PYR) results in a prolonged blood circulation and thus an enhanced tumor uptake of the drug model. This effect will most probably result in a significant increase of antitumor activity in the case of real drug application instead of a fluorescent drug model. Consequently, the TAV as a

value for relative quantification of the tumor accumulation needs to be related to the absolute amount of drug model transported to the tumors.

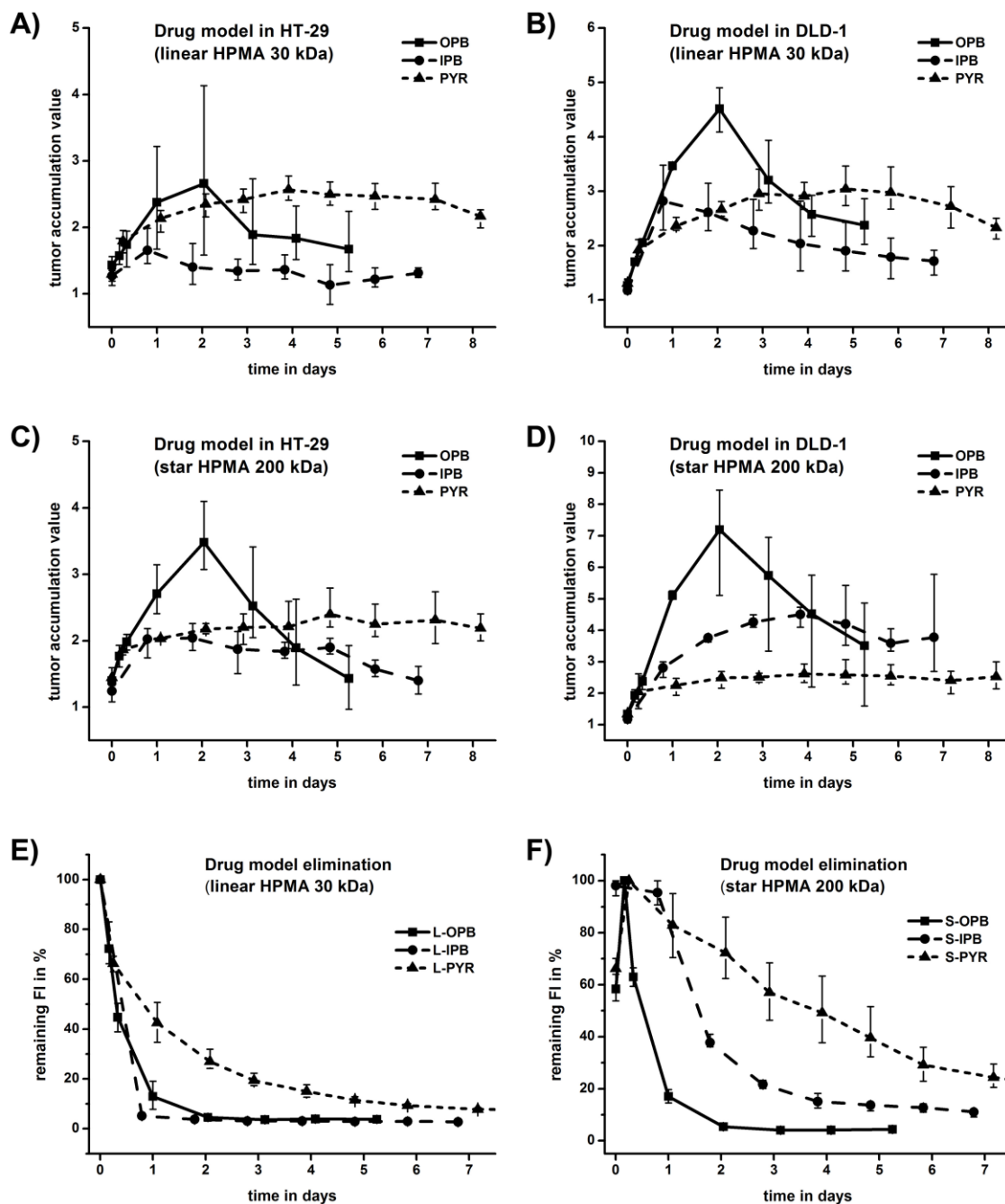


Figure 28. TAV (A-D) and total amounts (E and F) of the drug model from all investigated polymers. The data represent means \pm minimum and maximum values, $n=3$ (note different scaling of ordinates).

Despite the obvious advantage of a stabilized hydrazone bond, the application of polymer carriers with faster cleavable spacers could be improved by multiple dosing, exploiting the retention effect of the drug model. The fluorescence intensity of the drug model had strongly decreased in the OPB and IPB groups 5-7 days post injection. The mice of these groups were therefore re-injected with a second dose of 1.5 mg polymer, each. Consequently the TAV increased after the second injection (Figure 29). Interestingly, the inter-individual variability seemed to be smaller after the second injection. A markedly higher tumor accumulation value was observed 24 hours after the second injection, compared to one day after the first injection. This phenomenon can be explained by an exploited retention effect: as the drug model is retained in the tumor but rapidly removed from the blood when OPB or IPB were used as spacers, multiple dosing leads to increasing amounts of drug model in the tumors. Unfortunately the mice had to be sacrificed 1-2 days after the second injection due to the increasing tumor burden, and the findings could not be confirmed upon further dosing. Multiple dosing of the polymer conjugates must therefore be investigated in further studies using tumors with lower growth rates, which would allow longer experimentation periods.

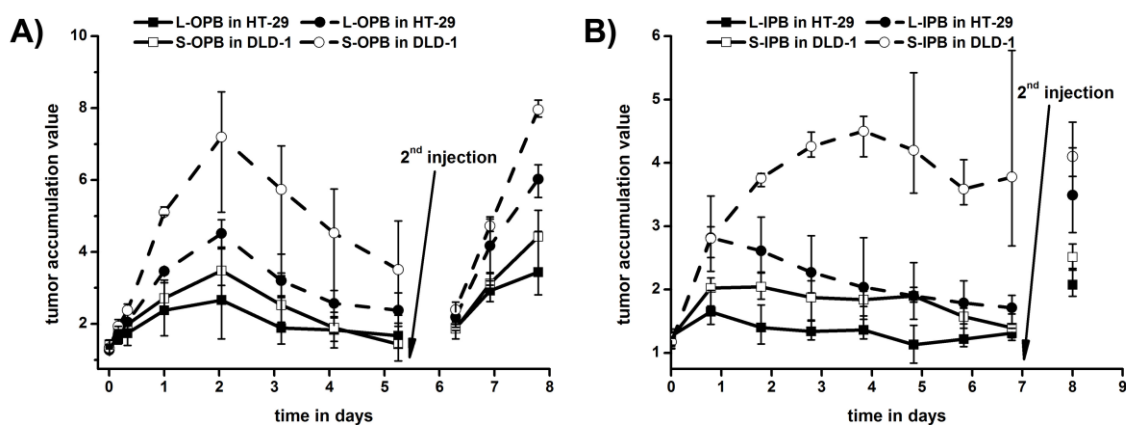


Figure 29. TAV of the drug model increases after the second injection for the HPMA copolymers with faster drug model release (A: OPB, B: IPB). The data represent the means \pm minimum and maximum values, $n=3$ (note different scaling of ordinates).

3.2.3 Ex Vivo Fluorescence Imaging of Autopsied Organs

After sacrifice, relevant organs and subcutaneous tumors were extracted from all mice of each group and fluorescence was analyzed *ex vivo*. Exemplary fluorescence images of the drug model distribution after the injection of star-like HPMA copolymers containing the IPB-spacer (1 day after injection of the second dose) and PYR-spacer (8 days after injection) are presented in Figure 30. The drug model fluorescence signal was highest in

the tumors of all groups, whereas the polymer label fluorescence was highest either in the tumors or the kidneys. The organ distribution of the polymers was basically the same as described already for the polymers with OPB-spacers (cp. chapter 3.1.7.1, p. 49 ff.). The presence of the polymer carrier in the kidneys has been previously discussed (cp. chapter 3.1.5, p 36 ff.).

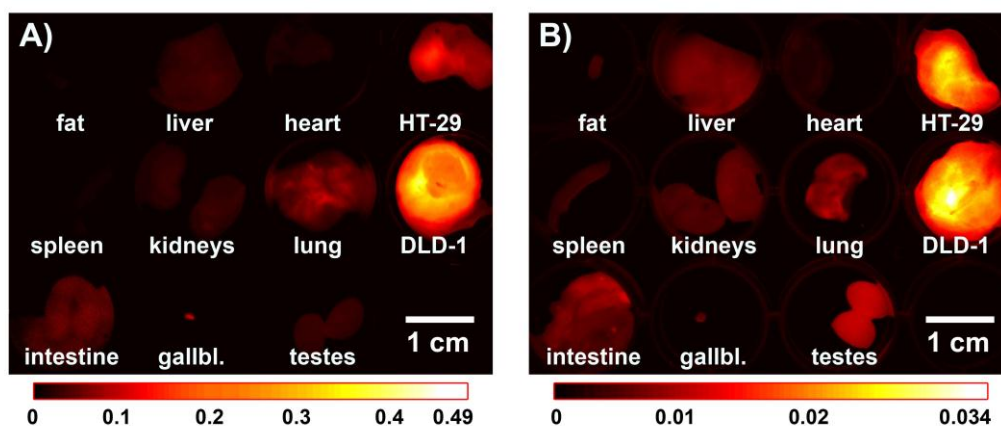


Figure 30. Exemplary drug model fluorescent component image (DY-676) of excised organs from a mouse treated with 1.5 mg S-IPB-HPMA (A: one day after 2nd injection) or with S-PYR-HPMA (B: eight days after injection). Note the overall lower intensity eight days p.i. (1st injection) compared to one day p.i. (2nd injection).

3.2.4 Summary

The dual fluorescently labeled HPMA copolymers described in chapter 3.1 were modified using different spacers to increase the stability of the pH-sensitive hydrazone bond. The influence of the two most promising spacers on the body fate of the HPMA carriers and the drug model was investigated in tumor-bearing mice and compared with the results of the HPMA copolymers containing the OPB-spacer, which was quite rapidly cleaved.

The results clearly demonstrate that the stability of the hydrolytically cleavable hydrazone bond *in vivo* strongly depends on its chemical environment. Conjugation of a pyridyl substituent (PYR) increased the hydrazone hydrolytic stability, which resulted *in vitro* in a decreased drug model release in buffers of pH 7.4 and 5.²³⁸ In particular, polymer conjugates containing the PYR spacer were very stable in blood, leading to a long circulation time for the drug model conjugate. A slow release of the drug model in the blood stream is an advantage because the polymer accumulation in the tumor is a slow process on a time scale over several days. The *in vivo* results demonstrated the clear correlation of a decreased drug model release rate and a higher amount of drug

model transported to the tumor, although this effect did not translate to an increased tumor accumulation value. However, tumor accumulation of the drug model could be as well increased by using conjugates with fast drug model release, by exploiting the retention effect by multiple dosing. As expected, the low clearance of the star-like polymer carriers from the body resulted in much higher accumulation in the tumors.

In conclusion, the results of the study emphasize the importance of the combination of a high-molecular-weight polymer carrier with a proper spacer. An optimum release rate is a prerequisite for the successful design of polymer conjugates for the treatment of solid tumors.

3.3 HPMA Copolymers: Therapy Study^h

Based on the promising tumor accumulation studies with HPMA copolymers, a therapy study was planned and carried out with the star-like HPMA copolymer (200 kDa) containing pH-dependent releasable doxorubicin. DLD-1 was chosen as tumor model because of its chemotherapy resistance to doxorubicin and because of the higher accumulation of HPMA copolymers in this model in the previous experiments. Chemotherapy resistance means that an inhibitory effect on the tumor cannot be achieved *in vitro* with a concentration of the cytostatic agent that corresponds to human peak plasma levels. Treatment with DOX-HPMA conjugates has been already shown to be effective in EL4-T-cell lymphoma previously, but not yet in doxorubicin-resistant colon carcinomas.^{239,240} To keep the number of animals manageable, this study was focused on the star-like architecture. A conjugate of doxorubicin with the star-like HPMA copolymer (200 kDa) was synthesized by the cooperation partners in Prague. *In vitro* release studies demonstrated comparable stability of doxorubicin-DY-676 and DY-676-PYR in pH 7.4 buffer and release in pH 5 buffer.²³⁸ This suggests a similar *in vivo* behavior of the therapy polymer and the dual fluorescent star-like HPMA containing the S-PYR spacer.

Within this therapy study, five groups were compared (cp. Table 3, p. 25): One group was conventionally treated with doxorubicin at a concentration of 5 mg/kg body weight, as the maximum tolerated dose (MTD) reported for doxorubicin in mice ranges from 5-10 mg/kg body weight.²⁴¹⁻²⁴⁴ Two groups were treated with HPMA-DOX conjugates, one with an equivalent dose and the other with a 3-fold increased dose. The remaining two groups served as control groups. A weekly dosing regimen was planned, but the treatment was halted for groups showing severe toxicities (e.g. weight loss, atypical behaviour, pronounced skin reactions). The results of the therapy study are presented in Figure 31. Both control groups showed exponential tumor growth and no weight loss. With respect to the rapidly increasing tumor size and tumor burden these mice were sacrificed 36 days after tumor inoculation.

^h Polymer synthesis: Institute of Macromolecular Chemistry AS CR, Prague, Czech Republic (T. Etrych, and P. Chytil). Study design: Stefan Hoffmann in cooperation with the Department of Internal Medicine IV, Oncology/Hematology, Martin-Luther-University Halle-Wittenberg (H. Caysa and T. Mueller). Study realization: Stefan Hoffmann, T. Mueller and A.-K. Heinrich (Institute of Pharmacy, Martin-Luther-University Halle-Wittenberg). Data Evaluation: Stefan Hoffmann.

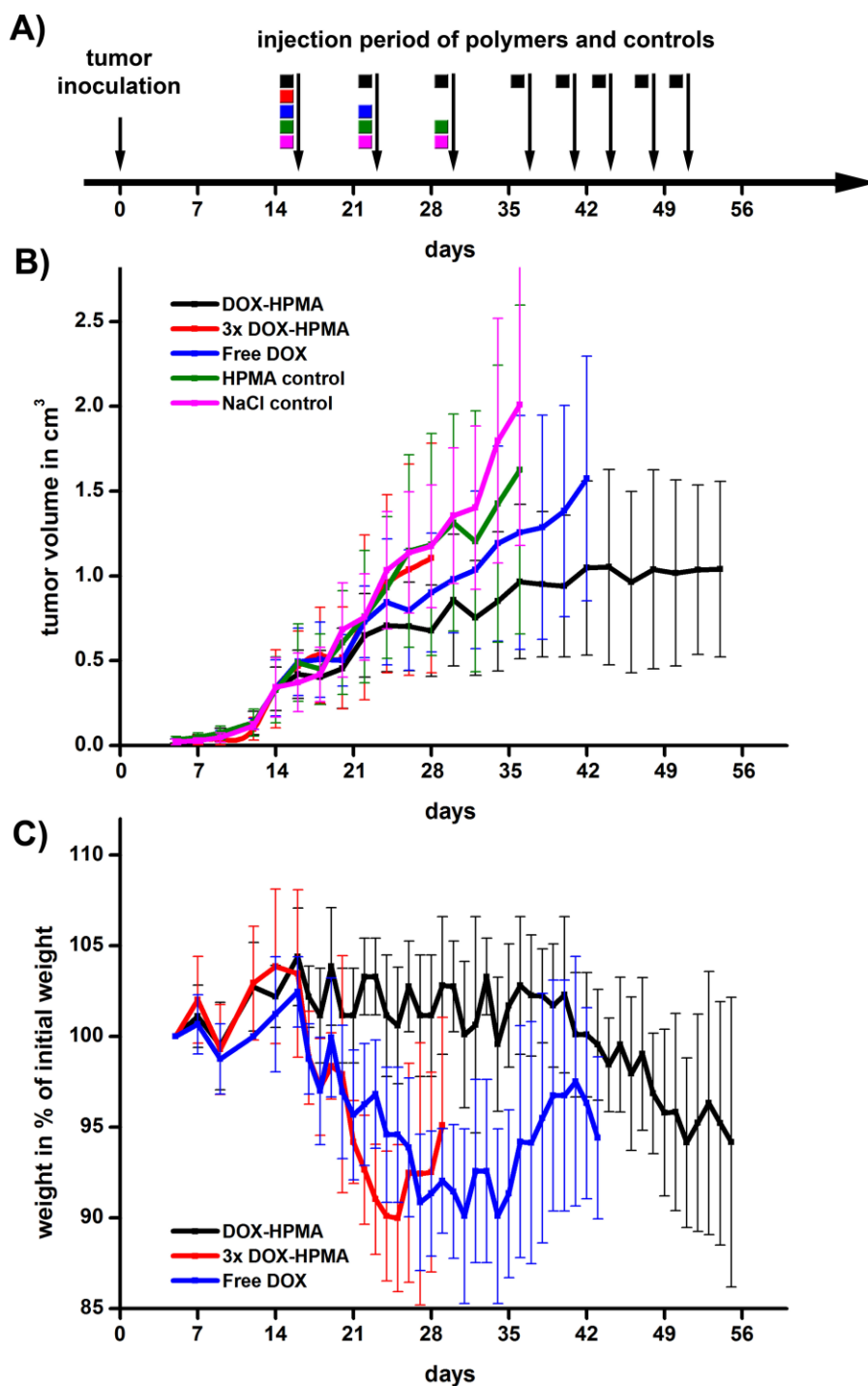


Figure 31. **A:** Injections during the therapy study. Tumors were inoculated at day 0. Therapy was administered once weekly taking toxicity into consideration. Only groups showing no severe toxicity or recovery from toxicity were re-treated in the next cycle. **B:** Tumor growth during treatment. Exponential growth can be observed for all groups but the DOX-HPMA group, which showed a stable mean tumor volume during the intensified therapy regimen (twice weekly) between day 40 and 55. **C:** Mouse weight was measured daily during therapy as one indicator for doxorubicin toxicity. The weight of the control groups did not decrease and is therefore omitted here. Interestingly the weight of the DOX-HPMA group did not decrease during weekly therapy, indicating low toxicity. All data represent means of six animals \pm SD.

The “3x DOX-HPMA”-group and the “Free-DOX”-group showed marked toxicity, which led to cessation of the weekly planned dosing regimen after only one or two injections, respectively. The pronounced toxicity in the group treated with free doxorubicin is remarkable, as higher MTDs were reported in literature.²⁴¹⁻²⁴⁴ Toxicity included atypical behavior, weight loss and doxorubicin-typical skin reactions and led to cessation of the experiment for the “3x DOX-HPMA”-group 13 days after one single injection only. The mice in the group treated with free DOX recovered within two weeks after the second injection, but due to cessation of the therapy an increasing tumor size was observed in this group, which led to the end of the experiment at day 44 without any further injection. Contrary to the “free DOX”-group, neither weight loss nor other signs of toxicity were observed in the group that was treated with the DOX-HPMA (equivalent doxorubicin dose) during the weekly dosing regimen. This effect can be explained by the lower amount of free doxorubicin circulating in the blood stream and the more local release of the active DOX in the tumor.

The overall good therapy tolerance in the DOX-HPMA group led to a change of the dosing regimen to twice weekly (accordingly 10 mg/kg per week), which subsequently resulted in weight loss of the mice, but also in a stable tumor size (mean) in the doxorubicin-resistant colon carcinoma xenograft tumor model (Figure 31). However the individual therapy response was varying (Table 7).

Table 7. Change of the tumor volume in cm³ of the mice treated with DOX-HPMA during 14 days of the weekly dosing regimen (from day 26 – day 40) and during the twice weekly dosing regimen (from day 40 – day 54).

Mouse	Day 26	Day 40	Day 54
1	0.63	0.98 (+56 %)	1.15 (+17 %)
2	0.79	1.01 (+28 %)	1.05 (+4 %)
3	0.55	0.65 (+18 %)	0.51 (-22 %)
4	0.35	0.40 (+14 %)	0.53 (+33 %)
5	0.76	0.95 (+25 %)	0.76 (-20 %)
6	1.13	1.64 (+45 %)	2.00 (+22 %)

The tumors in the DOX-HPMA group grew slower than in the control group, which was treated conventionally with doxorubicin. The tumor volume distribution in both groups was not comparable, likely because the sample size of 6 animals per group is small. Thus the non-parametric Mood’s median test was used to demonstrate a statistically

significant difference between the DOX-HPMA group and the “free DOX” group 42 days after tumor cell inoculation ($p=0.02$) Although the tumor volume distributions are not comparable between both groups and the interindividual variation is high, the Mood’s median test and the tumor volume trend during the experiment (presented in Figure 32) suggests a superior efficacy of the DOX-HPMA. However, this result needs further confirmation with an increased number of animals, which would allow more powerful statistical testing.

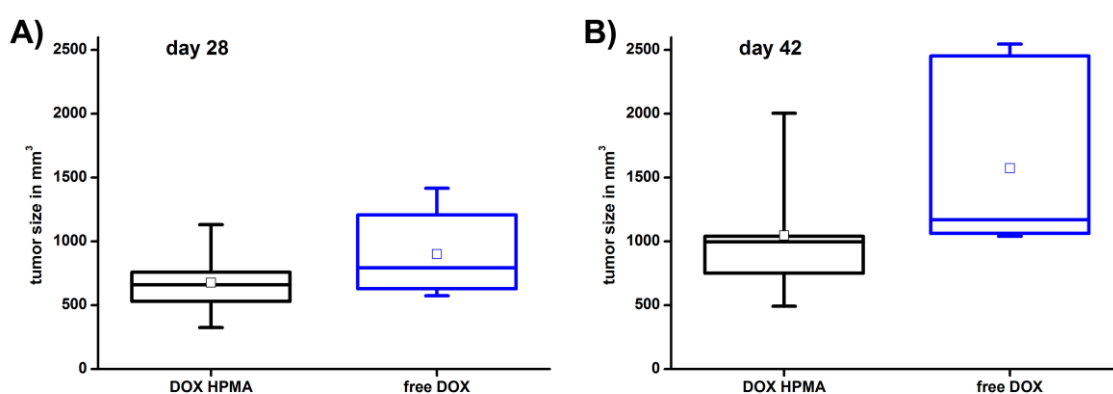


Figure 32. Tumor volume distribution within the DOX-HPMA group and the “free DOX” group 28 days (A) or 42 days (B) after tumor inoculation, respectively. A superior effect of the DOX-HPMA can be expected from the tumor volume trend. Boxes represent median, 1st and 3rd quartile; whiskers represent minimum and maximum; squares represent the mean.

The results of the therapy study demonstrate an additional therapeutic effect of the DOX-HPMA copolymers. Compared to the same dose of free DOX, a reduced toxicity was observed and thus a higher dose could be administered. Considering the aggressive and fast growing doxorubicin-resistant tumor model, the results are likely to be even more impressive when sensitive tumor models or tumors with slower growth rate are used, which should be addressed in further experiments.

3.4 Carbohydrate Plasma Volume Expandersⁱ

Carbohydrates present to be a class of wide-spread polymers, which are pharmaceutically used for various purposes and in several dosage forms. Amongst many other applications, polymers from this class are used as additives in solid dosage forms like tablets and pellets, as gelling agents, and also as plasma volume expanders (PVE) for many years.^{245,246} Recently, carbohydrates have also been considered as building blocks for nanoparticles.²⁴⁷ In addition, carbohydrate drug conjugates of lower molecular weight have already been investigated.²⁴⁸ Hyaluronic acid (HA) has been intensively investigated as a high molecular weight carbohydrate for tumor therapy and some products have already entered clinical studies.²⁴⁹ HA-Irinotecan from Alchemia Ltd. (Australia) presents to be a promising candidate and is currently investigated in clinical trials (phase III).

However, carbohydrate plasma expanders have not been considered for passive tumor targeting yet. In drug delivery, polysaccharide plasma expanders could be an interesting alternative to synthetic polymers and other carriers. Potential advantages include low cost synthesis, constant availability, a good safety profile, biodegradability and the long clinical use as plasma expanders. PVEs based on glucose monomers, like hydroxyethyl starch (HES) and dextran (DEX), are known to be well tolerated and biocompatible. High doses of these materials have been used in the clinic for decades.^{250,251} Currently there are several approved products commercially available, for instance HyperHES[®] (Fresenius Kabi), Venofundin[®] (B. Braun) and Vitafusal[®] (Serumwerk Bernburg). The production of these polymers is well established and possible in large scales under GMP conditions. Furthermore, HES is presently used to develop new drug delivery systems for parenteral application, for gene delivery, and it also attracted attention as commercial technology (HESylation[®]) to improve the solubility and to prolong the circulation time of certain active compounds.²⁵²⁻²⁵⁵ Recently, safety issues have been raised concerning the use of high-molecular-weight hydroxyethyl starches in certain severe diseased patients.²⁵⁶⁻²⁵⁸ However the difference in using HES as plasma volume expander (infusion of comparatively large volumes) or in tumor therapy needs to be taken into account. Three different high-molecular-weight carbohydrate PVEs have been

ⁱ These results have been published:

Hoffmann S, Caysa H, Kuntsche J, Kreideweiß P, Leimert A, Mueller T and Mäder K. Carbohydrate Plasma Expanders for Passive Tumor Targeting: In Vitro and In Vivo Studies. Carbohydr Polym 2013; 95(1): pp. 404-413.

investigated: Hydroxyethyl starches of 200 kDa (DS 0.5) and 450 kDa (DS 0.7) and Dextran 500 kDa (HES 200, HES 450 and DEX 500).

3.4.1 *In Vitro* Cytotoxicity and Immunogenicity

As the polymers used in this study have been used in the clinic in high doses as plasma volume expanders, they can generally be considered as biocompatible and safe. To support this, cytotoxicity was assessed by MTT-assay in human hepatocellular carcinoma cells (HepG2) and the activation of important pro- and anti-inflammatory cytokines in human peripheral blood mononuclear cells (PBMCs) was measured.

3.4.1.1 Cytotoxicity in Hepatocellular Carcinoma Cells (HepG2)^j

Cell viability was investigated by the MTT-assay in HepG2 cells after incubation with polymer solutions of 2 mg/mL or 20 mg/mL for 24 h or 48 h, respectively (Figure 33, n=16 each). Both concentrations are considerably higher than the initial blood concentration in mice in the following *in vivo* experiments (~ 0.8 – 1.4 mg/mL; cp. chapter 3.4.4, p. 79).

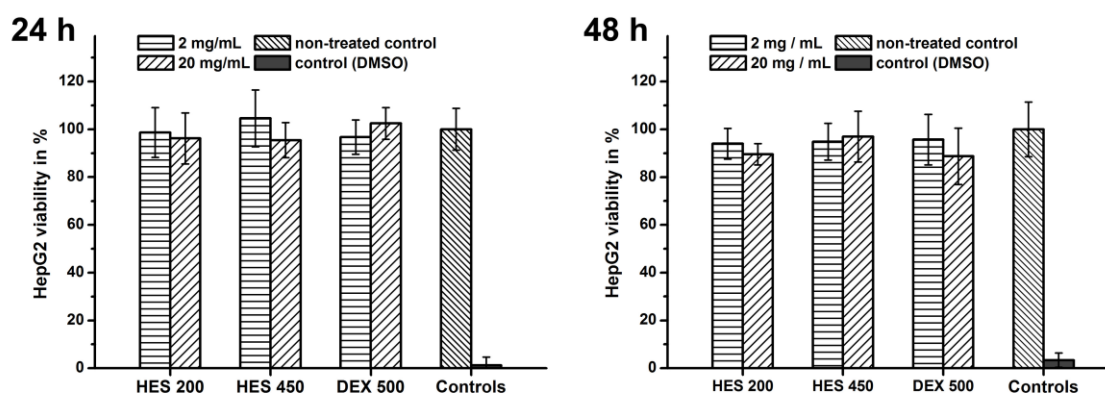


Figure 33. Cell viability of human hepatocellular carcinoma cells (HepG2) after incubation with PVE polymer solutions after 24 h or 48 h, respectively. Data represent means \pm SD, n=16.

^j Patrick Kreideweiß of the Institute of Pharmacy, Biochemical Pharmacy, Martin-Luther-University Halle-Wittenberg is acknowledged for experimental realization.

Hepatocytes are a relevant model to look for cytotoxicity. Dose dependent liver deposition and histological alterations in the liver after repeated infusion of hydroxyethyl starches have been already reported.^{259,260} The viability of non-treated cells served as a negative control and was defined to be 100 %. Cells treated with dimethyl sulfoxide (DMSO) served as a positive control. No significant decrease of HepG2 cell viability was observed after the incubation for 24 and 48 hours, leading to the conclusion that the carbohydrate polymers used in this study do not show any non-specific cytotoxicity against HepG2 cells.

3.4.1.2 Immunogenicity: Cytokine Modulation Assay^k

Lipopolysaccharides from various sources are known to be strong inducers of cytokine production. Therefore, all polysaccharide derived polymers for parenteral use should be tested for modulation of relevant cytokines, which are mainly produced by PBMCs after parenteral application of cytokine inducers. The plasma expanders used in this study were investigated for modulation of the production of six relevant pro- and anti-inflammatory cytokines (IL-1 β , IL-6, IL-8, IL-10, IL-12p70 and TNF) in human PBMCs after incubation for 4 h or 24 h. The cytokines were measured in cell culture supernatants by cytometric bead array flow cytometry (Figure 34).

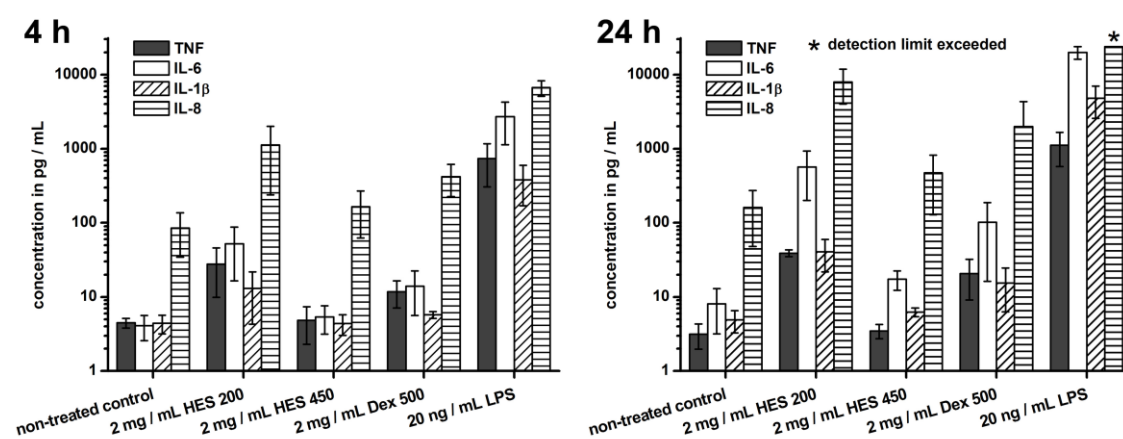


Figure 34. Cytokine concentration measured in cell supernatants of human PBMCs after incubation with PVE polymer solutions after 4 h or 24 h, respectively. Data represent means \pm SD, $n=3$.

^k Anja Leimert of the Department of Anesthesiology and Critical Care Medicine, Martin-Luther-University Halle-Wittenberg is acknowledged for experimental assistance.

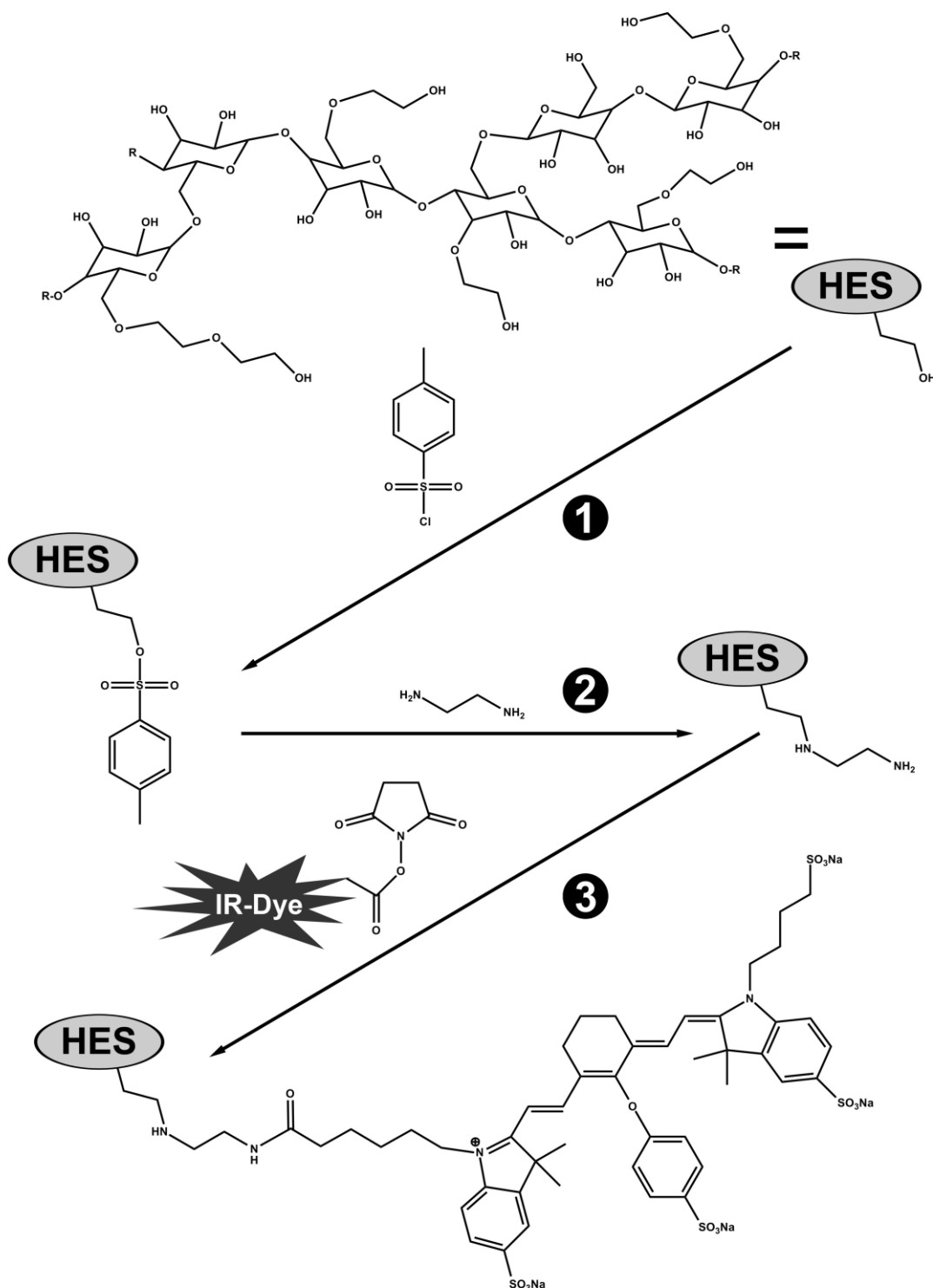
The positive control (20 ng/mL LPS) showed a tremendous increase of the pro-inflammatory cytokines (IL-1 β , IL-6, IL-8, and TNF), whereas the concentration in the samples treated with HES 450 (2 mg/mL) was comparable to the non-treated control. The cell supernatants treated with HES 200 and DEX 500 showed a slightly increased cytokine concentration compared to the non-treated control, especially for IL-8, which is an activator of neutrophils and mediator of angiogenesis, but also binds to erythrocytes.^{261,262} However, the concentration of IL-8 in cell supernatants from the LPS treated control was much higher and exceeded the upper detection limit of 23,000 pg/mL. IL-8 was also produced in the negative control (160 pg/mL \pm 113 pg/mL). In consistency with numerous studies investigating the immunogenicity of hydroxyethyl starches, the polymers used in this study can be regarded as non-immunogenic.²⁶³⁻²⁶⁶

3.4.2 Synthesis of NIR-Fluorescent Polymer-Dye Conjugates

All three polymers were conjugated with a fluorescence dye as a preparatory step for the *in vivo* studies by FLI (cp. chapter 2.2.1.2, p. 13). An NIR fluorescent probe was chosen for conjugation because of good light penetration in the “optical window”, which provides information also from deep tissues.^{145,146} To form a stable and physiologically non-cleavable amide bond the polymers were amine-modified prior to dye conjugation.²⁶⁷ The principle reactions are presented in Scheme 6.

HES 200 and HES 450 were activated with p-toluenesulfonyl chloride, using a modified method based on a previously described protocol.¹⁶⁷ Dextran was activated with p-toluenesulfonyl chloride in water, as the activation in DMF did not work for DEX 500 because of insufficient solubility. Toluene sulfonyl chloride activation of alcohols in water has already been previously reported.¹⁶⁸ Success of the reactions was monitored by ¹H-NMR in D₂O after purification by dialysis and lyophilization (Figure 35 A). The substitution degree (DS) with toluenesulfonyl esters was determined to be about 2 % per anhydrous glucose unit (AGU) for all polymers by calculation of the peak ratio of the aromatic protons (δ =7.4 and δ =7.75) to the proton at the alpha-carbon atom (C1, δ =5-6) of the AGU.²⁶⁸

$$DS [\%] = \frac{\text{area (7.4 ppm)} + \text{area (7.75 ppm)}}{4 \text{ protons} * \text{area (C1-proton peaks)}}$$



Scheme 6. Modification of HES. **1:** activation, **2:** amine modification, **3:** dye conjugation.

In the following step, the activated polymer was exposed to 500-fold molar excess of ethylenediamine in a mixture of borax buffer/DMF (pH 9.5) to prevent cross-linking reactions. Reaction success was proven by the disappearance of the signal of aromatic

protons in the $^1\text{H-NMR}$ spectra after sample purification. The succinimidyl activated fluorescence dye IRDye[®] 800CW-NHS ester was conjugated to the amine-modified polymers in bi-distilled water via an amide bond. The intermediate products and the final polymer-dye conjugates were purified by dialysis against bi-distilled water for 72 hours after each reaction step using a 3.5 kDa membrane. Although the molecular weight of IRDye[®] 800CW of 1.2 kDa (cp. Scheme 2, p. 12) is below the membrane threshold, the dialysis rate through the membrane was found to be very small in control experiments. Thus, after the last purification step, a proportion of free dye is still contained in the polymer.

The proportion of free dye was determined to be 6 % for HES 200 and HES 450 and 10.7 % for DEX 500 by analytical ultracentrifugation at 40.000 rpm and 20 °C (dye absorbance measured in an absorption maximum at 380 nm).¹ The poor permeability of the membrane for IRDye[®] 800CW was unexpected and did not occur for any of the other fluorescent dyes used in this thesis (cp. Scheme 2, p. 12). It might be explained with a hydrate shell or maybe dimer formation of the free dye. This effect was not further investigated as it was observed retrospectively, but however, it demonstrates the importance that one ought to be aware of appropriate controls when dialysis is performed as a product purification step. The amount of dye conjugated to the polymers was determined by fluorescence imaging (Figure 35 B).

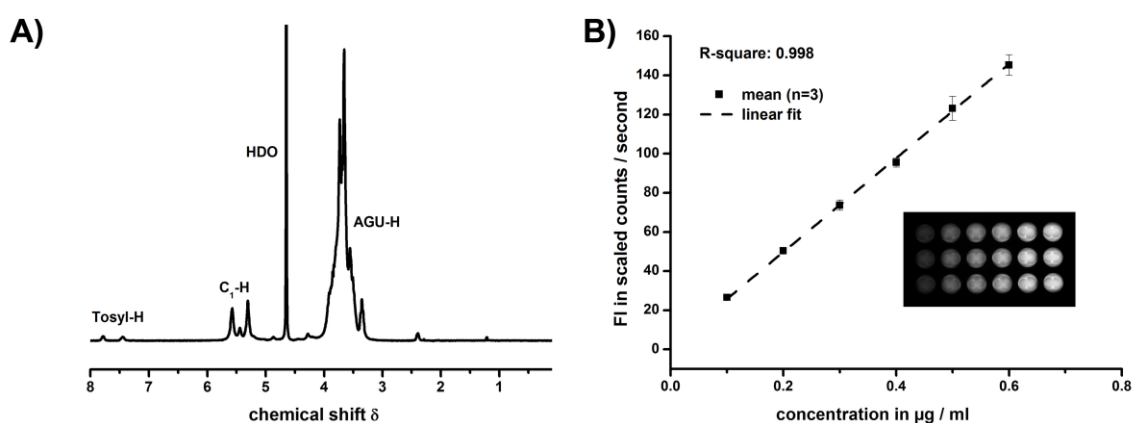


Figure 35. A: $^1\text{H-NMR}$ spectra of toluenesulfonyl-activated HES 450. **B:** A linear calibration curve of the fluorescence signal from pure dye concentrations was used to determine the conjugation efficiency.

¹ Hauke Lilie of the Institute for Biochemistry and Biotechnology/Technical Biochemistry, Martin-Luther-University Halle-Wittenberg is acknowledged for performing the analytical ultracentrifugation and for data analysis.

The conjugation efficiencies were determined to be 90 % (HES 200), 80 % (HES 450) and 75 % (DEX 500). Besides the amine modification with ethylenediamine, HES 200 was also modified using 1,8-octyl diamine and non-modified dextran 500 was also conjugated with the NIR-dye via an ester bond to serve as an ester control in the following *in vivo* experiments.

3.4.3 Particle Size and Molecular Weight Distribution

The particle size and molecular weight distribution were characterized for the three ethylenediamine modified polymers before and after modification. DLS measurements from unmodified polymers indicated a broad distribution of particle sizes (Table 8). The broad molecular weight distribution results were confirmed by AF4 measurements (M_W/M_N between 3.6 and 4.4, $n=3$). The results are summarized in Table 9. They indicate the presence of a fraction with lower molecular weight in all polymers (Figure 36).

Table 8. Particle size and polydispersity of the carbohydrates obtained from DLS. D_z : z-average mean square diameter, PDI: polydispersity index, $n=4$.

Polymer:	HES 200 / 0.5	HES 450 / 0.7	Dextran 500
D_z	18 nm \pm 0.2 nm	24 nm \pm 0.4 nm	33 nm \pm 0.5 nm
PDI	0.24 \pm 0.01	0.29 \pm 0.03	0.41 \pm 0.02

Table 9. AF4 results of the polysaccharide-based polymers. D_z : z-average mean square diameter; M_W : weight-average molar mass; M_N : number-average molar mass; M_W/M_N : polydispersity value.

Polymer	Non-modified polymers AF4 results			Amine-modified polymers AF4 results			IRDye [®] 800CW content (% m/m)
	D_z (nm)	M_W (kDa)	M_W/M_N	D_z (nm)	M_W (kDa)	M_W/M_N	
HES 200	26 \pm 2	230 \pm 5	3.6	33.6 \pm 5	128 \pm 7	2.0	0.55
HES 450	36 \pm 1	383 \pm 18	4.4	49.1 \pm 5	623 \pm 3	4.8	0.43
DEX 500	50 \pm 5	486 \pm 38	3.6	75.5 \pm 17	104 \pm 10	2.0	0.37

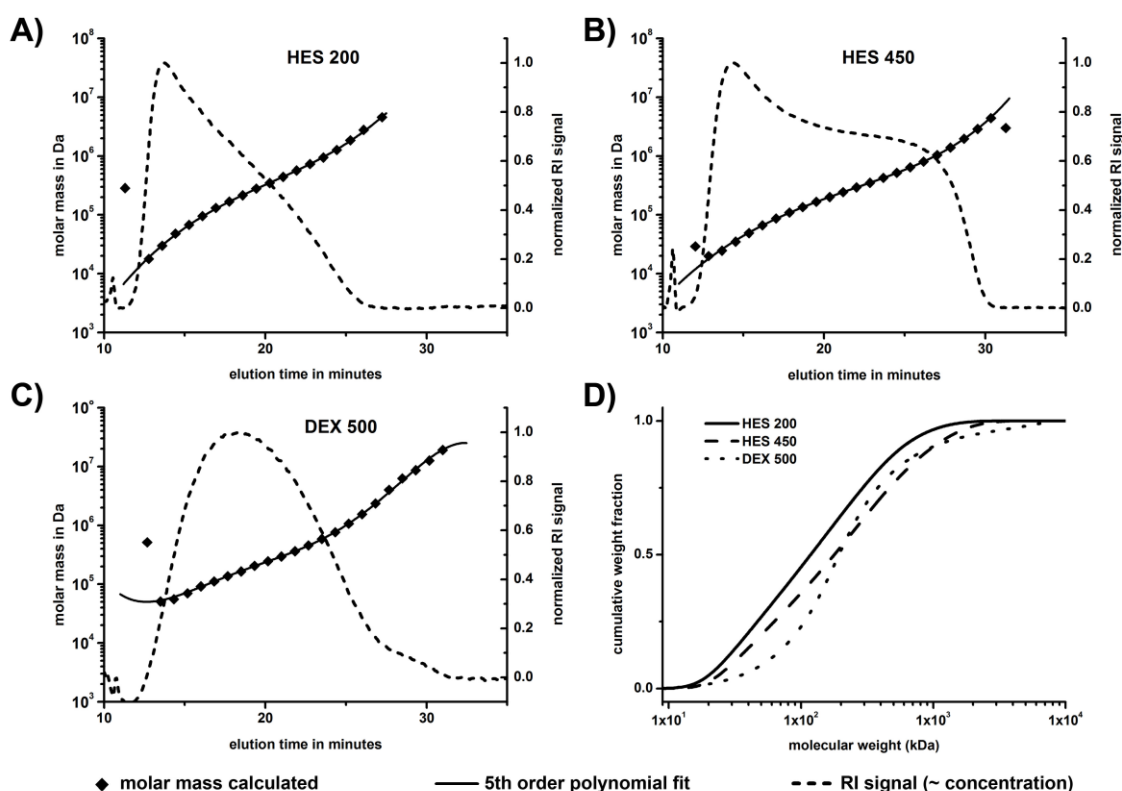


Figure 36. Elution profile of HES 200 (A), HES 450 (B) and DEX 500 (C). The RI signal corresponds with polymer concentration. All polymers showed a broad molecular weight distribution D: Cumulative molecular weight distribution of non-modified HES 200, HES 450 and DEX 500.

Recently, asymmetric flow field-flow fractionation has been already used to characterize the molecular weight distribution of HES.^{179,268} AF4 has the advantage that the polymers are separated according to their size before they are detected in the light scattering detector. Therefore monomodal size distributions are measured at each point in time during sample elution, given that different molecules in one sample are separated due to different flow properties. This results in more precise particle size distribution results. By combining the angle dependent light scattering signal with the sample concentration, which is obtained from the RI signal, the molecular weight can be calculated.²⁶⁹ The incremental change of the refractive index (dn/dc), which is needed for correct calculation, was determined beforehand by injection of different polymer concentrations in the range of 0.2 mg/mL to 1 mg/mL to the RI detector. It was calculated to be 0.142 mL/g (HES 200), 0.146 mL/g (HES 450) and 0.145 mL/g (DEX 500), which is in very good agreement with literature data.²⁷⁰ Generally, the z-average diameters measured by dynamic light scattering ($n=4$) were smaller than those determined by AF4, but the trend

that non-modified polymers with higher molecular weight have also a larger particle size was comparable for all polymers.

The AF4 results show the influence of the syntheses on the molecular weight distribution of the polymers. Competing processes can be discussed as reason: First, degradation reactions are likely to occur during the amine-modification (pH~10). Especially DEX 500, which was reacted at 70 °C, showed a strong decrease of the molecular weight after this step. Secondly, the polymers can self-aggregate during the reaction which could explain the increased molecular weight of HES 450. Furthermore, using ethylenediamine, cross-linking of molecules might occur, although 500 fold molar excess was used. Unfortunately it was not possible to determine the molecular weight distribution of the dye-conjugates by DLS and AF4/MALLS due to interferences of the fluorescence dye with the instrument's laser (690 nm). However, the NHS-ester of the dye cannot lead to cross linking reactions and enhanced self-assembly of the molecules is unlikely due to the hydrophilic and highly negatively charged nature of the dye. Also, the AF4 elution profile was not altered compared to those of the respective amine-modified polymers (RI-detector) and therefore a significant change in the molecular weight distribution is very unlikely. The broad molecular weight distributions of the plasma expanders could generally be regarded as a disadvantage compared to synthetic polymers, which often have more narrow distributions and low polydispersity, provided that the synthesis is well controlled. On the other hand, polysaccharide based polymers are available at a very large scale at low costs and still could be further processed or fractionated to obtain polymers with narrow molecular weight distribution. However, the non-fractionated material was used in the experiments.

3.4.4 Biodistribution and Elimination Studies

The biodistribution of the conjugated polymers was investigated in nude mice by multispectral FLI. four mice of each group were injected intravenously with 1.5 mg polymer in 100 μ L isotonic solution (sorbitol), which results in an initial blood concentration of 0.8 – 1.4 mg/mL (mouse weight: 20g-35g, blood volume (v/m): ~ 5.5 % of body weight²⁷¹). The injected solutions were particle free, isotonic and sterile. The background signal and the autofluorescence of the mice were subtracted from the emitted fluorescence by the Maestro™ software and the total fluorescence signal was compared to the total initial fluorescence after injection. All polymers were detectable in mice for several days, whereas the fluorescence intensity from an ester of dextran 500

with the same dye (control) decreased to 3 % of the initial fluorescence intensity within one day (Figure 37). This was probably due to the rapid cleavage of the ester. No accumulation in the liver was observed after the injection of the dextran-ester, which leads to the conclusion that the rapid cleavage of the ester happened faster than the liver accumulation of dextran.

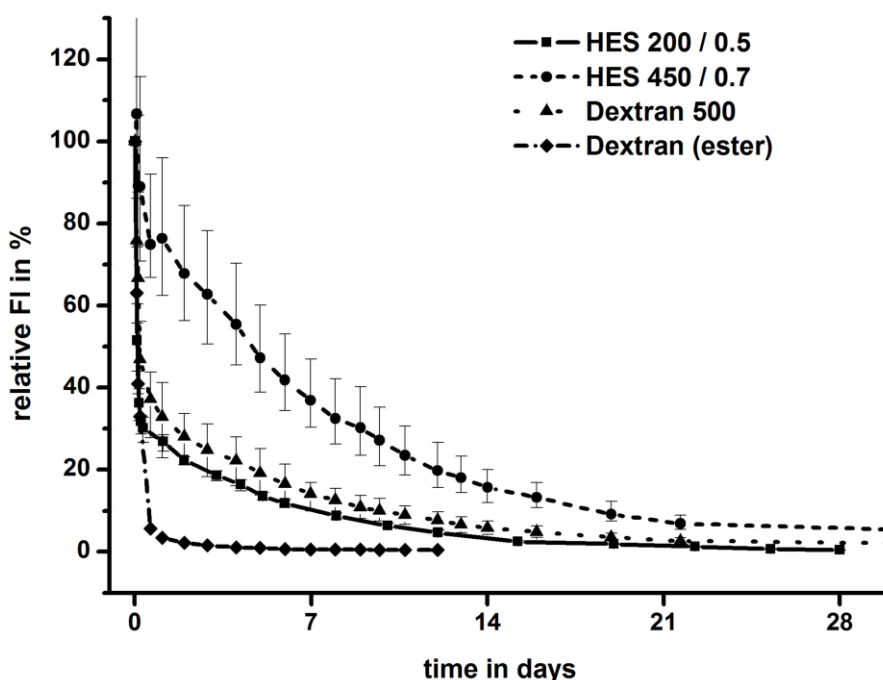


Figure 37. Elimination of the PVE polymers can be observed by measuring the decreasing fluorescence intensity from the mouse body (data represent means \pm minimum and maximum values. Dextran (ester): $n=1$, all others: $n=3$).

Interestingly, the fluorescence signal of a HES 200 derivative decreased as fast as the ester control when 1,8-octyl diamine was used as spacer between the dye and the polymer instead of ethylenediamine, which leads to the conclusion that the chain length of the amine spacer is important for a stable conjugate. All polymers showed a rapid initial decrease of the fluorescence intensity that can be explained by the rather broad molecular weight distribution. The lower molecular weight fraction – below renal excretion threshold – is rapidly excreted with the urine, which is also evident in a strong bladder signal in the first hours after injection (Figure 38). HES 450 was excreted very slowly compared to the other polymers, which can be attributed to the higher molecular weight on the one hand and to the higher degree of substitution with hydroxyethyl groups (HES 450: 0.7/AGU; HES 200: 0.5/AGU) reducing enzymatic degradation on the other hand.²⁷² Especially substitution at C₂ and high substitution degrees are known to

slow down enzymatic degradation effectively.²⁷³ These results are in good agreement with a study in humans.²⁷⁴

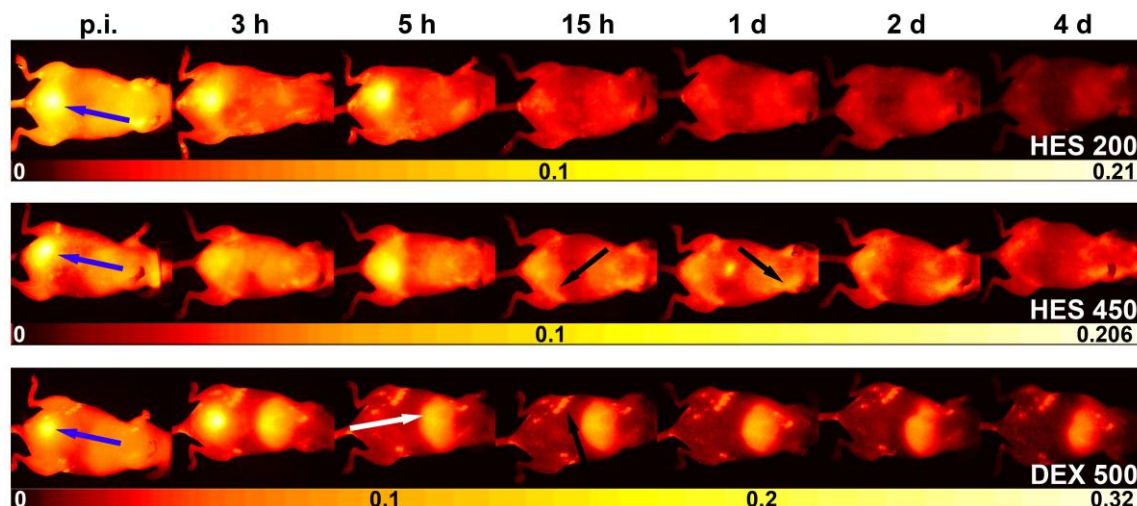


Figure 38. Representative *in vivo* images after injection of 1.5 mg polymer-NIR conjugate. Arrows point to bladder (blue), lymph nodes (black) and liver (white). The bladder signal indicates renal excretion. A particular liver accumulation can be observed for dextran only.

The fluorescence intensity of HES 450 did not decrease below 5 % of the initial fluorescence intensity up to 22 days after injection. The elimination kinetics was not only dependent on the molecular weight distribution, but also on the structure of the polymers. Dextran 500 (D_z : ≈ 100 kDa) was slower eliminated than HES 200 (D_z : ≈ 130 kDa), which can be explained on the one hand with the increased liver uptake and accumulation and on the other hand with the more branched structure of dextran. Dextran accumulated strongly and rapidly in the liver of the mice, whereas the hydroxyethyl starches were distributed much more homogeneously (Figure 38). All polymers – and especially dextran – accumulated also in regions of lymph nodes. Investigations of the autopsied organs of one mouse that was sacrificed one day after polymer injection confirmed the strong liver accumulation of DEX 500, whereas no particular accumulation of both hydroxyethyl starches was found (Figure 39).

Liver accumulation is undesired in most cases as it will lead to increased elimination of the drug delivery system from the blood stream and liver toxicity.^{220,221} Liver accumulation of dextran was reported to occur due to structure-specific receptor mediated uptake into hepatocytes.²⁷⁵ In most cases liver accumulation of nano-scaled drug delivery systems can be explained by RES mediated uptake into the macrophages

and Kupffer cells in liver and spleen, which is dependent on the structure, size, charge and surface polarity of the particles.^{224,225,276} However, there is no strong difference between DEX and HES in these properties and RES uptake does not seem to play a key role here, which is also evident in the low fluorescence signal from the spleen. Compared with most nanoparticulate drug delivery systems, it is clearly an advantage of the hydroxyethyl starches not to accumulate excessively in the liver or spleen. This can be probably attributed to the very hydrophilic properties that prevent the recognition and removal from the blood stream by the reticuloendothelial system. Furthermore there is as well no particular accumulation of the polymers in the ovaries observable, which recently was reported for a variety of structurally different nanocarriers.¹⁵⁵ The main difference between DEX and HES are the much higher degree of branching and that DEX is not substituted with hydroxyethyl groups.

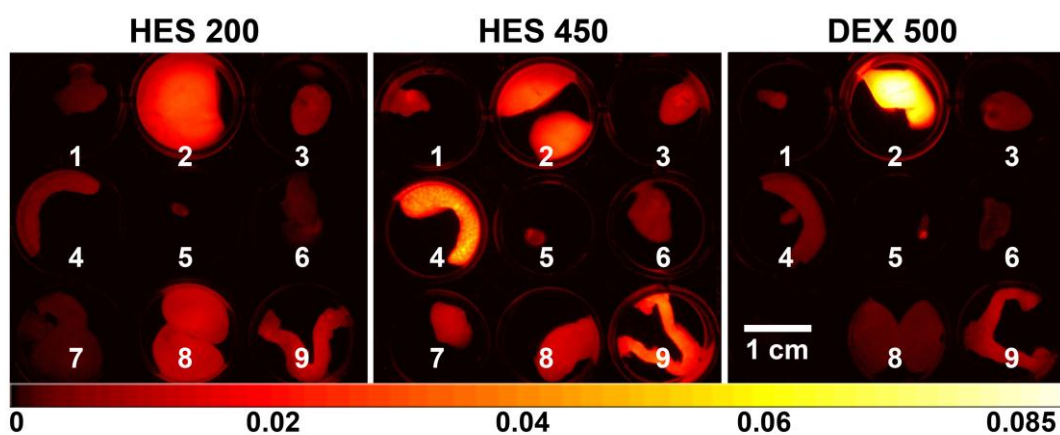


Figure 39. *Ex vivo* images of the autopsied organs from one mouse of each group one day after injection. For each image: 1 - fat, 2 - liver, 3 - heart, 4 - spleen, 5 - gallbladder, 6 - lung, 7 - intestine, 8 - kidneys, 9 - uterus and ovaries.

3.4.5 Tumor Accumulation Studies

Previous experiments with synthetic HPMA copolymers suggested that EPR-based accumulation of polymers in colon carcinoma xenografts is time dependent in the scale of days (cp. Figure 27, p. 61). Due to the long circulation time and rather slow initial decrease of the fluorescence intensity, HES 450 was chosen as the most suitable candidate for a possible tumor targeted delivery. Human colon carcinoma xenograft bearing male athymic nude mice were prepared by subcutaneous cell suspension injection of HT-29 and DLD-1 cells to the right and left flank of three mice (cp. chapter 2.2.7.3, p. 23). NIR-HES 450 (1.5 mg in 100 μ L isotonic sorbitol solution, sterile) was injected into the tail vein of the mice 21 days after tumor cell inoculation. At this time the

tumors had a volume of $0.57 \pm 0.18 \text{ cm}^3$ (HT-29) and $1.05 \pm 0.29 \text{ cm}^3$ (DLD-1). The mice were imaged *in vivo* for the following 42 h and sacrificed afterwards with respect to the tumor burden. No particular difference in tumor accumulation between the two xenograft models was observed (Figure 40), which is in agreement with results obtained with HPMA copolymers (cp. Figure 27, p. 61).

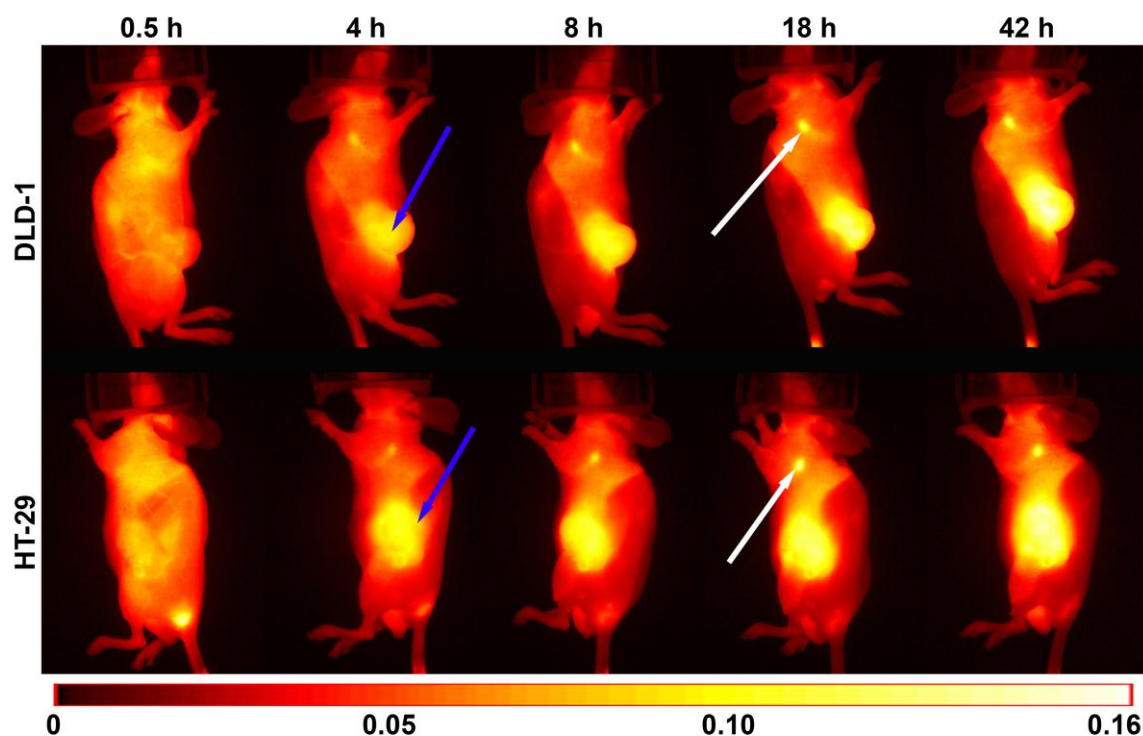


Figure 40. Representative time dependent *in vivo* images of a colon carcinoma xenograft bearing mouse after injection of 1.5 mg HES 450. Top (right flank): DLD-1, bottom (left flank): HT-29. Blue arrows point to the tumors and white arrows point to fluorescent lymph nodes.

For a better comparability of the fluorescence images with previous results, the “tumor accumulation value” (TAV) was calculated (cp. 3.1.6.3, p. 44 ff.). Analyzing the TAV, a time dependent tumor accumulation of HES 450, which is independent from the tested xenograft model, was confirmed (Figure 41 A). With HES 450 at least a comparable tumor accumulation as described for 200 kDa HPMA copolymers (DLD-1: 2.02 ± 0.22 and HT-29: 2.05 ± 0.11 after 49 hours) was achieved already after 42 h (DLD-1: 2.69 ± 0.65 and HT-29: 2.90 ± 0.42). As the number of animals in this pilot study was small, this result needs further confirmation. All mice were sacrificed 42 hours after injection. Relevant mouse organs were extracted and imaged *ex vivo* to confirm the *in vivo* results and to investigate the distribution in mouse organs in more detail (Figure 41

B). Comparing the fluorescence intensity from the tumors with other autopsied mouse organs a specific high local accumulation in the tumors could be confirmed.

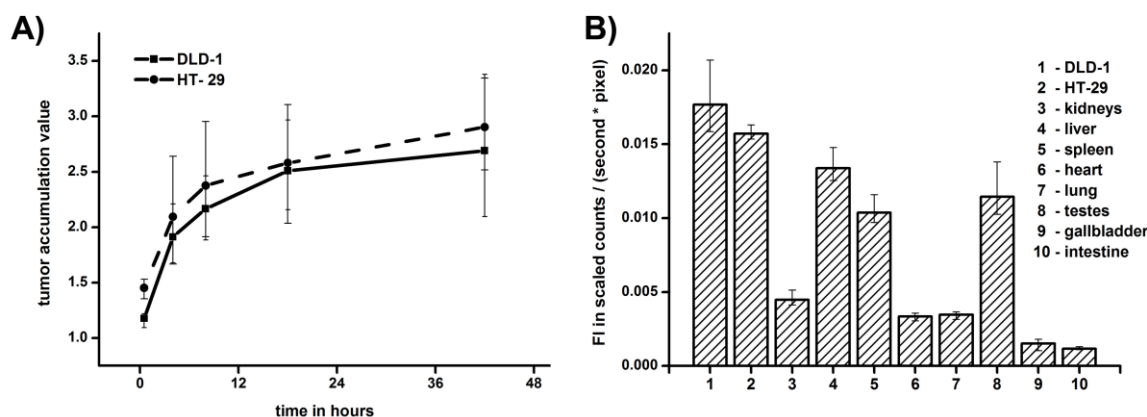


Figure 41. **A:** A comparable tumor accumulation value was calculated from the images for both tumors. **B:** The fluorescence intensity measured from organs that were extracted two days after injection of HES 450. Data represent means \pm minimum and maximum values, $n=3$.

The highest fluorescence intensity was measured in both tumors, followed by liver, spleen and testes. The polymer presence in liver and spleen can be explained by a combination of non-pronounced and non-specific RES-uptake and the comparably high blood content of these organs. It could be discussed that the polymer-dye conjugate content in liver and spleen is even higher than displayed in Figure 41, as the high blood content absorbs much more light, than for example the tumor tissue. To minimize this effect, NIR light with good tissue penetration was analyzed.

The high fluorescence intensity in the testes is interesting and cannot be explained and needs further detailed investigations. It was not yet observed in the previous biodistribution studies as female mice were used here. A high concentration of ^{14}C -HES (165 kDa) in the testes of rabbits has already been reported after intravenous injection, but the mechanism has not been investigated so far.²⁷⁷ However, potential accumulation in testes should be investigated in more detail in further studies. The tumors were sliced and imaged for a more detailed estimation of the tumor targeting effect and to explore the distribution within the tumors. Apart from a stronger signal at the tumor rim (rim-effect), the distribution of HES 450 in the tumors was rather homogeneous (Figure 42). A rim-effect in both colon carcinoma xenografts was already observed by MRI.²⁷⁸ It can be explained by various histological differences in the tumor structure compared to the central region.²⁷⁹

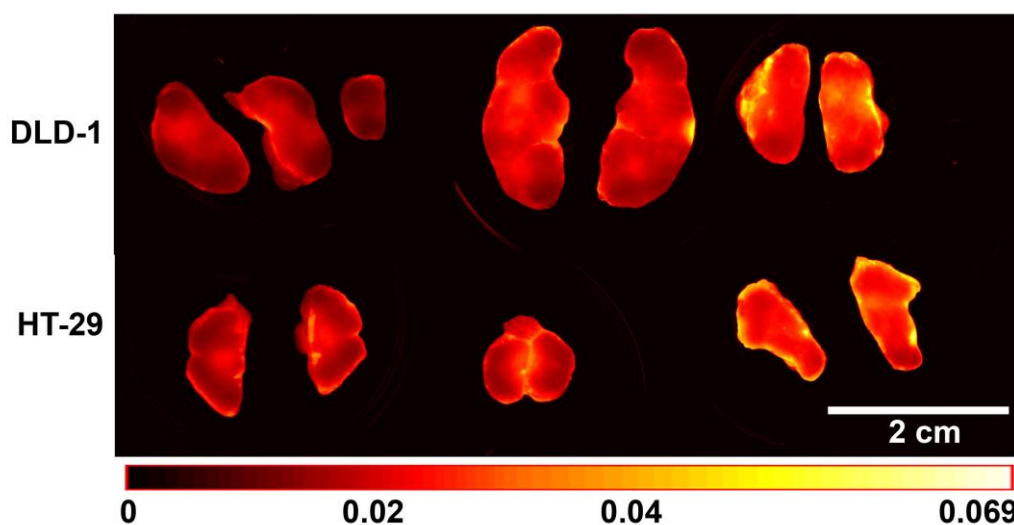


Figure 42. *Ex vivo* images of autopsied xenograft colon carcinomas from three mice two days after injection of HES 450. A homogeneous distribution is observable, apart from a bright tumor rim (rim-effect).

The interesting tumor-targeting results with HES, combined with the already mentioned advantages of carbohydrate plasma expanders led to subsequent investigations with NIR conjugated HES as diagnostic polymer for the detection of tumors.²⁸⁰ For these studies HES 200 was used and the tumor accumulation was found to be comparable to HES 450.²⁸⁰

3.4.6 Summary

Polysaccharide-based polymers are an interesting alternative to synthetic polymers for polymer therapeutics or diagnostics. They are inexpensive and available in large quantities with a broad range of molecular weights and substitution degrees.^{247,248} It was demonstrated that these polymers are nontoxic to hepatocellular carcinoma cells (HepG2) and have low immunogenic potential, which is consistent with previous literature reports. All investigated polymers showed a broad molecular weight distribution, which presents a certain disadvantage compared to synthetic polymers. Amine modification had a notable effect on the molecular weight distribution, which should be further investigated. The highly cross-linked dextran exhibited a notably stronger accumulation in the liver compared to the hydroxyethyl starches. Moreover, dextran was excreted slower than the larger HES 200 (amine-modified polymers), which could be ascribed to the pronounced liver uptake. No specific accumulation in liver or spleen was found for the hydroxyethyl starches. This is an advantage compared to most

nanoparticles or nanocapsules, even when they are coated with hydrophilic polymers.¹⁵⁴ Based on the *in vivo* data in healthy mice, the most promising polymer (HES 450) was used to demonstrate the EPR-based passive tumor accumulation in human xenograft colon carcinomas. A comparable tumor accumulation was measured as it was found with HPMA copolymers in the same tumor models. These results emphasize the potential of polysaccharide-based polymers as contrast agents for solid tumor or metastasis detection or possible drug delivery systems for tumor therapy. They prove that passive tumor accumulation based on the EPR-effect is possible using this class of well-known polymers.

3.5 Polymers from Glutamic Acid (PGA)

Polymers based on poly-L-glutamic acid have been investigated regarding the design of polymer-drug conjugates for drug delivery for more than 20 years now.^{281,282} This class of polymers is biocompatible, biodegradable and the pendant carboxyl-groups provide reactivity for conjugation of active compounds. Therefore polyglutamates present to be an interesting alternative to HPMA copolymers, which are not biodegradable and thus limited to a molecular weight below the renal excretion threshold in the clinical setting.¹²²

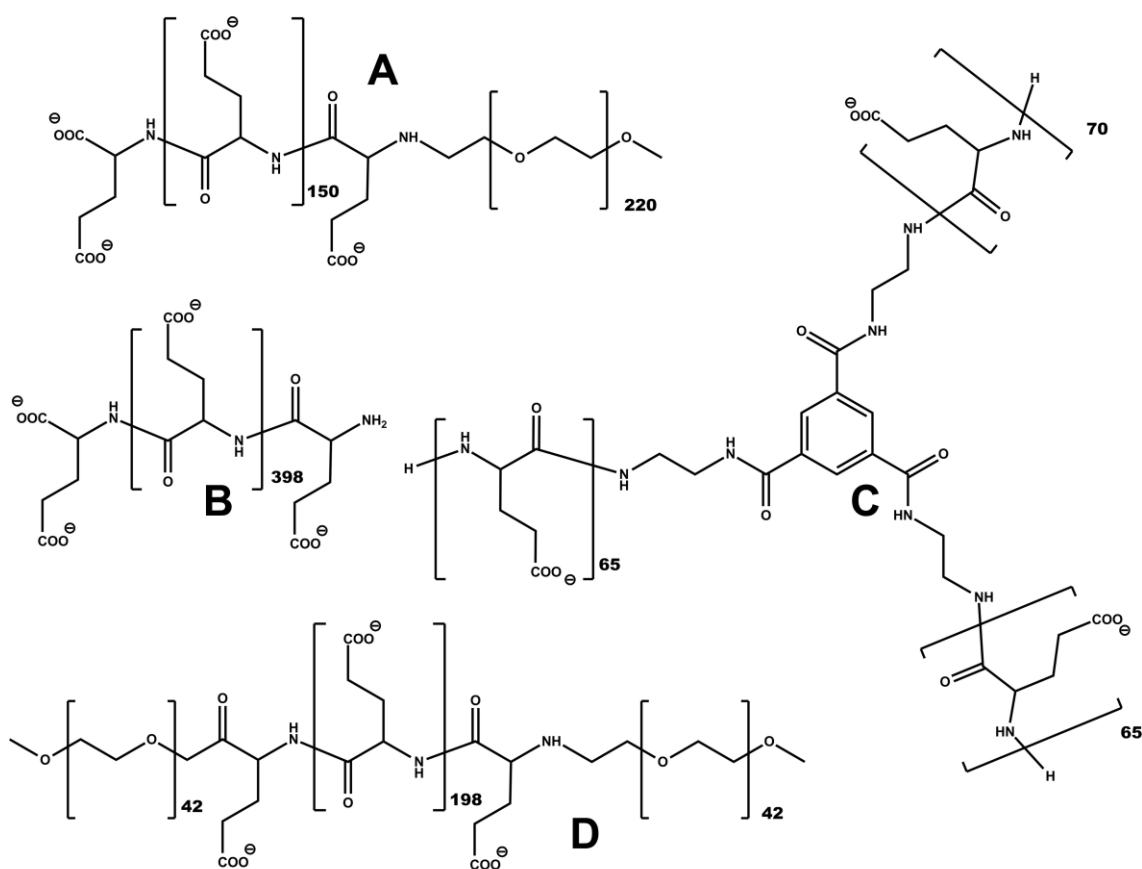
In recent years, various PGA-drug conjugates have been synthesized and investigated particularly for the treatment of cancer.^{110,283-286} Although no market authorization has been approved yet, some of these conjugates made the leap from preclinical to clinical studies in the last decade. The most advanced candidate is Paclitaxel poliglumex (OpaxioTM, formerly XyotaxTM) from Cell Therapeutics Inc. (USA). Several clinical studies demonstrating the efficacy of Paclitaxel poliglumex have been published in the last years.²⁸⁷⁻²⁹² In 2008, a marketing authorization application for OpaxioTM as a treatment of non-small cell lung cancer (NSCLC) has been submitted to the EMA.⁸⁴ However, the application was withdrawn in 2009 due to concerns of the Committee for Medicinal Products for Human Use (CHMP) regarding the efficacy, release mechanism and product purity.^{131,132} Nonetheless, further studies with OpaxioTM in various cancers are made and recently OpaxioTM received the orphan drug designation for the treatment of glioblastoma multiforme (GBM) from the FDA.²⁹³

Several structures of poly- α -L-glutamic acid have been synthesized by cooperation partners in València (Spain) using γ -benzyl-protected glutamic acid N-carboxyl anhydrides (NCA).^m Detailed description of the synthesis conditions is not part of this thesis and therefore omitted here. The synthesized structures included linear and star-like polymers as well as PEG-PGA di-block copolymers and PEG-PGA-PEG tri-block copolymers of different molecular weight. As the cooperation partners suspected micelle-formation of the tri-block copolymers, besides molecular weight distribution hemolytic activity has to be also investigated. The most promising polymers were chosen to be investigated *in vivo* for comparison with the HPMA copolymers and carbohydrate polymers described in previous chapters.

^m Synthesis of poly-L-glutamic acid polymers: Centro de Investigación Príncipe Felipe (CIPF), C/ Eduardo Primo Yúfera, 3 (junto Oceanográfico), 46012 València, Spain (Fabiana Canal, Richard M. England and Maria J. Vicent).

3.5.1 Characterization of Molecular Weight Distribution

After polymerization reaction the molecular weight distribution and thus the degree of polymerization of the benzyl-protected polymers was assessed with GPC by the cooperation partners. The de-protected polymers were analyzed by AF4 to confirm the molecular weight in aqueous solution after the de-protection reaction and lyophilization. The AF4 analyzes were carried out as described in section 2.2.4.2. The polymers were measured in PBS, simulating physiologically relevant pH and osmolality. As a simplification, a refractive index increment (dn/dc) of 0.180 was initially used for molar mass calculation. This value is in consistency with the values used for poly-glutamic acid in literature, where dn/dc values between 0.150 and 0.190 are reported.²⁹⁴⁻²⁹⁷ The four most promising polymers – all showing different structures, narrow mono-modal size distributions and a suitable molecular weight – were chosen for further characterization (structures are presented in Scheme 7).



Scheme 7. Structures of the PGA-based polymers chosen for further characterization: **A:** a PEG-PGA di-block-copolymer (DB-PGA-150). **B:** a linear PGA (L-PGA-400). **C:** a star-PGA (S-PGA-200). **D:** a PEG-PGA-PEG tri-block-copolymer (TB-PGA-200). The numbers represent the theoretical average degree of polymerization (DP).

The precise dn/dc of these polymers was determined as described previously (cp. 2.2.4.2, p. 15 ff.) by measuring the refractive index of different polymer concentrations (Figure 43 A). Thereafter, the AF4 chromatograms were reprocessed using the correct dn/dc . The mean molecular weight of the polymers and the precise dn/dc are presented in Table 10.

Table 10. AF4 results of the PGA-based polymer chosen for further characterization. M_W : weight-average molar mass; M_N : number-average molar mass; M_W/M_N : polydispersity value; dn/dc : refractive index increment used for calculation. All measurements are means of independent duplicates ($n=2$).

Polymer	M_W by GPC	M_W measured by AF4	M_W/M_N	dn/dc
L-PGA-400	35 kDa	16 kDa	1.34	0.156 mL/g
S-PGA-200	30 kDa	20 kDa	1.07	0.169 mL/g
DB-PGA-150	24 kDa	25 kDa	1.14	0.147 mL/g
TB-PGA-200	29 kDa	40 kDa	1.18	0.148 mL/g

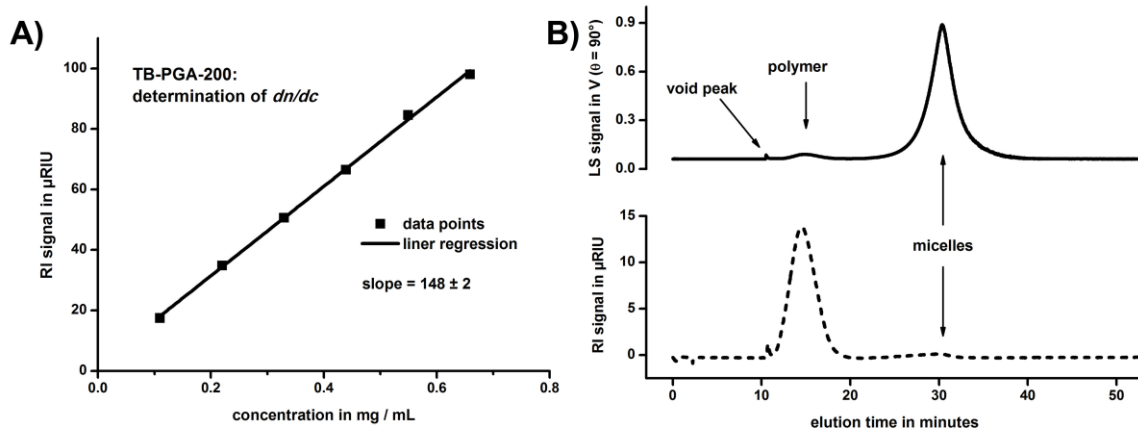


Figure 43. **A:** The refractive index increment was determined from the slope of measured RI from different polymer concentrations in PBS. **B:** A small proportion of Micelles were found for the PEG-PGA block-copolymers (DB-PGA-150 and TB-PGA-200), which were characterized by a small RI signal (RI proportional to concentration) and a large light scattering signal (angle dependent LS proportional to size).

The molecular weight determined by AF4 was notably smaller for most of the investigated polymers compared to the molecular weight predicted from GPC data. Conformation changes of the polymers in aqueous environment or polymer degradation during the de-protection reaction may be discussed as a possible reason for this effect.

Further, a second peak was detectable in the elugram of both PEG-PGA block-copolymers (Figure 43 B). Elution time, high light scattering intensity and small RI-signal indicated the presence of a small proportion of large polymeric micelles. The particle diameters (D_z) were calculated to be about 80 nm for the TB-PGA-200 and about 135 nm for the DB-PGA-150 using the particles mode of the software. Micelles could not be detected for the PGA-polymers without PEG. The micelle formation process could be explained by an intermolecular hydrogen bond core formed by the glutamic acid groups and the more hydrophilic PEG shell, although this was not further investigated.

The elution profiles of the polymers chosen for further characterization indicated a narrow molecular weight distribution (Figure 44), especially in comparison with the molecular weight distribution of the carbohydrate plasma volume expanders (cp. Figure 36, p. 78). The tailing effect of the L-PGA-400 and S-PGA-200 (Figure 44 A and B) can be explained by the presence of very small molecules below the MWCO of 5 kDa here, which are flushed out of the channel by the cross-flow. Thus, the average molecular weight analyzed by AF4 may be slightly overestimated.

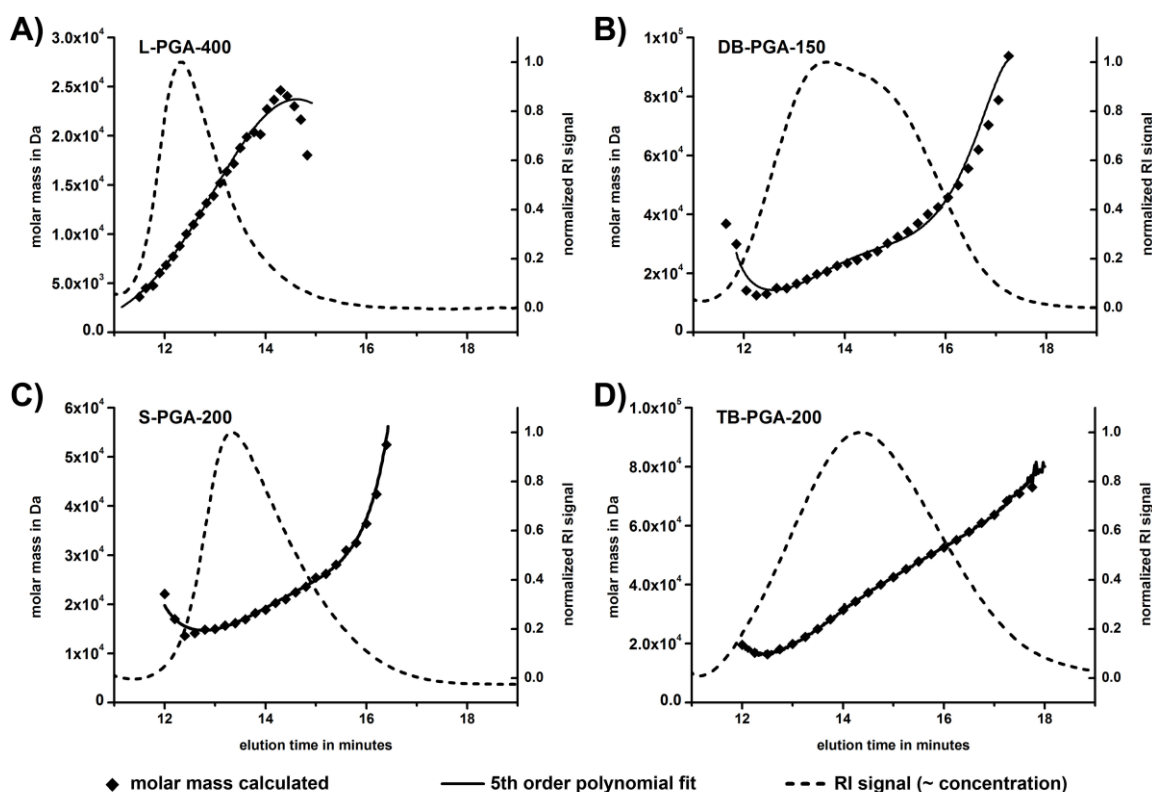


Figure 44. Elution profiles of PGA-based polymers. The polymers present a monomodal and narrow molecular weight distribution.

3.5.2 Hemolytic Activity Assay

Assessing the hemolytic activity of the polymers was necessary prior to *in vivo* experiments with intravenous administration, as surface active properties of some polymers could be assumed from previous data. Formation of micelles was reported by the cooperation partners for the tri-block copolymers and also the AF4 data indicated formation of micelles from PEG-PGA block-copolymers. Thus surface active properties could be concluded at least for the PEG-PGA block-copolymers. As surface active substances might de-stabilize cellular membranes and thus promote hemolysis of red blood cells, all polymers intended for *in vivo* characterization were tested for hemolytic activity in a PBS solution of human RBCs. The polymers showed no significant influence on red blood cell hemolysis during 60 minutes compared to a control in PBS (Figure 45), indicating that intravenous administration will not lead to hemolytic anemia.

$$A = c * k * \frac{1}{f_{Dil}} \rightarrow c = \frac{A * f_{Dil}}{k}$$

$$\frac{c_X}{c_T} = \frac{A_X * f_{Dil(X)}}{A_T * f_{Dil(T)}}$$

$$H [\%] = 100 * \frac{A_X}{A_T * 50} = 2 * \frac{A_X}{A_T}$$

$$SE [\%] = 2 * \left(\frac{SD(A_X)}{A_X} + \frac{SD(A_T)}{A_T} \right) * H [\%]$$

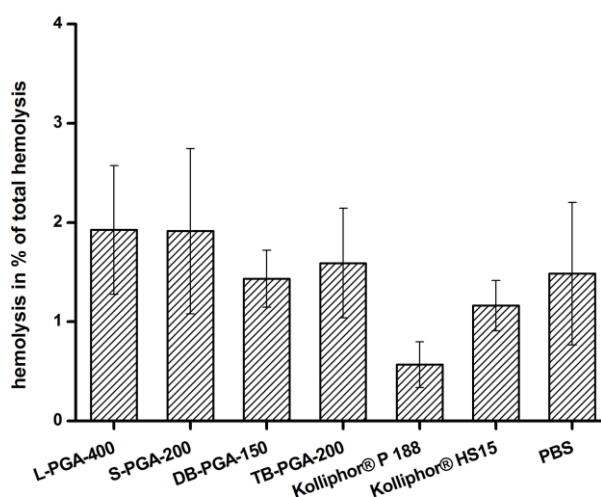
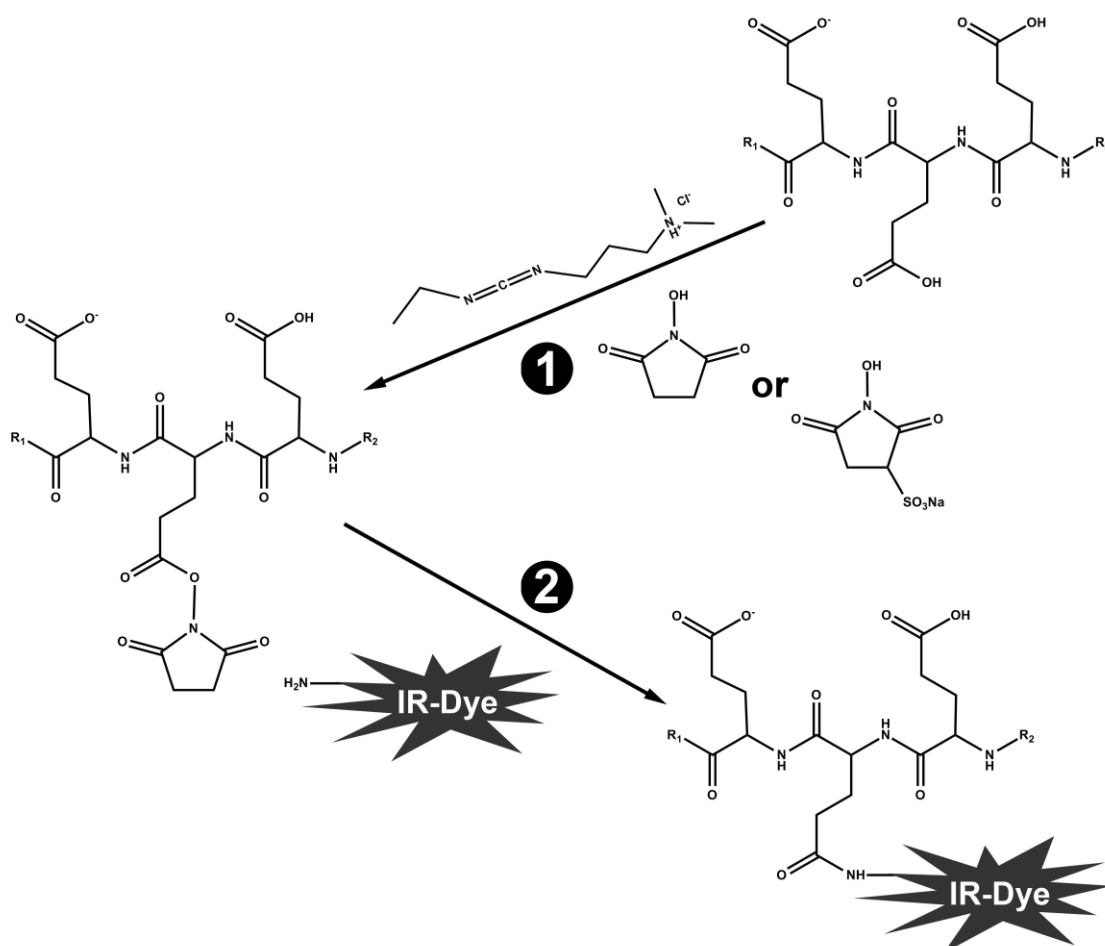


Figure 45. Hemolytic activity (H) of the polymers was calculated as a proportion of total hemolysis (measured after incubation with SDS) and was found to be in the range of the RBC control in PBS. Reference samples were incubated with commercial emulsifiers used in intravenous drug formulation (Kolliphor®). A : absorption, c : concentration, f_{Dil} : dilution factor, k : constant product of molar absorptivity (ϵ) and absorption path length (d), X refers to polymer sample and T refers to total hemolysis; data represent means \pm standard errors (SE); $n=3$.

3.5.3 Synthesis of NIR-Fluorescent PGA-Dye Conjugates

As the polymers based on PGA presented a carboxyl group as reactive site, an amine modified NIR-fluorescent dye (DY-781-Amine) was chosen for amide bond formation. The polymers were activated with NHS or sulfo-NHS, which is a common and favorable activation method.²⁹⁸ sulfo-NHS is known to form more stable water-soluble activated

esters than NHS and was used for conjugation of L-PGA-400 and DB-PGA-150, to investigate whether or not there is a difference in the reactivity compared to the use of NHS, which was applied for the activation of S-PGA-200 and TB-PGA-200. Although the use of sulfo-NHS is reported to be preferable,²⁹⁸ no difference in reaction success was observed in this case which might be explained by the excellent water-solubility of the PGA-polymers. Thus, having polymers presenting good solubility in aqueous media, NHS can be used for activation instead of the much more expensive sulfo-NHS. The PGA-dye conjugates have been synthesized in water as described previously based on a commonly used method (cp. chapter 2.2.1.3, p. 14).²⁹⁸ The principle of the reaction is presented in Scheme 8.



Scheme 8. Reaction of PGA-based polymers with an amine modified NIR-fluorescent dye after activation with EDCI and NHS or Sulfo-NHS. **1:** activation reaction, **2:** dye conjugation reaction.

After purification by dialysis against water and subsequent lyophilization intensively purple colored and NIR-fluorescent polymer-dye conjugates were obtained. For the

interpretation of the following *in vivo* studies, the high molecular weight of the fluorescent dye in relation to the polymer molecular weight has to be taken into consideration (783 Da, cp. Scheme 2, p. 12) as it might affect the polymer biodistribution. Certainly, changing the properties of polymers may be discussed as a disadvantage of FLI.

3.5.4 Biodistribution and Elimination in Mice: TB-PGA-200

To evaluate the bio-compatibility and biodistribution of the synthesized fluorescent PGA-based polymers, a first *in vivo* study was performed in four nude female SKH-1 mice. A reference spectrum of the DY-781-TB-PGA-200 conjugate was recorded previously *in vitro* with 1 mg/mL polymer solution. Each mouse was intravenously injected into the tail vein with 100 μ L polymer solution (isotonic with sorbitol and sterile filtered) containing 1 mg of the polymer. The fluorescence signal was observed *in vivo* for several days from three mice and one mouse was sacrificed and autopsied after one day for a more detailed view on the biodistribution *ex vivo*. Immediately after injection, a high fluorescence signal was detectable from the kidneys of all mice, indicating a specific local accumulation in the kidneys and renal elimination. Six hours after injection an accumulation was also detectable in the liver and in some lymph nodes. High specific fluorescence signals were also measured from certain bones, especially from the thighbone and lower leg in the region of the knee joint and from the spinal column. Representative images measured two days after injection of the polymer solution are presented in Figure 46.

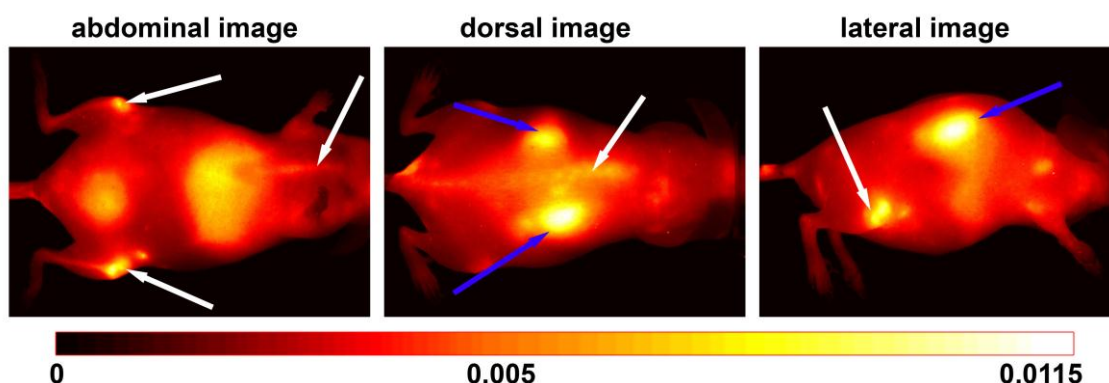


Figure 46. Biodistribution of the fluorescence signal in a mouse two days after injection of 1 mg DY-781-TB-PGA-200 conjugate. A high fluorescence signal could be measured from certain bones (marked by white arrows) and from the kidney (marked by blue arrows) and the liver.

A major part of the polymers was rapidly excreted. The fluorescence intensity decreased to 80 % of the initial fluorescence intensity within two days after injection (Figure 47 A). However, even 30 days after injection a very weak fluorescence signal was still detectable from the knee joints. The autopsied organs from a mouse that was sacrificed one day after polymer injection confirmed the *in vivo* observations (Figure 47). Highest fluorescence intensity was measured from the kidneys, but also the knee joint showed a high local and specific accumulation of the PEG-PGA tri-block-copolymer.

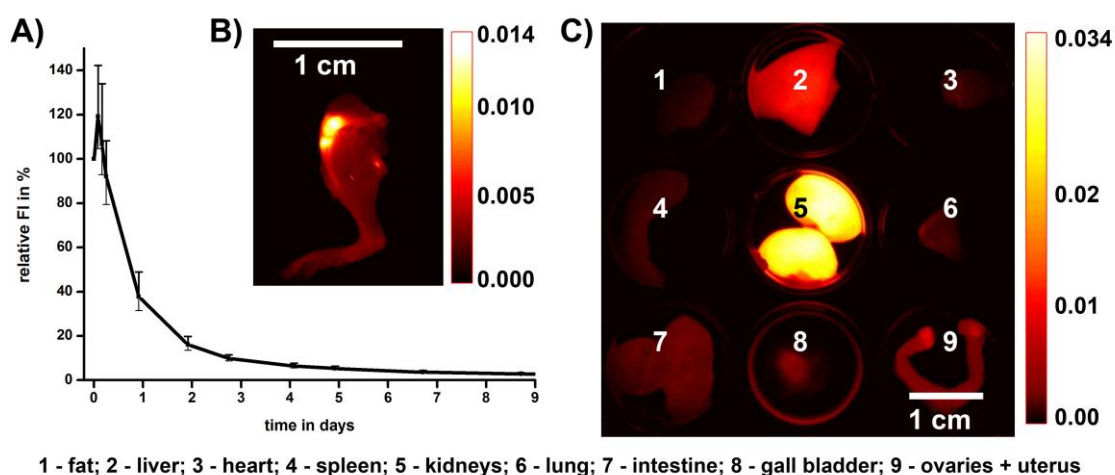


Figure 47. **A:** Elimination curve of TB-PGA-200. The fluorescence signal decreased by 80 % within the first two days after injection indicating a rapid excretion of the polymer. **B and C:** Organs and the leg without skin of a mouse that was sacrificed and autopsied 24 h after polymer injection. A high accumulation in the kidneys and in the bones at the knee joint is confirmed.

3.5.4.1 Ex Vivo Characterization of Kidney Accumulation

The kidneys of a nude female mouse (SKH-1) were extracted 24 h after injection of 1 mg TB-PGA-200 in 100 μ L isotonic sorbitol solution to investigate the kidney accumulation in more detail. MaestroTM images of axial kidney sections (freshly prepared by razor blade) suggested an accumulation of the polymer-dye conjugate especially in the kidney cortex (Figure 48). These findings were confirmed by CLSM. Fluorescence spectroscopy revealed a second emission maximum of the NIR-fluorescent dye at 708 nm at an excitation wavelength of 633 nm (measured with a Jasco FP-8200 fluorescence spectrometer). Although the quantum yield was poor compared to the primary emission maximum at 800 nm, fluorescence of the dye could be measured in a range of 639 – 758 nm by excitation with the 633 nm HeNe laser.

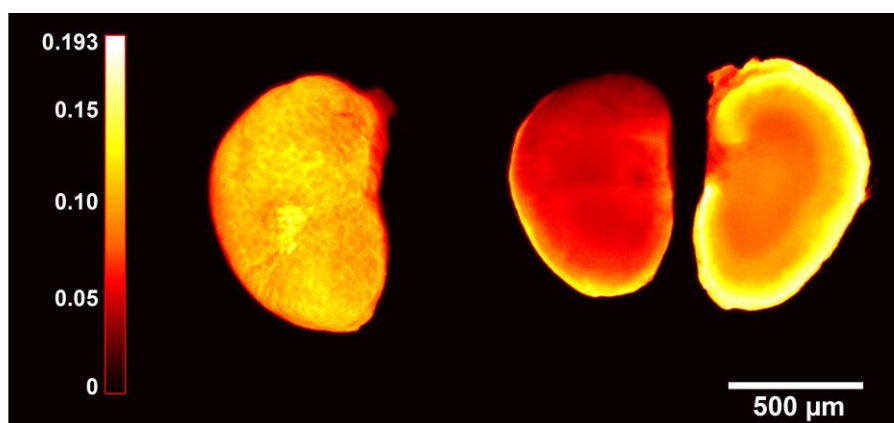


Figure 48. *Maestro™* fluorescence images of the extracted kidneys from a mouse autopsied 24 h after injection of 1 mg TB-PGA-200 in 100 μ L isotonic sorbitol solution. Left: exterior view, right: axial section.

Whereas in the *Maestro™* images of axial kidney sections the central part of the kidney seems to be also fluorescent, CLSM images show fluorescence solely from the cortex. The difference can be explained by deep penetration and multiple scattering of NIR light in the *Maestro™* fluorescence imaging process, leading to diffuse fluorescent signals also from the non-fluorescent central region of the kidney. The *Maestro™* image is a two-dimensional projection of a 3-dimensional fluorescent object. Most likely, the fluorescence in the central kidney region is caused by fluorescence of the deeper kidney cortex. The resolution is decreased due to multiple scattering events of NIR light. These effects were diminished by CLSM as fluorescence was excited and measured very precisely in a plane layer and only at an area of $2.75 \mu\text{m}^2$ (Figure 49 A) or $0.32 \mu\text{m}^2$ (Figure 49 B) at the same time, respectively. The CLSM images confirmed the specific accumulation of the polymer-dye conjugate in the kidney cortex, but however no plausible explanation could be derived from the images. As accumulation in the kidney was observed as well for all other investigated PGA based polymers (cp. Figure 55, p. 101), a specific structure dependent relation may be concluded and might also be regarded as a toxicity issue. However, an influence of the fluorescence dye has to be taken into consideration as well, especially as the dye is large in relation to the comparable small polyglutamates. For the chemically comparable dye DY-782 (cp. Scheme 2, p. 12) a rapid elimination within 1 day has been detected, although it seemed to accumulate in the kidneys during the first hours, likely due to renal elimination. Interestingly, kidney accumulation or renal toxicity has not yet been discussed in literature for *Opaxio™* or other polyglutamates. In the experimental studies within this work no mouse showed any obvious toxic effects from the polymer carriers, but with

regards to a potential conjugation of cytotoxic agents, the strong accumulation in the kidney seems to be a disadvantage over the other investigated polymer structures. It should be confirmed by other analytical techniques like MRI in further studies, to exclude a specific phenomenon due to fluorescence conjugation. However, accumulation in joints is interesting and unusual. It could be as well exploited for targeted delivery of certain drugs.

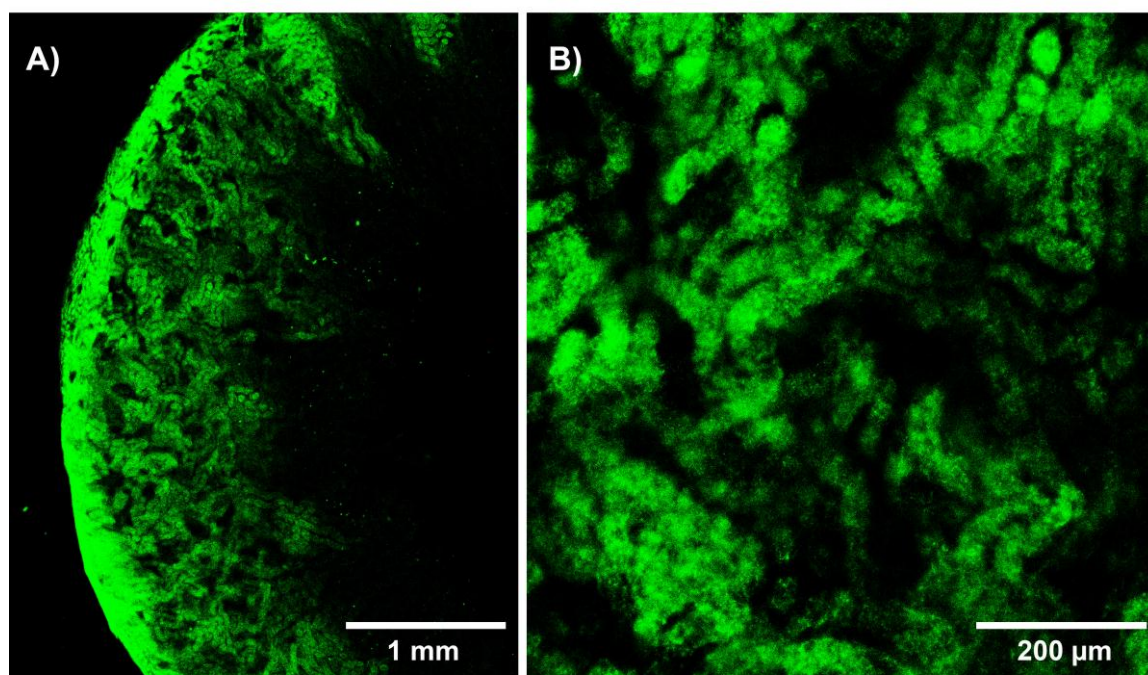


Figure 49. CLSM images of a kidney from a mouse that was autopsied 24 h after injection of 1 mg TB-PGA-200-DY-781 conjugate (green pseudo-colored). **A:** Overview of kidney cross section **B:** Detailed view on cortex structure, presumably glomeruli.

3.5.5 TB-PGA-200: Tumor Accumulation

The PEG-PGA-PEG tri-block copolymer exhibiting the highest molecular weight was chosen for a first explorative study in three male tumor bearing mice, because a very short circulation time was expected for the smaller PGA-polymers and previous results with HPMA copolymers indicated a time dependent tumor accumulation in the scale of days. Xenograft tumor-bearing mice were prepared as described previously (cp. chapter 2.2.7.3, page 23). 1.5 mg polymer in 100 μL isotonic sorbitol solution were injected 19 days after tumor cell inoculation, by which time the xenograft tumors had an average volume of $0.24 \text{ cm}^3 \pm 0.1 \text{ cm}^3$ (HT-29, left flank) and of $0.98 \text{ cm}^3 \pm 0.1 \text{ cm}^3$ (DLD-1, right flank), respectively. The elimination rate and biodistribution pattern was comparable with that observed in SKH-1 mice. Already one day after injection a notable tumor

accumulation was observed (Figure 50). Seven days after polymer injection the mice had to be sacrificed due to the tumor burden. A specific tumor accumulation was detectable over the whole observation period of one week. The organs of the mice were autopsied for *ex vivo* fluorescence imaging after sacrifice and a high accumulation in the tumors could be confirmed (Figure 51). A higher accumulation was observed in DLD-1, which could be ascribed to a more pronounced EPR-effect due to the increased growth rate and altered tumor microstructure (compare discussion in chapter 3.1.7.3, p. 52 ff.).

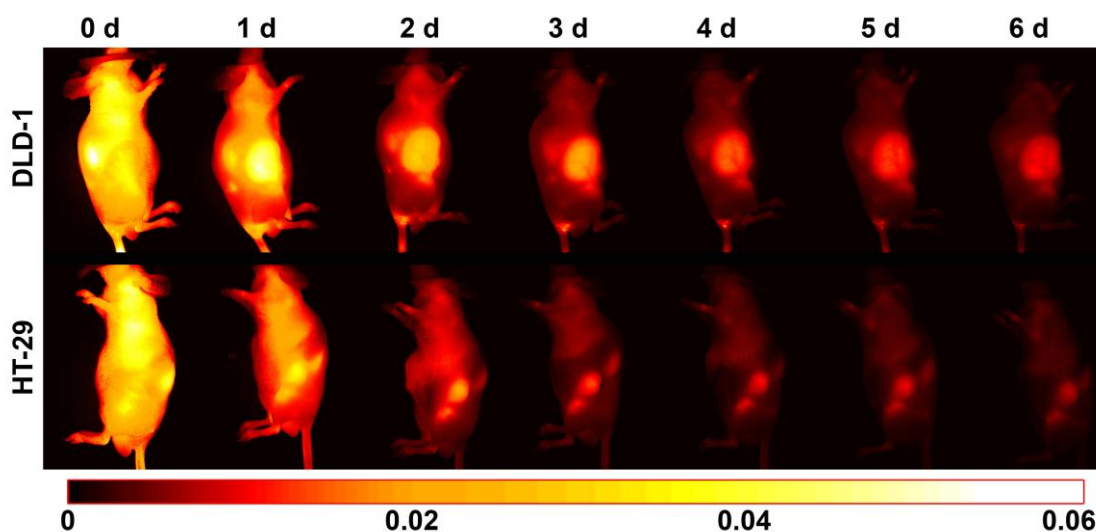


Figure 50. Lateral fluorescence images of a representative tumor bearing mouse treated with fluorescent TB-PGA-200. Top (right flank): DLD-1 and bottom (left flank): HT-29. The polymer accumulates in both tumors and is rapidly eliminated.

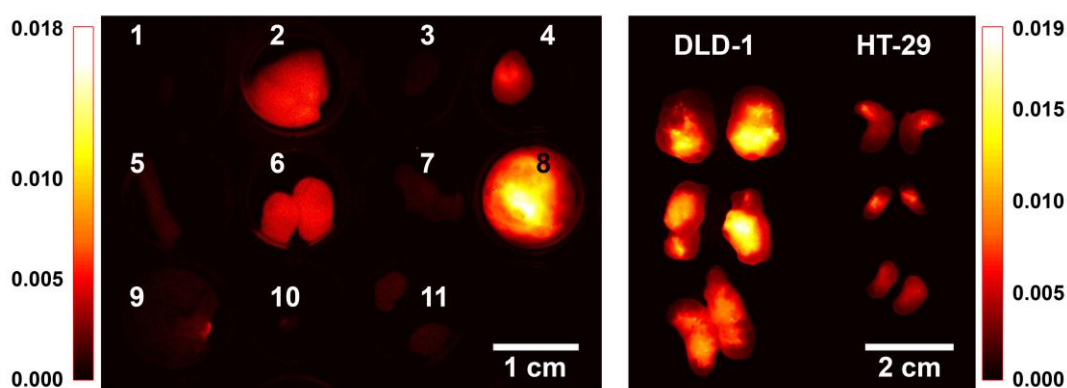


Figure 51. Left: Representative fluorescence component image of mouse organs extracted seven days after TB-PGA-200 injection. 1 – bladder, 2 – liver, 3 – heart, 4 – HT-29 tumor, 5 – spleen, 6 – kidneys, 7 - lung, 8 – DLD-1 tumor, 9 – intestine, 10 – gallbladder, 11 – testes. Right: Autopsied tumors (cross sliced) from 3 mice: a better accumulation is observable in DLD-1, especially in the center.

3.5.6 Tumor Accumulation: Variation of PGA Structures

Based on the promising tumor accumulation results of TB-PGA-200, the tumor accumulation of three other PGA-based polymers with varying size and architecture was characterized in the same xenograft mouse model (cp. Table 10, p. 89). The tumor volume at the day before polymer injection (19 days after tumor cell inoculation) was comparable for the different PGA structures, but for all of them smaller than it has been for TB-PGA-200 (cp. Table 11). All polymers showed a specific tumor accumulation in the xenograft models for the observation period, especially in DLD-1 (Figure 52).

Table 11. The tumor volume of HT-29 and DLD-1 one day before polymer injection as determined by caliper measurement. Apart from TB-PGA-200, the tumor volume of the groups is comparable. Volumes are given in cm^3 as means \pm SD.

Tumor	TB-PGA-200	S-PGA-200	L-PGA-400	DB-PGA-150
HT-29	$0.24 \pm 0.10 \text{ cm}^3$	$0.05 \pm 0.02 \text{ cm}^3$	$0.09 \pm 0.09 \text{ cm}^3$	$0.05 \pm 0.02 \text{ cm}^3$
DLD-1	$0.98 \pm 0.10 \text{ cm}^3$	$0.40 \pm 0.24 \text{ cm}^3$	$0.36 \pm 0.14 \text{ cm}^3$	$0.39 \pm 0.15 \text{ cm}^3$

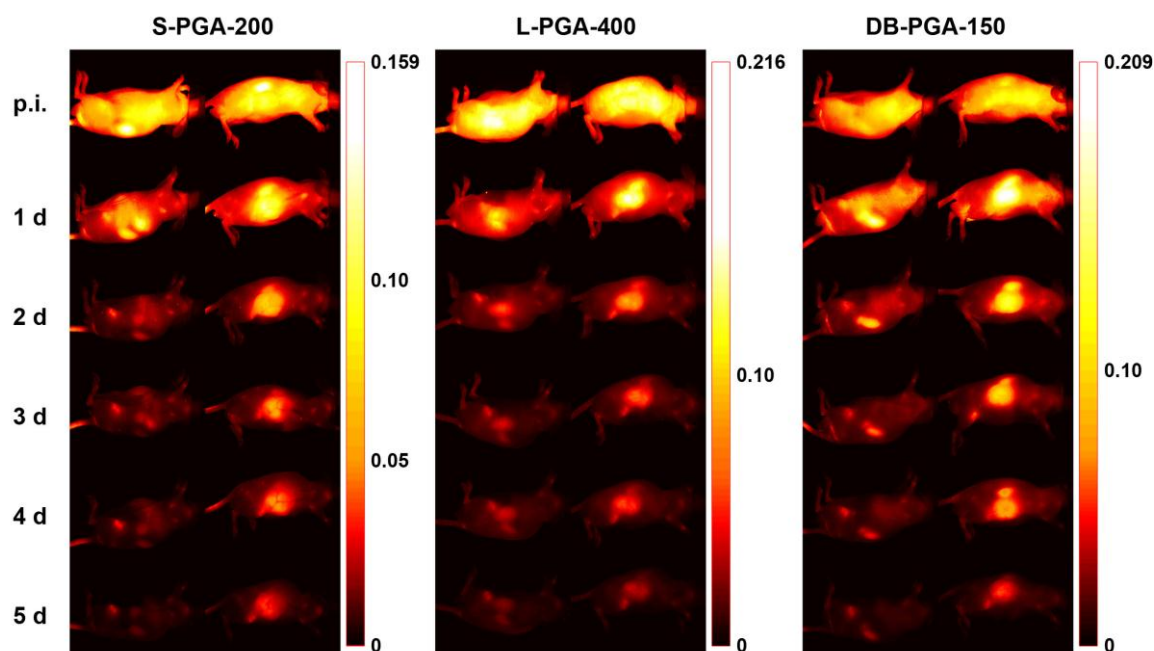


Figure 52. Representative fluorescence component images of tumor bearing mice (left: HT-29 and right: DLD-1) that were treated with different fluorescent PGA-polymers. An accumulation in the kidneys and in both tumors is detectable and rapid elimination can be observed for all polymers. No structure-related difference in biodistribution is observable.

The biodistribution pattern of all polymers was comparable with that of TB-PGA-200, independently from the polymer structure, whereas the elimination rate of the three smaller PGA-structures was slightly higher compared to that of TB-PGA-200 (Figure 53 A). High local fluorescence intensities were measured for all polymers from the kidneys, tumors, bones and also from the liver (Figure 53 B). For better comparability of the tumor accumulation, the tumor accumulation value (cp. chapter 3.1.6.3, p. 44 ff.) has been calculated for each group (Figure 53 C and D.)

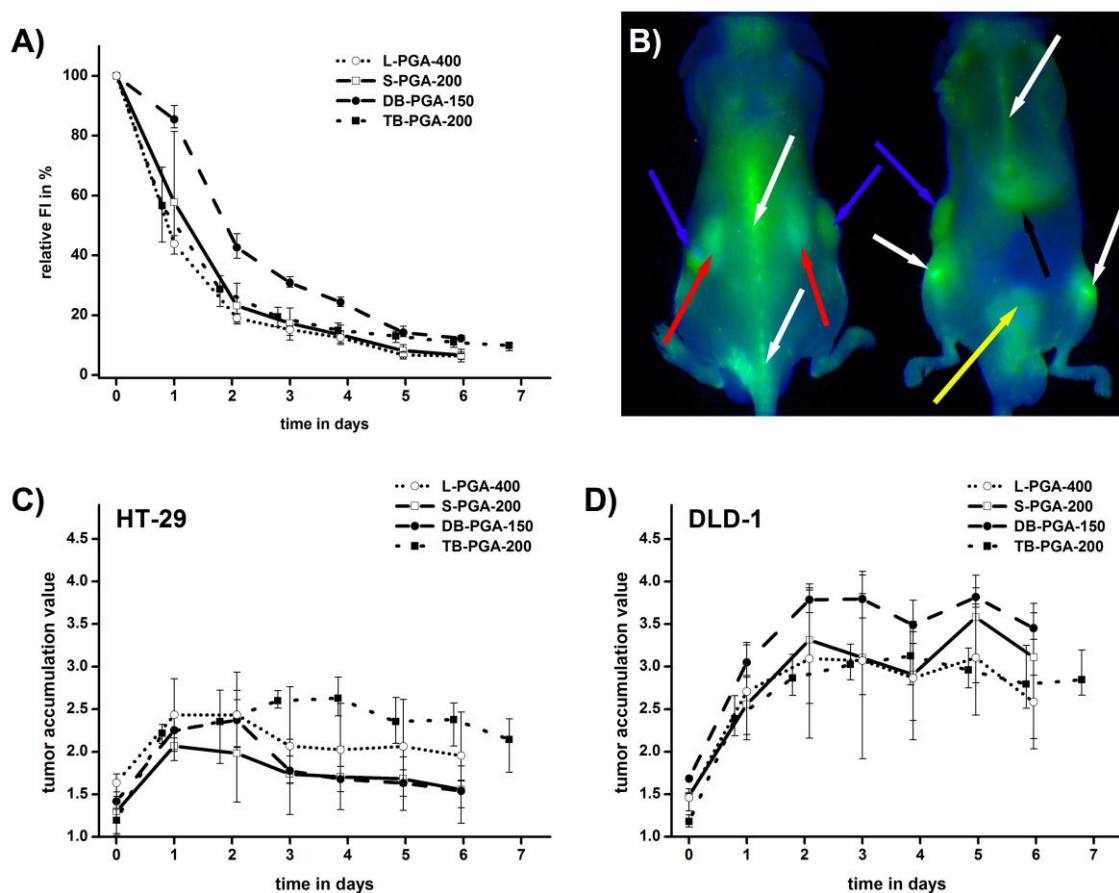


Figure 53. A: The elimination rate is comparable for three of the PGA-polymers, but slightly lower for TB-PGA-200, which can be explained with the higher molecular weight compared to the other polymers (cp. Table 10, p. 89). **B:** Pseudo-colored fluorescence image (left: dorsal, right: abdominal) of a nude mouse two days after injection of L-PGA-400. Green: polymer fluorescence, blue: autofluorescence of the mouse. The specific biodistribution pattern was observed for all PGA-polymers. Arrows point to the tumors (blue), bones and joints (white), kidneys (red), bladder (yellow) and to the liver (black). **C and D:** The tumor accumulation value of the PGA-polymers was observed to be smaller in HT-29 than in DLD-1. No significant difference between the polymers was detectable. TB-PGA-200 showed the highest accumulation in the DLD-1 xenograft model (TAV about 4). Data represent means \pm minimum and maximum values, $n=3$.

As it was observed already for HPMA copolymers and HES-450, the TAV was markedly higher in DLD-1 compared to HT-29. Considering all the data from tumor accumulation experiments, a model-dependent difference in the tumor accumulation in DLD-1 and HT-29 is very likely. The most probable explanation for higher tumor enrichment in DLD-1 is the more pronounced EPR-effect due to increased growth rate and presence of necrotic/fibrotic areas in this tumor model. The tumor accumulation was slightly higher for TB-PGA-200 compared to the other polymers. This may be ascribed to the increased tumor size in this group, which results in more necrotic/fibrotic areas leading to increased retention of the polymer. The increasing tumor size and weight loss of the mice led to the end of the experiment six days after polymer injection and subsequent autopsy of mouse organs. The fluorescence images of the organs confirmed a high local accumulation in DLD-1, liver and kidneys (Figure 54). The extracted HT-29 tumor obviously exhibited a lower fluorescence signal compared to DLD-1, confirming lower tumor accumulation (Figure 55 B). As already observed for TB-PGA-200, the kidneys showed a higher polymer concentration at the rim compared to the center, whereas the polymers were accumulated rather in central parts of the tumors (Figure 55). This can be explained with necrotic/fibrotic regions especially in the tumor center.

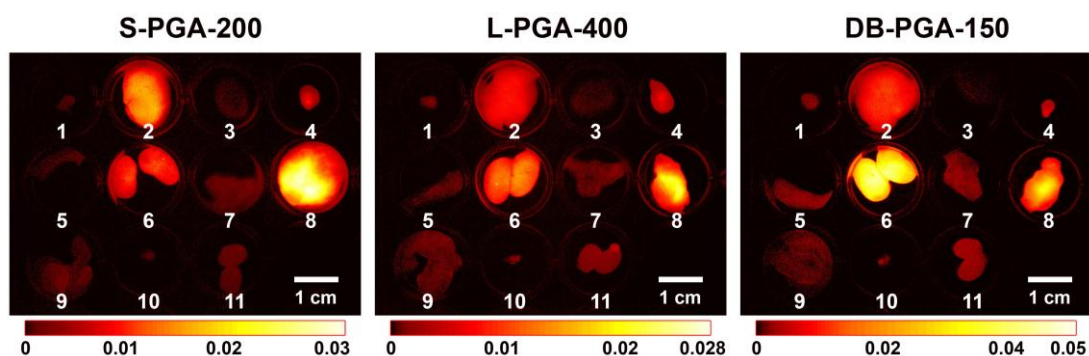


Figure 54. Representative component images of the polymer fluorescence signal from organs of a mouse of each group. Organs were extracted six days after polymer injection. Highest fluorescence signals could be measured mainly from the tumors, kidneys and the liver. For each image from left to right: Top – bladder, liver, heart and HT-29. Middle – spleen, kidneys, lung and DLD-1. Bottom – intestine, gallbladder, and testes.

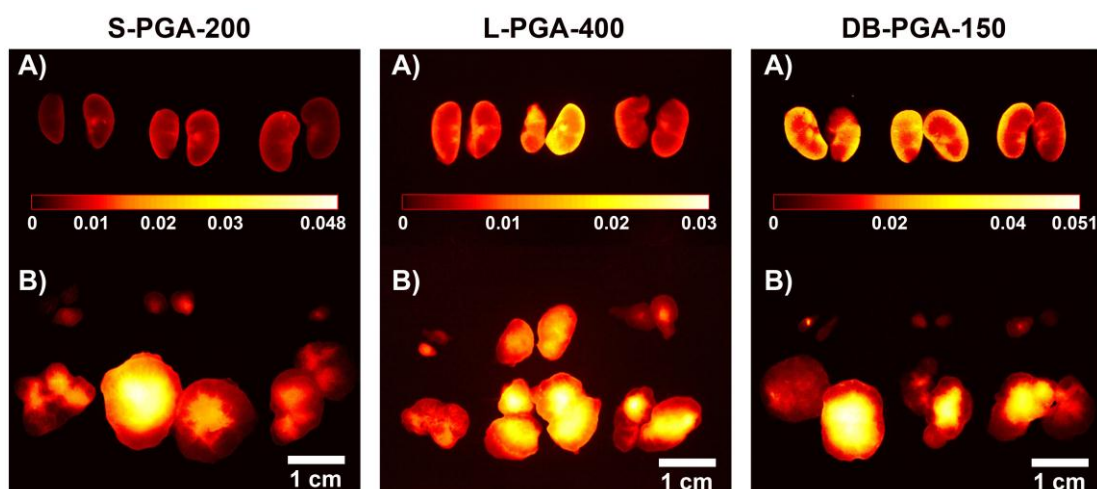


Figure 55. Cross slices of extracted kidneys (A) and tumors (B) – top HT-29, bottom DLD-1 – from all mice of each group. As shown previously for TB-PGA-200 (cp. Figure 48, p. 95), the polymer accumulated in a small rim of the kidney cortex. Tumor accumulation was observed to be much higher in DLD-1.

3.5.7 Summary

Polymers based on poly-glutamic acid present to be an interesting platform for the design of polymer conjugates for passive tumor targeting. Various different polymer architectures exhibiting a narrow molecular weight distribution were prepared by cooperation partners. After detailed characterization of the molecular weight distribution by AF4, the most promising candidates were selected and subsequently conjugated with an NIR fluorescent dye and characterized *in vivo* and *ex vivo* in a nude mouse tumor model. It was demonstrated that these polymers are suitable for passive tumor targeting independently from the polymer architecture. The results obtained from multispectral FLI revealed a high local accumulation of the polymers not only in the xenograft tumor models, but as well in kidneys and bones, especially in the region of cartilages, like knee joint, spine and sternum. This interesting PGA-specific effect should be further investigated, as it could be exploited for the development of a specific bone- or cartilage targeted drug delivery system, which for instance might be useful for the treatment of cancer metastases or as well other specific diseases. However, the mechanism of this specific effect, which was not observed for other investigated polymer classes within this work, is yet unknown. Although no mice showed any pathologic effect from the accumulation in the kidney cortex, this effect should be as well investigated in more detail in further studies using other analytical techniques than FLI.

4 Summary and Perspectives

Polymer conjugates arouse particular interest in medicine as drug delivery systems for targeted tumor therapy, but the relationship between the polymer structure, molecular weight and the fate in the living organism is not understood in detail yet. Within this work three structurally different polymer classes have been investigated with the aim to contribute to the understanding of this relationship and to identify suitable candidates for passive tumor targeting based on the EPR effect: HPMA copolymers, carbohydrates and polyglutamates. The molecular weight distribution of the polymers was characterized in detail and major toxicity issues have been experimentally addressed. Several polymers from each class have been investigated *in vivo* in nude mice with regard to biodistribution and elimination properties. Therefore fluorescence labeled derivatives of the polymers have been either obtained by cooperation partners (HPMA copolymers) or synthesized within the frame of this work (polyglutamates, carbohydrates).

Non-invasive near-infrared multispectral FLI allowed the evaluation of the body fate of all polymers. The observed biodistribution pattern particularly depended on the polymer class, but no strong dependency on the molecular weight or polymer architecture was found within one polymer class. HPMA copolymers preferentially accumulated in the kidneys, whereas carbohydrates showed slight enrichment in the liver and lymph nodes. The polyglutamates showed a high specific affinity to the kidneys and to bones and cartilages that might be an interesting observation with regard to a potential bone targeted drug delivery system. However, it has to be stressed out by all means that – besides dextran - none of the characterized polymers showed extensive liver accumulation as it is a common observation for nanoparticles or nanocapsules. Undoubtedly, this seems to be a great advantage of water soluble polymers, because the risk of potential hepatotoxicity is minimized and the circulation time of a potential drug in the blood stream is increased. Also, none of the investigated polymers showed local and specific accumulation in the ovaries, which has been recently reported for nanoparticulate drug delivery systems.

The carbohydrate polymers and polyglutamates have been conjugated each with a single fluorescent dye to assess the effects of the polymer in the body, whereas the HPMA copolymers were conjugated by cooperation partners with two fluorescent dyes with different emission spectra. One of them served as a non-cleavable polymer label

and the other one as a pH-dependent cleavable drug model. Thus it was possible to observe the biodistribution of both, the drug model and the polymer simultaneously by use of multispectral FLI. After the characterization of biodistribution and elimination, the proposed tumor accumulation due to the EPR-effect has been demonstrated in human colon carcinoma xenograft bearing athymic nude mice. The accumulation in tumors could be observed excellently by multispectral FLI. Interestingly, all investigated polymers accumulated in the tumor models. The accumulation in DLD-1 was always higher than in HT-29, which may be ascribed to an increased growth rate and a different tumor microstructure, which was substantiated by histology. With various HPMA copolymer derivatives it was proven *in vivo* by multispectral FLI that the release rate of the drug model can be controlled by the chemical environment of the spacer.

One major obstacle in fluorescence imaging techniques is that results are hardly quantifiable. Several influences on the emitted light have to be taken into consideration, such as absorption, scattering, autofluorescence and quenching. Quenching is very hard to predict in complex matrices or even *in vivo*. It turned out to be impossible to calculate concentrations from the measured fluorescence intensity *in vivo*. However, the tumor accumulation was nevertheless quantified in this work after development of a relative quantification approach. Thus, results from different polymers and different mice could be compared. It could be argued that fluorescence imaging is an inappropriate method for *in vivo* characterization of polymers because the used labels might change the polymer properties, especially for the rather small polyglutamates and the linear HPMA copolymer. This can be certainly discussed as disadvantage of the method and it is recommended to verify the promising results of this work in future by use of other imaging techniques, such as PET or MRI. However, multispectral FLI turned out to be easy to use and cheap, which makes it valuable especially for screening purposes in preclinical research.

The promising results of the tumor accumulation studies with HPMA copolymers ultimately led to a treatment study in xenograft tumor bearing mice with doxorubicin-conjugated HPMA copolymers. Although the human colon carcinoma tumor model in this study was doxorubicin resistant, an improved efficacy and reduced toxicity of the polymer-drug conjugate compared to free doxorubicin has been demonstrated. The results of this explorative study should be confirmed by further investigations in other tumor models. Tumors with slower growth rate are recommended for a longer possible observation period. It has to be stated that the subcutaneous tumor models used in this work have the advantage to be easily accessible and observable, but exhibit poor

clinical relevance. Twan Lammers commented subcutaneous tumor models at the European Summerschool of Nanomedicine 2011 in Wittenberg with the following statement: “Nobody is dying from a local, solid tumor, because solid tumors would be simply removed by surgery. People are dying from metastases.” Bearing this in mind, the results of this work have to be confirmed in clinically more relevant orthotopic and metastasizing tumor models, exhibiting more realistic biological properties, such as vascularization and infiltration.

Within this work, evidence has been found that multiple dosing with the polymers would lead to an increased tumor accumulation. This effect should be further investigated in ongoing studies. The cellular uptake of the polymer conjugates into the tumor cells has not been experimentally addressed in the focus of this work. Most proposed release mechanisms of the active substance from polymer-drug conjugates focus on intracellular release, for instance in the endosomes. Thus, the polymer drug conjugates have to enter the cells, but obviously, not everything that is nano-sized is taken up into tumor cells as those would be otherwise flooded with plasma proteins of the blood, for instance. Therefore, further studies should focus also on proving the cellular uptake of the various polymers by internalization experiments and investigate the uptake mechanism.

5 Appendix

5.1 List of Chemicals, Reagents and Solvents

Substance	Source/Origin	Remark
DY-676-NHS ester	Dyomics, Germany	
DY-782-NHS ester	Dyomics, Germany	
DY-781-Amine	Dyomics, Germany	
IRDye [®] 800CW	LI-COR Biosciences, USA	
HES 200/0.5	Serumwerk Bernburg AG, Germany	Free sample batch 0473
HES 450/0.7	Serumwerk Bernburg AG, Germany	Free sample batch 0209
Dextran 500	Serumwerk Bernburg AG, Germany	Free sample batch 241/03
Ethylenediamine	Sigma-Aldrich, Germany	
p-Tosylchloride	Sigma-Aldrich, Germany	
Deuterium oxide	Sigma-Aldrich, Germany	
LPS from E. coli	Sigma-Aldrich, Germany	Escherichia coli 055:B5
EDCI	Sigma-Aldrich, Germany	
NHS	Sigma-Aldrich, Germany	
LSM 1077	PAA Laboratories, Austria	
Sodium Pyruvate	PAA Laboratories, Austria	solution
MEM medium	PAA Laboratories, Austria	(with Phenol Red)
Gibco [®] MEM	Life Technologies, USA	(without Phenol Red)
HepG2 cells	DSMZ-German Collection of Micro-organisms and Cell Cultures, Germany	
BD CBA cytokines	Becton, Dickinson and Company, USA.	Human inflammatory kit
Dimethylformamide	VWR, Germany	Analytical grade
Triethylamine	VWR, Germany	Analytical grade
Methanol	VWR, Germany	Analytical grade
Isopropanol	VWR, Germany	Analytical grade
Dialysis Membrane	Spectrum Labs, USA	MWCO 3.5 kDa
Sterile filters	Millipore, USA	0.2 µM PTFE
Forane [®]	Abbott, Germany	For veterinary use

Other materials were used as received. Buffers used in the experiment were standardized buffers unless otherwise stated. Other organic solvents and chemicals used were technical grade.

5.2 References

- 1 Duncan R and Vicent MJ. Do HPMA copolymer conjugates have a future as clinically useful nanomedicines? A critical overview of current status and future opportunities. *Adv Drug Delivery Rev* 2010; 62(2): pp 272-282.
- 2 Soerjomataram I, Lortet-Tieulent J, Ferlay J, Forman D, Mathers C, Parkin D and Bray F. Estimating and validating disability-adjusted life years at the global level: a methodological framework for cancer. *BMC Med Res Methodol* 2012; 12:125.
Available from: <http://www.biomedcentral.com/1471-2288/12/125>
- 3 Ferlay J, Shin H-R, Bray F, Forman D, Mathers C and Parkin DM. Estimates of worldwide burden of cancer in 2008: GLOBOCAN 2008. *Int J Cancer* 2010; 127(12): pp 2893-2917.
- 4 Jemal A, Bray F, Center MM, Ferlay J, Ward E and Forman D. Global cancer statistics. *Ca-Cancer J Clin* 2011; 61(2): pp 69-90.
- 5 Bray F, Ren J-S, Masuyer E and Ferlay J. Global estimates of cancer prevalence for 27 sites in the adult population in 2008. *Int J Cancer* 2013; 132(5): pp 1133-1145.
- 6 Press Release No 223. Latest world cancer statistics. Global cancer burden rises to 14.1 million new cases in 2012: Marked increase in breast cancers must be addressed. 2013. Lyon (FR): International Agency for Research on Cancer;
Available from: http://www.iarc.fr/en/media-centre/pr/2013/pdfs/pr223_E.pdf
- 7 Wolf U, Barnes B, Bertz J, Haberland J, Laudi A, Stöcker M, Schönfeld I and Kurth BM. Das Zentrum für Krebsregisterdaten (ZfKD) im Robert Koch-Institut (RKI) in Berlin. *Bundesgesundheitsblatt* 2011; 54(11): pp 1229-1234.
- 8 Todesursachen in Deutschland. 2012. Fachserie 4 Reihe 12 - 2011. Wiesbaden: Statistisches Bundesamt;
Available from: <https://www.destatis.de/DE/Publikationen/Thematisch/Gesundheit/Todesursachen/Todesursachen.html>
- 9 Kaatsch P, Spix C, Katalinic A, Hentschel S, Baras N, Barnes B, Bertz J, Dahm S, Haberland J, Kraywinkel K et al. Krebs in Deutschland 2007/2008. 8th ed. Berlin: Robert Koch-Institut und die Gesellschaft der epidemiologischen Krebsregister in Deutschland e.V.; 2012. ISBN: 978-3-89606-214-7.
- 10 Bertz J, Dahm S, Haberland J, Kraywinkel K, Kurth BM and Wolf U. Verbreitung von Krebserkrankungen in Deutschland: Entwicklung der Prävalenz zwischen 1990 und 2010. Berlin: Robert Koch-Institut; 2010. ISBN: 978-3-89606-208-6.
- 11 Neubauer G and Neubauer A. Krebs im Fokus - Häufigkeit und Kosten in Deutschland. Limburg an der Lahn: WORTREICH Gesellschaft für individuelle Kommunikation mbH; 2012. ISBN: 978-3-00-040302-6.
- 12 Haberland J, Wolf U, Barnes B, Bertz J, Dahm S, Laudi A and Kraywinkel K. Kurzfristige Prognosen der Krebsmortalität in Deutschland bis 2015. *UMID* 2012; 3: pp 16-23.
- 13 Luengo-Fernandez R, Leal J and Sullivan R. Economic burden of malignant neoplasms in the European Union. *Ann Oncol* 2012; 23(suppl 9): ix25.
Available from: http://annonc.oxfordjournals.org/content/23/suppl_9/ixe1
- 14 Hartmann M, Mayer-Nicolai C and Pfaff O. Approval probabilities and regulatory review patterns for anticancer drugs in the European Union. *Crit Rev Oncol Hemat* 2013; 87(2): pp 112-121.

- 15 Mullard A. 2011 FDA drug approvals. *Nat Rev Drug Discovery* 2012; 11(2): pp 91-94.
- 16 Mullard A. 2012 FDA drug approvals. *Nat Rev Drug Discovery* 2013; 12(2): pp 87-90.
- 17 Jansen L, Gondos A, Eberle A, Emrich K, Holleczeck B, Katalinic A and Brenner H. Cancer survival in Eastern and Western Germany after the fall of the iron curtain. *Eur J Epidemiol* 2012; 27(9): pp 689-693.
- 18 Cooper GM. The Development and Causes of Cancer. In: *The Cell: A Molecular Approach*. 2nd ed. Sunderland (MA): Sinauer Associates; 2000. ISBN: 0-87893-106-6.
- 19 Anand P, Kunnumakara AB, Sundaram C, Harikumar KB, Tharakan ST, Lai OS, Sung B and Aggarwal BB. Cancer is a preventable disease that requires major lifestyle changes. *Pharm Res* 2008; 25(9): pp 2097-2116.
- 20 Modan B, Mart H, Baidatz D, Steinitz R and Levin S. Radiation induced Head and Neck Tumours. *The Lancet* 1974; 303(7852): pp 277-279.
- 21 De Gonzalez AB and Darby S. Risk of cancer from diagnostic X-rays: estimates for the UK and 14 other countries. *The Lancet* 2004; 363(9406): pp 345-351.
- 22 Kellerer AM. Risk estimates for radiation-induced cancer - the epidemiological evidence. *Radiat Environ Biophys* 2000; 39(1): pp 17-24.
- 23 Sasco AJ, Secretan MB and Straif K. Tobacco smoking and cancer: a brief review of recent epidemiological evidence. *Lung Cancer* 2004; 45(suppl 2): pp S3-S9.
- 24 Kune GA, Kune S, Vitetta L and Watson LF. Smoking and colorectal cancer risk: data from the Melbourne Colorectal Cancer Study and brief review of literature. *Int J Cancer* 1992; 50(3): pp 369-372.
- 25 Engeland A, Andersen A, Haldorsen T and Tretli S. Smoking habits and risk of cancers other than lung cancer: 28 years' follow-up of 26,000 Norwegian men and women. *Cancer Cause Control* 1996; 7(5): pp 497-506.
- 26 Hecht SS. Cigarette smoking and lung cancer: chemical mechanisms and approaches to prevention. *Lancet Oncol* 2002; 3(8): pp 461-469.
- 27 Calle EE and Kaaks R. Overweight, obesity and cancer: epidemiological evidence and proposed mechanisms. *Nat Rev Cancer* 2004; 4(8): pp 579-591.
- 28 Bianchini F, Kaaks R and Vainio H. Overweight, obesity, and cancer risk. *Lancet Oncol* 2002; 3(9): pp 565-574.
- 29 Perz JF, Armstrong GL, Farrington LA, Hutin YJ and Bell BP. The contributions of hepatitis B virus and hepatitis C virus infections to cirrhosis and primary liver cancer worldwide. *J Hepatol* 2006; 45(4): pp 529-538.
- 30 Munoz N, Castellsague X, De Gonzalez AB and Gissmann L. HPV in the etiology of human cancer. *Vaccine* 2006; 24(suppl 3): pp S3/1-S3/10.
- 31 Croce CM. Oncogenes and cancer. *N Engl J Med* 2008; 358(5): pp 502-511.
- 32 Hanahan D and Weinberg RA. Hallmarks of cancer: the next generation. *Cell* 2011; 144(5): pp 646-674.
- 33 Hanahan D and Weinberg RA. The hallmarks of cancer. *Cell* 2000; 100(1): pp 57-70.

- 34 Pietras K and Östman A. Hallmarks of cancer: interactions with the tumor stroma. *Exp Cell Res* 2010; 316(8): pp 1324-1331.
- 35 Gilman A. The initial clinical trial of nitrogen mustard. *Am J Surg* 1963; 105: pp 574-578.
- 36 Goodman LS, Wintrobe MM, Dameshek W, Goodman MJ, Gilman A and McLennan MT. Nitrogen mustard therapy. *JAMA-J Am Med Assoc* 1984; 251(17): pp 2255-2261.
- 37 Papac RJ. Origins of cancer therapy. *Yale J Biol Med* 2001; 74(6): pp 391-398.
- 38 Sawyers C. Targeted cancer therapy. *Nature* 2004; 432(7015): pp 294-297.
- 39 Sasportas LS, Kasmieh R, Wakimoto H, Hingtgen S, van de Water JA, Mohapatra G, Figueiredo JL, Martuza RL, Weissleder R and Shah K. Assessment of therapeutic efficacy and fate of engineered human mesenchymal stem cells for cancer therapy. *Proc Natl Acad Sci* 2009; 106(12): pp 4822-4827.
- 40 Loebinger MR and Janes SM. Stem cells as vectors for antitumour therapy. *Thorax* 2010; 65(4): pp 362-369.
- 41 Roth JA and Cristiano RJ. Gene therapy for cancer: what have we done and where are we going? *J Natl Cancer Inst* 1997; 89(1): pp 21-39.
- 42 El-Aneed A. An overview of current delivery systems in cancer gene therapy. *J Controlled Release* 2004; 94(1): pp 1-14.
- 43 Rosenberg SA, Yang JC and Restifo NP. Cancer immunotherapy: moving beyond current vaccines. *Nat Med* 2004; 10(9): pp 909-915.
- 44 Finn OJ. Cancer vaccines: between the idea and the reality. *Nat Rev Immunol* 2003; 3(8): pp 630-641.
- 45 Ross JS, Slodkowska EA, Symmans WF, Puzstai L, Ravdin PM and Hortobagyi GN. The HER-2 receptor and breast cancer: Ten years of targeted anti-HER-2 therapy and personalized medicine. *Oncologist* 2009; 14(4): pp 320-368.
- 46 Ferrara N, Hillan KJ and Novotny W. Bevacizumab (Avastin), a humanized anti-VEGF monoclonal antibody for cancer therapy. *Biochem Biophys Res Commun* 2005; 333(2): pp 328-335.
- 47 Shawver LK, Slamon D and Ullrich A. Smart drugs: tyrosine kinase inhibitors in cancer therapy. *Cancer Cell* 2002; 1(2): pp 117-123.
- 48 Brigger I, Dubernet C and Couvreur P. Nanoparticles in cancer therapy and diagnosis. *Adv Drug Delivery Rev* 2002; 54(5): pp 631-651.
- 49 Brannon-Peppas L and Blanchette JO. Nanoparticle and targeted systems for cancer therapy. *Adv Drug Delivery Rev* 2004; 56(11): pp 1649-1659.
- 50 Bharali DJ, Khalil M, Gurbuz M, Simone TM and Mousa SA. Nanoparticles and cancer therapy: a concise review with emphasis on dendrimers. *Int J Nanomed* 2009; 4: pp 1-7. Available from: http://www.dovepress.com/articles.php?article_id=2803
- 51 Lammers T, Kiessling F, Hennink WE and Storm G. Drug targeting to tumors: principles, pitfalls and (pre-) clinical progress. *J Controlled Release* 2012; 161(2): pp 175-187.
- 52 Torchilin VP. Recent advances with liposomes as pharmaceutical carriers. *Nat Rev Drug Discovery* 2005; 4(2): pp 145-160.

- 53 Liechty WB and Peppas NA. Expert opinion: responsive polymer nanoparticles in cancer therapy. *Eur J Pharm Biopharm* 2012; 80(2): pp 241-246.
- 54 Torchilin VP. Micellar nanocarriers: pharmaceutical perspectives. *Pharm Res* 2007; 24(1): pp 1-16.
- 55 Bae Y and Kataoka K. Intelligent polymeric micelles from functional poly(ethylene glycol)-poly(amino acid) block copolymers. *Adv Drug Delivery Rev* 2009; 61(10): pp 768-784.
- 56 Blanco E, Kessinger CW, Sumer BD and Gao J. Multifunctional micellar nanomedicine for cancer therapy. *Exp Biol Med* 2009; 234(2): pp 123-131.
- 57 Gillies ER and Frechet JMJ. Dendrimers and dendritic polymers in drug delivery. *Drug Discovery Today* 2005; 10(1): pp 35-43.
- 58 Duncan R. The dawning era of polymer. *Nat Rev Drug Discovery* 2003; 2: pp 347-360.
- 59 Haag R and Kratz F. Polymer therapeutics: concepts and applications. *Angew Chem, Int Ed* 2006; 45(8): pp 1198-1215.
- 60 Lievre A, Bachet JB, Le Corre D, Boige V, Landi B, Emile JF, Cote JF, Tomasic G, Penna C and Ducreux M. KRAS mutation status is predictive of response to cetuximab therapy in colorectal cancer. *Cancer Res* 2006; 66(8): pp 3992-3995.
- 61 Aas T, Børresen AL, Geisler S, Smith-Sørensen B, Johnsen H, Varhaug JE, Akslen LA and Lønning PE. Specific P53 mutations are associated with de novo resistance to doxorubicin in breast cancer patients. *Nat Med* 1996; 2(7): pp 811-814.
- 62 Paez JG, Janne PA, Lee JC, Tracy S, Greulich H, Gabriel S, Herman P, Kaye FJ, Lindeman N and Boggon TJ. EGFR mutations in lung cancer: correlation with clinical response to gefitinib therapy. *Sci Signaling* 2004; 304(5676): pp 1497-1500.
- 63 Maeda H. The enhanced permeability and retention (EPR) effect in tumor vasculature: the key role of tumor-selective macromolecular drug targeting. *Adv Enzyme Regul* 2001; 41(1): pp 189-207.
- 64 Brown JM and Giaccia AJ. The unique physiology of solid tumors: opportunities (and problems) for cancer therapy. *Cancer Res* 1998; 58(7): pp 1408-1416.
- 65 Leu AJ, Berk DA, Lymboussaki A, Alitalo K and Jain RK. Absence of functional lymphatics within a murine sarcoma: a molecular and functional evaluation. *Cancer Res* 2000; 60(16): pp 4324-4327.
- 66 Padera TP, Stoll BR, Tooredman JB, Capen D, Di Tomaso E and Jain RK. Pathology: cancer cells compress intratumour vessels. *Nature* 2004; 427(6976): p 695.
- 67 Matsumura Y and Maeda H. A new concept for macromolecular therapeutics in cancer chemotherapy: mechanism of tumoritropic accumulation of proteins and the antitumor agent smancs. *Cancer Res* 1986; 46(12 Part 1): pp 6387-6392.
- 68 Duncan R. Polymer conjugates as anticancer nanomedicines. *Nat Rev Cancer* 2006; 6(9): pp 688-701.
- 69 Lammers T, Hennink WE and Storm G. Tumour-targeted nanomedicines: principles and practice. *Br J Cancer* 2008; 99(3): pp 392-397.
- 70 Maeda H. Tumor-selective delivery of macromolecular drugs via the EPR effect: background and future prospects. *Bioconjugate Chem* 2010; 21(5): pp 797-802.

- 71 Maeda H and Matsumura Y. EPR effect based drug design and clinical outlook for enhanced cancer chemotherapy. *Adv Drug Delivery Rev* 2011; 63(3): pp 129-130.
- 72 Maeda H, Wu J, Sawa T, Matsumura Y and Hori K. Tumor vascular permeability and the EPR effect in macromolecular therapeutics: a review. *J Controlled Release* 2000; 65(1): pp 271-284.
- 73 Maeda H, Bharate GY and Daruwalla J. Polymeric drugs for efficient tumor-targeted drug delivery based on EPR-effect. *Eur J Pharm Biopharm* 2009; 71(3): pp 409-419.
- 74 Torchilin V. Tumor delivery of macromolecular drugs based on the EPR effect. *Adv Drug Delivery Rev* 2011; 63(3): pp 131-135.
- 75 Duncan R and Gaspar R. Nanomedicine (s) under the Microscope. *Mol Pharmaceutics* 2011; 8(6): pp 2101-2141.
- 76 Acharya S and Sahoo SK. PLGA nanoparticles containing various anticancer agents and tumour delivery by EPR effect. *Adv Drug Delivery Rev* 2011; 63(3): pp 170-183.
- 77 Kwon G, Suwa S, Yokoyama M, Okano T, Sakurai Y and Kataoka K. Enhanced tumor accumulation and prolonged circulation times of micelle-forming poly (ethylene oxide-aspartate) block copolymer-adriamycin conjugates. *J Controlled Release* 1994; 29(1): pp 17-23.
- 78 Boucher Y, Kirkwood JM, Opacic D, Desantis M and Jain RK. Interstitial hypertension in superficial metastatic melanomas in humans. *Cancer Res* 1991; 51(24): pp 6691-6694.
- 79 Less JR, Posner MC, Boucher Y, Borochovit D, Wolmark N and Jain RK. Interstitial hypertension in human breast and colorectal tumors. *Cancer Res* 1992; 52(22): pp 6371-6374.
- 80 Jain RK and Stylianopoulos T. Delivering nanomedicine to solid tumors. *Nat Rev Clin Oncol* 2010; 7(11): pp 653-664.
- 81 Feng L and Mumper RJ. A Critical Review of Lipid-based Nanoparticles for Taxane Delivery. *Cancer Lett* 2013; 334(2): pp 157-175.
- 82 Fang J, Nakamura H and Maeda H. The EPR effect: Unique features of tumor blood vessels for drug delivery, factors involved, and limitations and augmentation of the effect. *Adv Drug Delivery Rev* 2011; 63(3): pp 136-151.
- 83 Duncan R, Ringsdorf H and Satchi-Fainaro R. Polymer therapeutics: Polymers as drugs, drug and protein conjugates and gene delivery systems: Past, present and future opportunities. *J Drug Targeting* 2006; 14(6): pp 337-341.
- 84 Vicent MJ, Ringsdorf H and Duncan R. Polymer therapeutics: clinical applications and challenges for development. *Adv Drug Delivery Rev* 2009; 61(13): pp 1117-1120.
- 85 Hirano T, Klesse W and Ringsdorf H. Polymeric derivatives of activated cyclophosphamide as drug delivery systems in antitumor chemotherapy. *Pharmacologically active polymers*, 20. *Die Makromolekulare Chemie* 1979; 180(4): pp 1125-1131.
- 86 Ringsdorf H. Structure and properties of pharmacologically active polymers. *J Polym Sci Pol Sym* 1975; 51(1): pp 135-153.
- 87 Ringsdorf H, Schlarb B and Venzmer J. Molecular architecture and function of polymeric oriented systems: models for the study of organization, surface recognition, and dynamics of biomembranes. *Angew Chem, Int Ed Engl* 1988; 27(1): pp 113-158.

- 88 Duncan R, Lloyd JB and Kopeček J. Degradation of side chains of N-(2-hydroxypropyl) methacrylamide copolymers by lysosomal enzymes. *Biochem Biophys Res Commun* 1980; 94(1): pp 284-290.
- 89 Duncan R and Kopeček J. Soluble synthetic polymers as potential drug carriers. In: *Polymers in Medicine*. Adv Polym Sci 57: Springer Berlin Heidelberg; 1984. pp 51-101. ISBN: 978-3-540-38740-4.
- 90 Duncan R, Cable HC, Lloyd JB, Rejmanova P and Kopeček J. Polymers containing enzymatically degradable bonds, 7. Design of oligopeptide side-chains in poly [N-(2-hydroxypropyl) methacrylamide] copolymers to promote efficient degradation by lysosomal enzymes. *Die Makromolekulare Chemie* 1983; 184(10): pp 1997-2008.
- 91 Kopeček J and Duncan R. Targetable polymeric prodrugs. *J Controlled Release* 1987; 6(1): pp 315-327.
- 92 Kopeček J and Bažilová H. Poly [N-(2-hydroxypropyl) methacrylamide] - I. Radical polymerization and copolymerization. *Eur Polym J* 1973; 9(1): pp 7-14.
- 93 Kopeček J. Controlled biodegradability of polymers – a key to drug delivery systems. *Biomaterials* 1984; 5(1): pp 19-25.
- 94 Ulbrich K, Koňák Č, Tuzar Z and Kopeček J. Solution properties of drug carriers based on poly [N-(2-hydroxypropyl) methacrylamide] containing biodegradable bonds. *Die Makromolekulare Chemie* 1987; 188(6): pp 1261-1272.
- 95 Ulbrich K, Strohalm J and Kopeček J. Poly (ethylene glycol)s containing enzymatically degradable bonds. *Die Makromolekulare Chemie* 1986; 187(5): pp 1131-1144.
- 96 Ulbrich K, Strohalm J and Kopeček J. Polymers containing enzymatically degradable bonds, 3. Poly [N-(2-hydroxypropyl) methacrylamide] chains connected by oligopeptide sequences cleavable by trypsin. *Die Makromolekulare Chemie* 1981; 182(7): pp 1917-1928.
- 97 Ulbrich K, Zacharieva EI, Kopeček J, Hume IC and Duncan R. Polymer-bound derivatives of sarcosyl and their antitumour activity against mouse and human leukaemia in vitro. *Die Makromolekulare Chemie* 1987; 188(11): pp 2497-2509.
- 98 Pasut G and Veronese FM. PEG conjugates in clinical development or use as anticancer agents: an overview. *Adv Drug Delivery Rev* 2009; 61(13): pp 1177-1188.
- 99 Pechar M, Braunova A, Ulbrich K, Jelínková M and Říhová B. Poly(ethylene glycol) - Doxorubicin conjugates with pH-controlled activation. *J Bioact Compat Polym* 2005; 20(4): pp 319-341.
- 100 Veronese FM, Schiavon O, Pasut G, Mendichi R, Andersson L, Tsirk A, Ford J, Wu G, Kneller S and Davies J. PEG-doxorubicin conjugates: influence of polymer structure on drug release, in vitro cytotoxicity, biodistribution, and antitumor activity. *Bioconjugate Chem* 2005; 16(4): pp 775-784.
- 101 Etrych T, Jelínková M, Říhová B and Ulbrich K. New HPMA copolymers containing doxorubicin bound via pH-sensitive linkage: synthesis and preliminary in vitro and in vivo biological properties. *J Controlled Release* 2001; 73(1): pp 89-102.
- 102 Chytil P, Etrych T, Koňák Č, Šírová M, Mrkvan T, Bouček J, Říhová B and Ulbrich K. New HPMA copolymer-based drug carriers with covalently bound hydrophobic substituents for solid tumour targeting. *J Controlled Release* 2008; 127(2): pp 121-130.

- 103 Lammers T, Kühnlein R, Kissel M, Šubr V, Etrych T, Pola R, Pechar M, Ulbrich K, Storm G and Huber P. Effect of physicochemical modification on the biodistribution and tumor accumulation of HPMA copolymers. *J Controlled Release* 2005; 110(1): pp 103-118.
- 104 Haag R, Sunder A and Stumbe JF. An approach to glycerol dendrimers and pseudo-dendritic polyglycerols. *J Am Chem Soc* 2000; 122(12): pp 2954-2955.
- 105 Calderon M, Quadir MA, Sharma SK and Haag R. Dendritic polyglycerols for biomedical applications. *Adv Mater* 2010; 22(2): pp 190-218.
- 106 Luxenhofer R, Han Y, Schulz A, Tong J, He Z, Kabanov AV and Jordan R. Poly (2-oxazoline)s as Polymer Therapeutics. *Macromol Rapid Commun* 2012; 33(19): pp 1613-1631.
- 107 Viegas TX, Bentley MD, Harris JM, Fang Z, Yoon K, Dizman B, Weimer R, Mero A, Pasut G and Veronese FM. Polyoxazoline: chemistry, properties, and applications in drug delivery. *Bioconjugate Chem* 2011; 22(5): pp 976-986.
- 108 Barz M, Luxenhofer R, Zentel R and Vicent MJ. Overcoming the PEG-addiction: well-defined alternatives to PEG, from structure–property relationships to better defined therapeutics. *Polym Chem* 2011; 2(9): pp 1900-1918.
- 109 Vicent MJ and Perez-Paya E. Poly-L-glutamic acid (PGA) aided inhibitors of apoptotic protease activating factor 1 (Apaf-1): An antiapoptotic polymeric nanomedicine. *J Med Chem* 2006; 49(13): pp 3763-3765.
- 110 Li C. Poly (L-glutamic acid)-anticancer drug conjugates. *Adv Drug Delivery Rev* 2002; 54(5): pp 695-713.
- 111 Pasut G and Veronese FM. Polymer-drug conjugation, recent achievements and general strategies. *Prog Polym Sci* 2007; 32(8): pp 933-961.
- 112 Abuchowski A, Van Es T, Palczuk NC and Davis FF. Alteration of immunological properties of bovine serum albumin by covalent attachment of polyethylene glycol. *J Biol Chem* 1977; 252(11): pp 3578-3581.
- 113 Moses MA, Brem H and Langer R. Advancing the field of drug delivery: taking aim at cancer. *Cancer Cell* 2003; 4(5): pp 337-341.
- 114 Reddy LH. Drug delivery to tumours: recent strategies. *J Pharm Pharmacol* 2005; 57(10): pp 1231-1242.
- 115 Malam Y, Loizidou M and Seifalian AM. Liposomes and nanoparticles: nanosized vehicles for drug delivery in cancer. *Trends Pharmacol Sci* 2009; 30(11): pp 592-599.
- 116 Ganta S, Devalapally H, Shahiwala A and Amiji M. A review of stimuli-responsive nanocarriers for drug and gene delivery. *J Controlled Release* 2008; 126(3): pp 187-204.
- 117 Mundargi RC, Babu VR, Rangaswamy V, Patel P and Aminabhavi TM. Nano/micro technologies for delivering macromolecular therapeutics using poly (D, L-lactide-co-glycolide) and its derivatives. *J Controlled Release* 2008; 125(3): pp 193-209.
- 118 Schädlich A, Caysa H, Mueller T, Rose C, Göpferich A, Kuntsche J and Mäder K. Tumor accumulation of NIR fluorescent PEG-PLA nanoparticles: Impact of particle size and human xenograft tumor model. *ACS nano* 2011; 5(11): pp 8710-8720.
- 119 Khandare J and Minko T. Polymer–drug conjugates: progress in polymeric prodrugs. *Prog Polym Sci* 2006; 31(4): pp 359-397.

- 120 Duncan R. Drug-polymer conjugates: potential for improved chemotherapy. *Anti-Cancer Drugs* 1992; 3(3): pp 175-210.
- 121 Ulbrich K and Šubr V. Polymeric anticancer drugs with pH-controlled activation. *Adv Drug Delivery Rev* 2004; 56(7): pp 1023-1050.
- 122 Vicent MJ and Duncan R. Polymer conjugates: nanosized medicines for treating cancer. *Trends Biotechnol* 2006; 24(1): pp 39-47.
- 123 Drobnik J. Biodegradable soluble macromolecules as drug carriers. *Adv Drug Delivery Rev* 1989; 3(2): pp 229-245.
- 124 Greco F and Vicent MJ. Combination therapy: opportunities and challenges for polymer-drug conjugates as anticancer nanomedicines. *Adv Drug Delivery Rev* 2009; 61(13): pp 1203-1213.
- 125 Vicent MJ, Greco F, Nicholson RI, Paul A, Griffiths PC and Duncan R. Polymer therapeutics designed for a combination therapy of hormone-dependent cancer. *Angew Chem, Int Ed* 2005; 44(26): pp 4061-4066.
- 126 Lammers T, Šubr V, Ulbrich K, Peschke P, Huber PE, Hennink WE and Storm G. Simultaneous delivery of doxorubicin and gemcitabine to tumors in vivo using prototypic polymeric drug carriers. *Biomaterials* 2009; 30(20): pp 3466-3475.
- 127 Duncan R. Development of HPMA copolymer-anticancer conjugates: clinical experience and lessons learnt. *Adv Drug Delivery Rev* 2009; 61(13): pp 1131-1148.
- 128 Gaspar R and Duncan R. Polymeric carriers: preclinical safety and the regulatory implications for design and development of polymer therapeutics. *Adv Drug Delivery Rev* 2009; 61(13): pp 1220-1231.
- 129 Gaspar R. Regulatory issues surrounding nanomedicines: setting the scene for the next generation of nanopharmaceuticals. *Nanomedicine* 2007; 2(2): pp 143-147.
- 130 Duncan R and Vicent MJ. Polymer Therapeutics-Prospects for 21st Century: The End of the Beginning. *Adv Drug Delivery Rev* 2013; 65(1): pp 60-70.
- 131 European Medicines Agency. Withdrawal assessment report for Opaxio; 2009. Doc.Ref.: EMEA/654674/2009.
Available from: http://www.ema.europa.eu/docs/en_GB/document_library/Application_withdrawal_assessment_report/2010/01/WC500060348.pdf
- 132 European Medicines Agency. Questions and answers on the withdrawal of the marketing authorisation application for Opaxio paclitaxel poliglumex; 2009. Doc. Ref.: EMEA/654674/2009.
Available from: http://www.ema.europa.eu/docs/en_GB/document_library/Medicine_QA/2010/01/WC500060347.pdf
- 133 Weissleder R. Molecular imaging in cancer. *Sci Signaling* 2006; 312(5777): pp 1168-1171.
- 134 Phelps ME. Positron emission tomography provides molecular imaging of biological processes. *Proc Natl Acad Sci* 2000; 97(16): pp 9226-9233.
- 135 Torigian DA, Huang SS, Houseni M and Alavi A. Functional imaging of cancer with emphasis on molecular techniques. *Ca-Cancer J Clin* 2007; 57(4): pp 206-224.
- 136 Quon A and Gambhir SS. FDG-PET and beyond: molecular breast cancer imaging. *J Clin Oncol* 2005; 23(8): pp 1664-1673.

- 137 Gambhir SS. Molecular imaging of cancer with positron emission tomography. *Nat Rev Cancer* 2002; 2(9): pp 683-693.
- 138 Beyer T, Townsend DW, Brun T, Kinahan PE, Charron M, Roddy R, Jerin J, Young J, Byars L and Nutt R. A combined PET/CT scanner for clinical oncology. *J Nucl Med* 2000; 41(8): pp 1369-1379.
- 139 Schillaci O. Hybrid SPECT/CT: a new era for SPECT imaging? *Eur J Nucl Med Mol Imaging* 2005; 32(5): pp 521-524.
- 140 Judenhofer MS, Wehrl HF, Newport DF, Catana C, Siegel SB, Becker M, Thielscher A, Kneilling M, Lichy MP and Eichner M. Simultaneous PET-MRI: a new approach for functional and morphological imaging. *Nat Med* 2008; 14(4): pp 459-465.
- 141 Pichler BJ, Kolb A, Nägele T and Schlemmer HP. PET/MRI: paving the way for the next generation of clinical multimodality imaging applications. *J Nucl Med* 2010; 51(3): pp 333-336.
- 142 Mariani G, Bruselli L, Kuwert T, Kim EE, Flotats A, Israel O, Dondi M and Watanabe N. A review on the clinical uses of SPECT/CT. *Eur J Nucl Med Mol Imaging* 2010; 37(10): pp 1959-1985.
- 143 Pleijhuis R, Crane L, van Oosten M, van Dam G and Ntziachristos V. Optical Imaging Applications in Cancer Research and Treatment. In: *Cancer - Cares Treatments and Preventions*. 1st ed. iConcept Press Ltd; 2013. ISBN: 978-1477554-99-9.
- 144 Ntziachristos V, Bremer C and Weissleder R. Fluorescence imaging with near-infrared light: new technological advances that enable in vivo molecular imaging. *Eur Radiol* 2003; 13(1): pp 195-208.
- 145 Weissleder R. A clearer vision for in vivo imaging. *Nat Biotechnol* 2001; 19(4): pp 316-317.
- 146 Leblond F, Davis SC, Valdes PA and Pogue BW. Pre-clinical whole-body fluorescence imaging: Review of instruments, methods and applications. *J Photochem Photobiol, B* 2010; 98(1): pp 77-94.
- 147 Frangioni JV. In vivo near-infrared fluorescence imaging. *Curr Opin Chem Biol* 2003; 7(5): pp 626-634.
- 148 Hebden JC, Arridge SR and Delpy DT. Optical imaging in medicine: I. Experimental techniques. *Phys Med Biol* 1997; 42(5): pp 825-840.
- 149 Mahmood U and Weissleder R. Near-infrared optical imaging of proteases in cancer. *Mol Cancer Ther* 2003; 2(5): pp 489-496.
- 150 Ale A, Ermolayev V, Deliolanis NC and Ntziachristos V. Fluorescence background subtraction technique for hybrid fluorescence molecular tomography/x-ray computed tomography imaging of a mouse model of early stage lung cancer. *J Biomed Opt* 2013; 18(5): p 056006.
- 151 Kunjachan S, Gremse F, Theek B, Koczera P, Pola R, Pechar M, Etrych T, Ulbrich K, Storm G and Kiessling F. Noninvasive optical imaging of nanomedicine biodistribution. *ACS nano* 2012; 7(1): pp 252-262.
- 152 Almutairi A, Akers WJ, Berezin MY, Achilefu S and Frechet JMJ. Monitoring the Biodegradation of Dendritic Near-Infrared Nanoprobes by in Vivo Fluorescence Imaging. *Mol Pharmaceutics* 2008; 5(6): pp 1103-1110.

- 153 Goutayer M, Dufort S, Josserand V, Royère A, Heinrich E, Vinet F, Bibette J, Coll JL and Texier I. Tumor targeting of functionalized lipid nanoparticles: assessment by in vivo fluorescence imaging. *Eur J Pharm Biopharm* 2010; 75(2): pp 137-147.
- 154 Schädlich A, Rose C, Kuntsche J, Caysa H, Mueller T, Göpferich A and Mäder K. How Stealthy are PEG-PLA Nanoparticles? An NIR In Vivo Study Combined with Detailed Size Measurements. *Pharm Res* 2011; 28: pp 1995-2007.
- 155 Schädlich A, Hoffmann S, Mueller T, Caysa H, Rose C, Göpferich A, Li J, Kuntsche J and Mäder K. Accumulation of nanocarriers in the ovary: A neglected toxicity risk? *J Controlled Release* 2012; 160: pp 105-112.
- 156 Poellinger A, Burock S, Grosenick D, Hagen A, Lüdemann L, Diekmann F, Engelken F, Macdonald R, Rinneberg H and Schlag PM. Breast cancer: early-and late-fluorescence near-infrared imaging with indocyanine green—a preliminary study. *Radiology* 2011; 258(2): pp 409-416.
- 157 Sevick-Muraca EM. Translation of near-infrared fluorescence imaging technologies: emerging clinical applications. *Annu Rev Med* 2012; 63: pp 217-231.
- 158 Erickson SJ, Martinez SL, DeCerce J, Romero A, Caldera L and Godavarty A. Three-dimensional fluorescence tomography of human breast tissues in vivo using a hand-held optical imager. *Phys Med Biol* 2013; 58(5): pp 1563-1579.
- 159 Corlu A, Choe R, Durduran T, Rosen MA, Schweiger M, Arridge SR, Schnall MD and Yodh AG. Three-dimensional in vivo fluorescence diffuse optical tomography of breast cancer in humans. *Opt Express* 2007; 15(11): pp 6696-6716.
- 160 O'Sullivan TD, Leproux A, Chen JH, Bahri S, Matlock A, Roblyer D, McLaren CE, Chen WP, Cerussi AE and Su MY. Optical imaging correlates with magnetic resonance imaging breast density and reveals composition changes during neoadjuvant chemotherapy. *Breast Cancer Res* 2013; 15(1): p R14.
Available from: <http://breast-cancer-research.com/content/15/1/R14>
- 161 Herranz M and Ruibal A. Optical Imaging in Breast Cancer Diagnosis: The Next Evolution. *J Oncol* 2012; 2012(863747).
Available from: <http://www.ncbi.nlm.nih.gov/pmc/articles/PMC3529498/>
- 162 Ishizawa T, Harada N, Muraoka A, Aoki T, Beck Y, Hasegawa K, Ijichi M, Kusaka K, Shibasaki M and Bandai Y. Scientific Basis and Clinical Application of ICG Fluorescence Imaging: Hepatobiliary Cancer. *The Open Surgical Oncology Journal* 2010; 2: pp 31-36.
- 163 Kokudo N and Ishizawa T. Clinical Application of Fluorescence Imaging of Liver Cancer Using Indocyanine Green. *Liver Cancer* 2012; 1(1): pp 15-21.
- 164 Werner SG. Implementierung, Standardisierung und Evaluierung einer neuen ICG-gestützten fluoreszenzoptischen Bildgebungstechnologie mit dem Xiralite-Verfahren zur Entzündungsdiagnostik bei rheumatischen Krankheitsbildern. Thesis (PhD). Berlin: Medizinischen Fakultät Charité - Universitätsmedizin Berlin, 2012.
Available from: http://www.diss.fu-berlin.de/diss/servlets/MCRFileNodeServlet/FUDISS_derivate_000000011007/diss_werner_sg_2012.pdf
- 165 Werner SG, Langer HE, Backhaus M and Horneff G. Fluoreszenzoptische Bildgebung mit dem Xiralite®-System in der Kinderrheumatologie. *Arthritis und Rheuma* 2006; 26(6): pp 364-368.
- 166 Werner SG, Langer HE, Ohrndorf S, Bahner M, Schott P, Schwenke C, Schirner M, Bastian H, Lind-Albrecht G and Kurtz B. Inflammation assessment in patients with arthritis using a

- novel in vivo fluorescence optical imaging technology. *Ann Rheum Dis* 2012; 71(4): pp 504-510.
- 167 Besheer A, Hertel TC, Kressler J, Mäder K and Pietzsch M. Enzymatically Catalyzed HES conjugation Using Microbial Transglutaminase: Proof of Feasibility. *J Pharm Sci* 2009; 98(11): pp 4420-4428.
- 168 Morita J, Nakatsuji H, Misaki T and Tanabe Y. Water-solvent method for tosylation and mesylation of primary alcohols promoted by KOH and catalytic amines. *Green Chem* 2005; 7(10): pp 711-715.
- 169 Schmitz KS. An introduction to dynamic light scattering of macromolecules. San Diego, CA (USA); Academic Press Inc.; 1990. ISBN: 978-0-12-627260-4.
Available from: <http://www.sciencedirect.com/science/book/9780126272604>
- 170 Berne BJ and Pecora R. Dynamic light scattering: with applications to chemistry, biology, and physics. 2003 ed. Mineola, NY: Courier Dover Publications; 1976. ISBN: 978-0486411552.
- 171 Lochmann A. Development and characterization of controlled delivery systems for rhBMP-2. Thesis (PhD). Halle, Germany: Martin-Luther-University Halle-Wittenberg, 2011.
Available from: <http://digital.bibliothek.uni-halle.de/hs/content/titleinfo/860684>
- 172 Anger S, Caldwell KD and Mueller RH. Charakterisierung von Makromolekülen, Kolloiden und Partikeln mit der Field-Flow Fractionation. *Pharm Ind* 2000; 62(2): pp 150-156.
- 173 Moldenhauer DCE and Klein T. Trennung und Charakterisierung von Proteinen, Polymeren und Partikeln. *GIT Laborzeitschrift* 2008; 6: pp 595-598.
- 174 Wahlund KG and Giddings JC. Properties of an asymmetrical flow field-flow fractionation channel having one permeable wall. *Anal Chem* 1987; 59(9): pp 1332-1339.
- 175 Yohannes G, Jussila M, Hartonen K and Riekkola ML. Asymmetrical flow field-flow fractionation technique for separation and characterization of biopolymers and bioparticles. *J Chromatogr, A* 2011; 1218(27): pp 4104-4116.
- 176 Augsten C and Mäder K. Characterizing molar mass distributions and molecule structures of different chitosans using asymmetrical flow field-flow fractionation combined with multi-angle light scattering. *Int J Pharm* 2008; 351(1): pp 23-30.
- 177 Lee S, Nilsson PO, Nilsson GS and Wahlund KG. Development of asymmetrical flow field-flow fractionation–multi angle laser light scattering analysis for molecular mass characterization of cationic potato amylopectin. *J Chromatogr, A* 2003; 1011(1): pp 111-123.
- 178 Viebke C and Williams PA. Determination of molecular mass distribution of κ -carrageenan and xanthan using asymmetrical flow field-flow fractionation. *Food Hydrocolloids* 2000; 14(3): pp 265-270.
- 179 Augsten C. Asymmetrische Fluß Feld-Fluß Fraktionierung in Verbindung mit Mehrwinkellichtstreuung - Eine neue bedeutende Methode der Pharmazeutischen Analytik zur Charakterisierung von Makromolekülen und Nanopartikeln. Thesis (PhD). Halle, Germany: Martin-Luther-University Halle-Wittenberg, 2008.
Available from: <http://sundoc.bibliothek.uni-halle.de/diss-online/08/08H117/>
- 180 Noack A. Development and characterization of curcuminoid-loaded lipid nanoparticles. Thesis (PhD). Halle, Germany: Martin-Luther-University Halle-Wittenberg, 2012.
Available from: <http://digital.bibliothek.uni-halle.de/hs/content/titleinfo/1380119>

- 181 Tenambergen F, Maruiama CH and Mäder K. Dual asymmetric centrifugation as an alternative preparation method for parenteral fat emulsions in preformulation development. *Int J Pharm* 2013; 447(1-2): pp 31-37.
- 182 Bock TK and Müller BW. A novel assay to determine the hemolytic activity of drugs incorporated in colloidal carrier systems. *Pharm Res* 1994; 11(4): pp 589-591.
- 183 Pape WJ, Pfannenbecker U and Hoppe U. Validation of the red blood cell test system as in vitro assay for the rapid screening of irritation potential of surfactants. *Mol Toxicol* 1987; 1(4): pp 525-536.
- 184 Kondo T and Tomizawa M. Hemolysis by nonionic surface-active agents. *J Pharm Sci* 1968; 57(7): pp 1246-1248.
- 185 Kirchherr AK, Briel A and Mäder K. Stabilization of Indocyanine Green by Encapsulation within Micellar Systems. *Mol Pharmaceutics* 2009; 6(2): pp 480-491.
- 186 Monographs on Dosage Forms: Parenteral Preparations. In: European Pharmacopoeia 7.8. Strasbourg: European Directorate for the Quality of Medicines & Health Care (EDQM); 2013. ISBN: 978-92-871-7222-8.
- 187 Euhus DM, Hudd C, Laregina MC and Johnson FE. Tumor measurement in the nude mouse. *J Surg Oncol* 1986; 31(4): pp 229-234.
- 188 Tomayko MM and Reynolds CP. Determination of subcutaneous tumor size in athymic (nude) mice. *Cancer Chemother Pharmacol* 1989; 24(3): pp 148-154.
- 189 Pygall SR, Whetstone J, Timmins P and Melia CD. Pharmaceutical applications of confocal laser scanning microscopy: The physical characterisation of pharmaceutical systems. *Adv Drug Delivery Rev* 2007; 59(14): pp 1434-1452.
- 190 Kutza C, Metz H, Kutza J, Syrowatka F and Mäder K. Towards a detailed characterization of oily adsorbates as "solid liquids". *Eur J Pharm Biopharm* 2012.
- 191 Oidtmann J. Mikroverkapselung von bioaktiven Inhaltsstoffen aus der Heidelbeere (*Vaccinium myrtillus* L.). Thesis (PhD). Halle, Germany: Martin-Luther-University Halle-Wittenberg, 2013.
Available from: <http://digital.bibliothek.uni-halle.de/hs/content/titleinfo/1446330>
- 192 Roos W. Confocal pH topography in plant cells: Shifts of proton distribution are involved in plant signalling. In: Rengel Z (editor). *Handbook of Plant Growth: pH as a Major Variable in Plant Growth*. 1st ed. New York: Marcel Dekker Inc.; 2002. pp 73-106. ISBN: 978-0-203-91034-4.
- 193 Kissel M, Peschke P, Šubr V, Ulbrich K, Schuhmacher J, Debus J and Friedrich E. Synthetic macromolecular drug carriers: biodistribution of poly [(N-2-hydroxypropyl) methacrylamide] copolymers and their accumulation in solid rat tumors. *PDA J Pharm Sci Technol* 2001; 55(3): pp 191-201.
- 194 Kopeček J and Kopečková P. HPMA copolymers: origins, early developments, present, and future. *Adv Drug Delivery Rev* 2010; 62(2): pp 122-149.
- 195 Lammers T and Ulbrich K. HPMA copolymers: 30 years of advances. *Adv Drug Delivery Rev* 2010; 62(2): pp 119-121.
- 196 Ulbrich K and Šubr V. Structural and chemical aspects of HPMA copolymers as drug carriers. *Adv Drug Delivery Rev* 2010; 62(2): pp 150-166.

- 197 Liu XM, Miller SC and Wang D. Beyond oncology - Application of HPMA copolymers in non-cancerous diseases. *Adv Drug Delivery Rev* 2010; 62(2): pp 258-271.
- 198 Dvorak M, Kopečková P and Kopeček J. High-molecular weight HPMA copolymer-adriamycin conjugates. *J Controlled Release* 1999; 60(2-3): pp 321-332.
- 199 Etrych T, Chytil P, Mrkvan T, Šírová M, Říhová B and Ulbrich K. Conjugates of doxorubicin with graft HPMA copolymers for passive tumor targeting. *J Controlled Release* 2008; 132(3): pp 184-192.
- 200 Arias L. Drug targeting strategies in cancer treatment: an overview. *Mini-Rev Med Chem* 2011; 11(1): pp 1-17.
- 201 Garnett MC. Targeted drug conjugates: principles and progress. *Adv Drug Delivery Rev* 2001; 53(2): pp 171-216.
- 202 Calderon M, Quadir MA, Strumia M and Haag R. Functional dendritic polymer architectures as stimuli-responsive nanocarriers. *Biochimie* 2010; 92(9): pp 1242-1251.
- 203 Chytil P, Etrych T, Kříž J, Šubr V and Ulbrich K. N-(2-Hydroxypropyl) methacrylamide-based polymer conjugates with pH-controlled activation of doxorubicin for cell-specific or passive tumour targeting. Synthesis by RAFT polymerisation and physicochemical characterisation. *Eur J Pharm Sci* 2010; 41(3): pp 473-482.
- 204 Šírová M, Mrkvan T, Etrych T, Chytil P, Rossmann P, Ibrahimova M, Kovář L, Ulbrich K and Říhová B. Preclinical Evaluation of Linear HPMA-Doxorubicin Conjugates with pH-Sensitive Drug Release: Efficacy, Safety, and Immunomodulating Activity in Murine Model. *Pharm Res* 2010; 27(1): pp 200-208.
- 205 Ulbrich K. Polymeric anticancer drugs with pH-controlled activation. *Adv Drug Delivery Rev* 2004; 56(7): pp 1023-1050.
- 206 Shen WC, Ryser HJ and LaManna L. Disulfide spacer between methotrexate and poly (D-lysine). A probe for exploring the reductive process in endocytosis. *J Biol Chem* 1985; 260(20): pp 10905-10908.
- 207 Thorpe PE, Wallace PM, Knowles PP, Relf MG, Brown AN, Watson GJ, Knyba RE, Wawrzynczak EJ and Blakey DC. New coupling agents for the synthesis of immunotoxins containing a hindered disulfide bond with improved stability in vivo. *Cancer Res* 1987; 47(22): pp 5924-5931.
- 208 Stern L, Perry R, Ofek P, Many A, Shabat D and Satchi-Fainaro R. A Novel Antitumor Prodrug Platform Designed to Be Cleaved by the Endoprotease Legumain. *Bioconjugate Chem* 2009; 20(3): pp 500-510.
- 209 Rejmanova P, Kopeček J, Pohl J, Baudys M and Kostka V. Polymers containing enzymatically degradable bonds, 8. Degradation of oligopeptide sequences in N (2 hydroxypropyl) methacrylamide copolymers by bovine spleen cathepsin B. *Die Makromolekulare Chemie* 1983; 184(10): pp 2009-2020.
- 210 Mrkvan T, Šírová M, Etrych T, Chytil P, Strohalm J, Plocová D, Ulbrich K and Říhová B. Chemotherapy based on HPMA copolymer conjugates with pH-controlled release of doxorubicin triggers anti-tumor immunity. *J Controlled Release* 2005; 110(1): pp 119-129.
- 211 Etrych T, Kovář L, Strohalm J, Chytil P, Říhová B and Ulbrich K. Biodegradable star HPMA polymer-drug conjugates: Biodegradability, distribution and anti-tumor efficacy. *J Controlled Release* 2011; 154(3): pp 241-248.

- 212 Svenson S and Tomalia DA. Dendrimers in biomedical applications--reflections on the field. *Adv Drug Delivery Rev* 2005; 57(15): pp 2106-2129.
- 213 Stiriba SE, Frey H and Haag R. Dendritic polymers in biomedical applications: from potential to clinical use in diagnostics and therapy. *Angew Chem, Int Ed* 2002; 41(8): pp 1329-1334.
- 214 Ulbrich K, Etrych T, Chytil P, Jelínková M and Říhová B. HPMA copolymers with pH-controlled release of doxorubicin: In vitro cytotoxicity and in vivo antitumor activity. *J Controlled Release* 2003; 87(1-3): pp 33-47.
- 215 Etrych T, Strohalm J, Chytil P, Černoch P, Starovoytova L, Pechar M and Ulbrich K. Biodegradable star HPMA polymer conjugates of doxorubicin for passive tumor targeting. *Eur J Pharm Sci* 2011; 42(5): pp 527-539.
- 216 Allmeroth MM, Moderegger D, Biesalski B, Koynov K, Rösch F, Thews OM and Zentel R. Modifying the body distribution of HPMA based copolymers by molecular weight and aggregate formation. *Biomacromolecules* 2011; 12(7): pp 2841-2849.
- 217 Lu ZR. Molecular imaging of HPMA copolymers: Visualizing drug delivery in cell, mouse and man. *Adv Drug Delivery Rev* 2010; 62(2): pp 246-257.
- 218 Seymour LW, Miyamoto Y, Maeda H, Brereton M, Strohalm J, Ulbrich K and Duncan R. Influence of molecular weight on passive tumour accumulation of a soluble macromolecular drug carrier. *Eur J Cancer* 1995; 31(5): pp 766-770.
- 219 Hoffmann S, Vystrčilová L, Ulbrich K, Etrych T, Caysa H, Mueller T and Mäder K. Dual Fluorescent HPMA Copolymers for Passive Tumour Targeting with pH-Sensitive Drug Release: Synthesis and Characterisation of Distribution and Tumour Accumulation in Mice by Noninvasive Multispectral Optical Imaging. *Biomacromolecules* 2012; 13(3): pp 652-663.
- 220 Storm G, Belliot SO, Daemen T and Lasic DD. Surface modification of nanoparticles to oppose uptake by the mononuclear phagocyte system. *Adv Drug Delivery Rev* 1995; 17(1): pp 31-48.
- 221 Gaur U, Sahoo SK, De TK, Ghosh PC, Maitra A and Ghosh PK. Biodistribution of fluoresceinated dextran using novel nanoparticles evading reticuloendothelial system. *Int J Pharm* 2000; 202(1-2): pp 1-10.
- 222 Lammers T, Šubr V, Ulbrich K, Hennink WE, Storm G and Kiessling F. Polymeric nanomedicines for image-guided drug delivery and tumor-targeted combination therapy. *Nano Today* 2010; 5(3): pp 197-212.
- 223 Seymour LW, Duncan R, Strohalm J and Kopeček J. Effect of molecular weight (Mw) of N (2 hydroxypropyl) methacrylamide copolymers on body distribution and rate of excretion after subcutaneous, intraperitoneal, and intravenous administration to rats. *J Biomed Mater Res* 1987; 21(11): pp 1341-1358.
- 224 Owens DE and Peppas NA. Opsonization, biodistribution, and pharmacokinetics of polymeric nanoparticles. *Int J Pharm* 2006; 307(1): pp 93-102.
- 225 Adams ML, Lavasanifar A and Kwon GS. Amphiphilic block copolymers for drug delivery. *J Pharm Sci* 2003; 92(7): pp 1343-1355.
- 226 Haraldsson B, Nyström J and Deen WM. Properties of the glomerular barrier and mechanisms of proteinuria. *Physiol Rev* 2008; 88(2): pp 451-487.

- 227 Vaupel P, Kallinowski F and Okunieff P. Blood flow, oxygen and nutrient supply, and metabolic microenvironment of human tumors: a review. *Cancer Res* 1989; 49(23): pp 6449-6465.
- 228 Schmidt M and Good RA. Transplantation of human cancers to nude mice and effects of thymus grafts. *J Natl Cancer Inst* 1975; 55: p 81.
- 229 Povlsen CO and Rygaard J. Heterotransplantation of human adenocarcinomas of the colon and rectum to the mouse mutant nude. A study of nine consecutive transplantations. *Acta Pathol Microbiol Scand , Sect A* 1971; 79(2): pp 159-169.
- 230 Killion JJ, Radinsky R and Fidler IJ. Orthotopic models are necessary to predict therapy of transplantable tumors in mice. *Cancer Metastasis Rev* 1998; 17(3): pp 279-284.
- 231 Wilmanns C, Fan D, O'Brian CA, Bucana CD and Fidler IJ. Orthotopic and ectopic organ environments differentially influence the sensitivity of murine colon carcinoma cells to doxorubicin and 5-fluorouracil. *Int J Cancer* 1992; 52(1): pp 98-104.
- 232 Kerbel RS. What is the optimal rodent model for anti-tumor drug testing? *Cancer Metastasis Rev* 1998; 17(3): pp 301-304.
- 233 Lee EM, Bachmann PS and Lock RB. Xenograft models for the preclinical evaluation of new therapies in acute leukemia. *Leuk Lymphoma* 2007; 48(4): pp 659-668.
- 234 Liu J, Bauer H, Callahan J, Kopečková P, Pan H and Kopeček J. Endocytic uptake of a large array of HPMA copolymers: Elucidation into the dependence on the physicochemical characteristics. *J Controlled Release* 2010; 143(1): pp 71-79.
- 235 Kreuter J. Nanoparticle-based drug delivery systems. *J Controlled Release* 1991; 16(1): pp 169-176.
- 236 Olszewski WL, Stanczyk M, Gewartowska M, Domaszewska-Szostek A and Durlík M. Lack of functioning intratumoral lymphatics in colon and pancreas cancer tissue. *Lymphatic Res Biol* 2012; 10(3): pp 112-117.
- 237 Schädlich A, Naolou T, Amado E, Schöps R, Kressler J and Mäder K. Non-invasive in vivo monitoring of the bio-fate of 195 kDa poly(vinyl alcohol) by multispectral fluorescence imaging. *Biomacromolecules* 2011; 12(10): pp 3674-3683.
- 238 Chytil P, Hoffmann S, Schindler L, Kostka L, Ulbrich K, Caysa H, Mueller T, Mäder K and Etrych T. Dual fluorescent HPMA copolymers for passive tumor targeting with pH-sensitive drug release II: Impact of release rate on biodistribution. *J Controlled Release* 2013; 172(2): pp 504-512.
- 239 Etrych T, Šubr V, Strohalm J, Šírová M, Říhová B and Ulbrich K. HPMA copolymer-doxorubicin conjugates: The effects of molecular weight and architecture on biodistribution and in vivo activity. *J Controlled Release* 2012; 164(3): pp 346-354.
- 240 Etrych T, Mrkvan T, Chytil P, Koňák Č, Říhová B and Ulbrich K. N-(2-hydroxypropyl)methacrylamide-based polymer conjugates with pH-controlled activation of doxorubicin. I. New synthesis, physicochemical characterization and preliminary biological evaluation. *J Appl Polym Sci* 2008; 109(5): pp 3050-3061.
- 241 Vanhoefer U, Cao S, Harstrick A, Seeber S and Rustum YM. Comparative antitumor efficacy of docetaxel and paclitaxel in nude mice bearing human tumor xenografts that overexpress the multidrug resistance protein (MRP). *Ann Oncol* 1997; 8(12): pp 1221-1228.

- 242 Trail PA, Willner D, Lasch SJ, Henderson AJ, Greenfield RS, King D, Zoeckler ME and Braslawsky GR. Antigen-specific activity of carcinoma-reactive BR64-doxorubicin conjugates evaluated in vitro and in human tumor xenograft models. *Cancer Res* 1992; 52(20): pp 5693-5700.
- 243 Meyer DL, Law KL, Payne JK, Mikolajczyk SD, Zarrinmayeh H, Jungheim LN, Kling JK, Shepherd TA and Starling JJ. Site-Specific Prodrug Activation by Antibody-. beta.-Lactamase Conjugates: Preclinical Investigation of the Efficacy and Toxicity of Doxorubicin Delivered by Antibody Directed Catalysis. *Bioconjugate Chem* 1995; 6(4): pp 440-446.
- 244 Rottenberg S, Nygren AO, Pajic M, van Leeuwen FW, van der Heijden I, van de Wetering K, Liu X, De Visser KE, Gilhuijs KG and Van Tellingen O. Selective induction of chemotherapy resistance of mammary tumors in a conditional mouse model for hereditary breast cancer. *Proc Natl Acad Sci* 2007; 104(29): pp 12117-12122.
- 245 Franz G. Polysaccharides in pharmacy. In: Dusek K (editor). *Pharmacy/Thermomechanics/Elastomers/Telechelics*. 1st ed. Springer; 1986. pp 1-30. ISBN: 978-3-540-15830-1.
- 246 Franz G. Polysaccharides in pharmacy: current applications and future concepts. *Planta Med* 1989; 55(6): pp 493-497.
- 247 Mizrahy S and Peer D. Polysaccharides as building blocks for nanotherapeutics. *Chem Soc Rev* 2012; 41(7): pp 2623-2640.
- 248 Goodarzi N, Varshochian R, Kamalinia G, Atyabi F and Dinarvand R. A review of polysaccharide cytotoxic drug conjugates for cancer therapy. *Carbohydr Polym* 2012; 92(2): pp 1280-1293.
- 249 Gibbs P, Clingan PR, Ganju V, Strickland AH, Wong SS, Tebbutt NC, Underhill CR, Fox RM, Clavant SP and Leung J. Hyaluronan-Irinotecan improves progression-free survival in 5-fluorouracil refractory patients with metastatic colorectal cancer: a randomized phase II trial. *Cancer Chemother Pharmacol* 2011; 67(1): pp 153-163.
- 250 Bowman HW. Clinical evaluation of dextran as a plasma volume expander. *J Am Med Assoc* 1953; 153(1): pp 24-26.
- 251 Lee Jr. WH, Cooper N, Weidner Jr. MG and Murner ES. Clinical evaluation of a new plasma expander, hydroxyethyl starch. *J Trauma* 1968; 8(3): pp 381-393.
- 252 Wöhl-Bruhn S, Badar M, Bertz A, Tiersch B, Koetz J, Menzel H, Mueller PP and Bunjes H. Comparison of In Vitro and In Vivo protein release from hydrogel systems. *J Controlled Release* 2012; 162(1): pp 127-133.
- 253 Wöhl-Bruhn S, Bertz A, Harling S, Menzel H and Bunjes H. Hydroxyethylstarch-based polymers for the controlled release of biomacromolecules from hydrogel microspheres. *Eur J Pharm Biopharm* 2012; 81(3): pp 573-581.
- 254 Noga M, Edinger D, Rödl W, Wagner E, Winter G and Besheer A. Controlled shielding and deshielding of gene delivery polyplexes using hydroxyethyl starch (HES) and alpha-amylase. *J Controlled Release* 2012; 159(1): pp 92-103.
- 255 Hey T, Knoller H and Vorstheim P. Half-Life Extension through HESylation. In: *Therapeutic Proteins: Strategies to Modulate Their Plasma Half-Lives*. Wiley Online Library; 2011. pp 117-140. ISBN: 3527644822.

- 256 Perner A, Haase N, Guttormsen AB, Tenhunen J, Klemenzson G, Åneman A, Madsen KR, Møller MH, Elkjær JM and Poulsen LM. Hydroxyethyl Starch 130/0.4 versus Ringer's acetate in severe sepsis. *N Engl J Med* 2012; 367(2): pp 124-134.
- 257 Navickis RJ, Haynes GR and Wilkes MM. Effect of hydroxyethyl starch on bleeding after cardiopulmonary bypass: A meta-analysis of randomized trials. *J Thorac Cardiovasc Surg* 2012; 144(1): pp 223-230.
- 258 Elinoff JM and Danner RL. Hydroxyethyl starch 130/0.42 increased death at 90 days compared with Ringer's acetate in severe sepsis. *Ann Intern Med* 2012; 157(8): pp JC4-JC6.
- 259 Sirtl C, Laubenthal H, Zumtobel V, Kraft D and Jurecka W. Tissue deposits of hydroxyethyl starch (HES): dose-dependent and time-related. *Br J Anaesth* 1999; 82(4): pp 510-515.
- 260 Christidis C, Mal F, Ramos J, Senejoux A, Callard P, Navarro R, Trinchet JC, Larrey D, Beaugrand M and Guettier C. Worsening of hepatic dysfunction as a consequence of repeated hydroxyethylstarch infusions. *J Hepatol* 2001; 35(6): pp 726-732.
- 261 Koch AE, Polverini PJ, Kunkel SL, Harlow LA, DiPietro LA, Elner VM, Elner SG and Strieter RM. Interleukin-8 as a macrophage-derived mediator of angiogenesis. *Science* 1992; 258(5089): pp 1798-1801.
- 262 Baggiolini M and Clark-Lewis I. Interleukin-8, a chemotactic and inflammatory cytokine. *FEBS Lett* 1992; 307(1): pp 97-101.
- 263 Lv R, Zhou W, Zhang LD and Xu JG. Effects of hydroxyethyl starch on hepatic production of cytokines and activation of transcription factors in lipopolysaccharide-administered rats. *Acta Anaesthesiol Scand* 2005; 49(5): pp 635-642.
- 264 Tian J, Lin X, Li YH and Xu JG. Influence of hydroxyethyl starch on lipopolysaccharide-induced tissue nuclear factor kappa B activation and systemic TNF- γ expression. *Acta Anaesthesiol Scand* 2005; 49(9): pp 1311-1317.
- 265 Collis RE, Collins PW, Gutteridge CN, Kaul A, Newland AC, Williams DM and Webb AR. The effect of hydroxyethyl starch and other plasma volume substitutes on endothelial cell activation; an in vitro study. *Intensive Care Med* 1994; 20(1): pp 37-41.
- 266 Vincent JL. The pros and cons of hydroxyethyl starch solutions. *Anesth Analg* 2007; 104(3): pp 484-486.
- 267 Brinkley M. A brief survey of methods for preparing protein conjugates with dyes, haptens and crosslinking reagents. *Bioconjugate Chem* 1992; 3(1): pp 2-13.
- 268 Besheer A. Nanomedicines based on modified hydroxyethyl starch: from synthesis to in vivo evaluation. Thesis (PhD). Halle, Germany: Martin-Luther-University Halle Wittenberg., 2009.
Available from: <http://digital.bibliothek.uni-halle.de/ulbhalhs/urn/urn:nbn:de:gbv:3:4-21>
- 269 Folta-Stogniew E and Williams K. Determination of molecular masses of proteins in solution: implementation of an HPLC size exclusion chromatography and laser light scattering service in a core laboratory. *J Biomol Tech* 1999; 10(2): pp 51-63.
- 270 Kulicke WM, Kaiser U, Schwengers D and Lemmes R. Measurements of the refractive index increment on hydroxyethyl starch as a basis for absolute molecular weight determinations. *Starch* 1991; 43(10): pp 392-396.

- 271 Bernstein SE. Physiological Characteristics. In: E.L.Green (editor). *Biology of the Laboratory Mouse*. 2nd revised ed. New York: Dover Publications, Inc; 1966.
Available from: <http://www.informatics.jax.org/greenbook/index.shtml>
- 272 Kulicke WM, Roessner D and Kull W. Characterization of hydroxyethyl starch by polymer analysis for use as a plasma volume expander. *Starch* 1993; 45(12): pp 445-450.
- 273 Treib J, Haass A, Pindur G, Seyfert UT, Treib W, Grauer MT, Jung F, Wenzel E and Schimrigk K. HES 200/0.5 is not HES 200/0.5. Influence of the C2/C6 hydroxyethylation ratio of hydroxyethyl starch (HES) on hemorheology, coagulation and elimination kinetics. *Thromb Haemostasis* 1995; 74(6): pp 1452-1456.
- 274 Ferber HP, Nitsch E and Förster H. Studies on hydroxyethyl starch. Part II: Changes of the molecular weight distribution for hydroxyethyl starch types 450/0.7, 450/0.5, 450/0.3, 300/0.4, 200/0.7, 200/0.5, 200/0.3 and 200/0.1 after infusion in serum and urine of volunteers. *Arzneim Forsch* 1985; 35(3): pp 615-622.
- 275 Nishikawa M, Kamijo A, Fujita T, Takakura Y, Sezaki H and Hashida M. Synthesis and Pharmacokinetics of A New Liver-Specific Carrier, Glycosylated Carboxymethyl-Dextran, and Its Application to Drug Targeting. *Pharm Res* 1993; 10(9): pp 1253-1261.
- 276 De Jong WH, Hagens WI, Krystek P, Burger MC, Sips AJAM and Geertsma RE. Particle size-dependent organ distribution of gold nanoparticles after intravenous administration. *Biomaterials* 2008; 29(12): pp 1912-1919.
- 277 Yoshida M, Amino M and Kishikawa T. A Study of Hydroxyethyl Starch. Long Pursuit of Hydroxyethyl Starch after Consecutive Infusions into Rabbits. *Starch* 1984; 36(7): pp 240-246.
- 278 Caysa H, Metz H, Mäder K and Mueller T. Application of Benchtop-magnetic resonance imaging in a nude mouse tumor model. *J Exp Clin Cancer Res* 2011; 30(1:69).
- 279 Matsubayashi R, Matsuo Y, Edakuni G, Satoh T, Tokunaga O and Kudo S. Breast Masses with Peripheral Rim Enhancement on Dynamic Contrast-enhanced MR Images: Correlation of MR Findings with Histologic Features and Expression of Growth Factors1. *Radiology* 2000; 217(3): pp 841-848.
- 280 Caysa H. Untersuchungen zum Monitoring von Tumorxenograftmodellen mittels nicht-invasivem in vivo Multispektral-Fluoreszenzimaging. Thesis (PhD). Halle, Germany: Martin-Luther-University Halle Wittenberg, 2013.
Available from: <http://digital.bibliothek.uni-halle.de/id/1630519>
- 281 Hoes CJT, Potman W, Van Heeswijk WAR, Mud J, De Grooth BG, Greve J and Feijen J. Optimization of macromolecular prodrugs of the antitumor antibiotic adriamycin. *J Controlled Release* 1985; 2: pp 205-213.
- 282 Zunino F, Pratesi G and Micheloni A. Poly (carboxylic acid) polymers as carriers for anthracyclines. *J Controlled Release* 1989; 10(1): pp 65-73.
- 283 Guan H, McGuire MJ, Li S and Brown KC. Peptide-targeted polyglutamic acid doxorubicin conjugates for the treatment of alpha(v)beta(6)-positive cancers. *Bioconjugate Chem* 2008; 19(9): pp 1813-1821.
- 284 Vega J, Ke S, Fan Z, Wallace S, Charsangavej C and Li C. Targeting doxorubicin to epidermal growth factor receptors by site-specific conjugation of C225 to poly (L-glutamic acid) through a polyethylene glycol spacer. *Pharm Res* 2003; 20(5): pp 826-832.

- 285 Milas L, Mason KA, Hunter N, CHUN LI and Wallace S. Poly (L-glutamic acid)-paclitaxel conjugate is a potent enhancer of tumor radiocurability. *Int J Radiat Oncol, Biol, Phys* 2003; 55(3): pp 707-712.
- 286 Zou C, Brewer M, Cao X, Zang R, Lin J, Deng Y and Li C. Antitumor activity of 4-(N-hydroxyphenyl) retinamide conjugated with poly (L-glutamic acid) against ovarian cancer xenografts. *Gynecol Oncol* 2007; 107(3): pp 441-449.
- 287 Chipman SD, Oldham FB, Pezzoni G and Singer JW. Biological and clinical characterization of paclitaxel poliglumex (PPX, CT-2103), a macromolecular polymer-drug conjugate. *Int J Nanomed* 2006; 1(4): pp 375-383.
- 288 Li C and Wallace S. Polymer-drug conjugates: recent development in clinical oncology. *Adv Drug Delivery Rev* 2008; 60(8): pp 886-898.
- 289 Herzog T, Barret RJ, Edwards R and Oldham FB. Phase II study of paclitaxel poliglumex (PPX)/carboplatin (C) for 1st line induction and maintenance therapy of stage III/IV ovarian or primary peritoneal carcinoma. *ASCO Annual Meeting Proceedings J Clin Oncol* 2005; 23(16S): p 5012.
- 290 Singer JW. Paclitaxel poliglumex (XYOTAX™, CT-2103): a macromolecular taxane. *J Controlled Release* 2005; 109(1): pp 120-126.
- 291 Dipetrillo T, Milas L, Evans D, Akerman P, Ng T, Miner T, Cruff D, Chauhan B, Iannitti D and Harrington D. Paclitaxel poliglumex (PPX-Xyotax) and concurrent radiation for esophageal and gastric cancer: a phase I study. *Am J Clin Oncol* 2006; 29(4): pp 376-379.
- 292 O'Brien ME, Socinski MA, Popovich AY, Bondarenko IN, Tomova A, Bilynsky BT, Hotko YS, Ganul VL, Kostinsky IY and Eisenfeld AJ. Randomized phase III trial comparing single-agent paclitaxel Poliglumex (CT-2103, PPX) with single-agent gemcitabine or vinorelbine for the treatment of PS 2 patients with chemotherapy-naive advanced non-small cell lung cancer. *J Thorac Oncol* 2008; 3(7): pp 728-734.
- 293 Cell Therapeutics Inc.: 2012 Annual Report. 2013. Available from: <http://www.celltherapeutics.com>
- 294 Joyce J, Cook J, Chabot D, Hepler R, Shoop W, Xu Q, Stambaugh T, Aste-Amezaga M, Wang S and Indrawati L. Immunogenicity and protective efficacy of Bacillus anthracis poly-D-glutamic acid capsule covalently coupled to a protein carrier using a novel triazine-based conjugation strategy. *J Biol Chem* 2006; 281(8): pp 4831-4843.
- 295 Zimmermann R, Osaki T, Kratzmüller T, Gauglitz G, Dukhin SS and Werner C. Electrostatic switching of biopolymer layers. insights from combined electrokinetics and reflectometric interference. *Anal Chem* 2006; 78(16): pp 5851-5857.
- 296 Joshi A, Saraph A, Poon V, Mogridge J and Kane RS. Synthesis of potent inhibitors of anthrax toxin based on poly-L-glutamic acid. *Bioconjugate Chem* 2006; 17(5): pp 1265-1269.
- 297 Tomimatsu Y, Vitello L and Gaffield W. Effect of aggregation on the optical rotatory dispersion of poly (-L-glutamic acid). *Biopolymers* 1966; 4(6): pp 653-662.
- 298 Hermanson GT. *Bioconjugate Techniques*. 1st ed. Elsevier Science Publishing Company, Inc.; 1996. ISBN: 978-0-12-342335-1.

5.3 Publications

5.3.1 Peer Reviewed Articles

- **Hoffmann S**, Vystrčilová L, Ulbrich K, Etrych T, Caysa H, Mueller T and Mäder K. Dual fluorescent HPMA copolymers for passive tumor targeting with pH-sensitive drug release: synthesis and characterization of distribution and tumor accumulation in mice by non-invasive multispectral optical imaging. Biomacromolecules 2012; 13(3): pp. 652–663.
- **Hoffmann S**, Caysa H, Kuntsche J, Kreideweiß P, Leimert A, Mueller T and Mäder K. Carbohydrate plasma expanders for passive tumor targeting: *In vitro and in vivo* studies. Carbohydrate Polymers 2013; 95(1): pp. 404-413.
- Schädlich A, **Hoffmann S**, Mueller T, Caysa H, Rose C, Göpferich A, Li J, Kuntsche J and Mäder K. Accumulation of nanocarriers in the ovary: A neglected toxicity risk? Journal of Controlled Release 2012; 160(1): pp. 105–112.
- Caysa H, **Hoffmann S**, Luetzkendorf J, Mueller LP, Unverzagt S, Mäder K and Mueller T. Monitoring of xenograft tumor growth and response to chemotherapy by non-invasive in vivo multispectral fluorescence imaging. PLoS One 2012; 7(10): e47927.
- Chytil P, **Hoffmann S**, Schindler L, Kostka L, Ulbrich K, Caysa H, Mueller T, Mäder K and Etrych T. Dual fluorescent HPMA copolymers for passive tumor targeting with pH-sensitive drug release II: Impact of release rate on biodistribution. Journal of Controlled Release 2013; 172(2): pp. 504-512.

5.3.2 Quotable Abstracts

- **Hoffmann S**, Vystrčilová L, Ulbrich K, Etrych T, Caysa H, Mueller T and Mäder K. HPMA copolymer drug conjugates with pH-sensitive release: Non-invasive and simultaneous characterization of carrier and drug model biodistribution and tumor accumulation in mice by use of in vivo multispectral optical imaging. In: Polymers in Medicine 2012; ISBN 978-80-85009-72-9 (2012).

5.3.3 Conference Contributions

- **Hoffmann S**, Schädlich A, Caysa H, Mueller T and Mäder K. In vivo characterization of high molecular weight hydroxyethyl starch using non-invasive fluorescence imaging. 8th International Symposium on Polymer Therapeutics: From Laboratory to Clinical Practice, Valencia (Spain) 2010. (Poster & oral presentation)
- **Hoffmann S**, Schädlich A, Caysa H, Mueller T and Mäder K. Plasma volume expanders as potential drug delivery systems – An in vivo study utilizing non-invasive near infrared fluorescence optical imaging. DPhG Jahrestagung, Braunschweig (Germany) 2010. (Poster)
- **Hoffmann S**, Schädlich A, Caysa H, Mueller T and Mäder K. HES 450 as potential drug delivery system for passive tumor targeting: An in vivo study in nude mice using near infrared optical imaging. European Summerschool in Nanomedicine, Wittenberg (Germany) 2011. (Poster)
- Kutza J, **Hoffmann S**, Noack A and Mäder K. A New Model system for the investigation of in-vitro drug release from hydrophilic polymerbased gels, nanoparticles and water soluble polymers by multispectral fluorescence imaging. European Summerschool in Nanomedicine, Wittenberg (Germany) 2011. (Poster)
- Vystrčilová L, Etrych T and **Hoffmann S**. High-molecular-weight polymer drug carriers for cancer treatment and imaging. European Summerschool in Nanomedicine, Wittenberg (Germany) 2011. (Poster)
- Vystrčilová L, Etrych T, **Hoffmann S**, Mäder K and Ulbrich K. Dual fluorescently labeled polymer carriers for in vivo visualisation of biodistribution. 12th European Symposium on Controlled Drug Delivery, Egmond aan Zee (Netherlands) 2012. (Poster)
- Caysa H, **Hoffmann S**, Mueller T, and Mäder K. Anwendung von Fluoreszenzfarbstoffen zur Charakterisierung moderner Arzneiformen unter Einbeziehung präklinischer in vivo Mausmodelle Innovationsforum - „Funktionelle Farbstoffe - Innovation in Medizin und Technik“, Bitterfeld-Wolfen (Germany) 2012. (Poster)

- **Hoffmann S**, Vystrčilová L, Ulbrich K, Etrych T, Caysa H, Mueller T and Mäder K. Tumor targeted delivery of polymer drug conjugates with pH-sensitive release: monitoring the biodistribution of carriers and drug model simultaneously by multispectral optical imaging. 9th International Symposium on Polymer Therapeutics: From Laboratory to Clinical Practice, Valencia (Spain) 2012. (Poster & oral presentation).
AWARDED with "Polymer Chemistry Award".
- **Hoffmann S**, Vystrčilová L, Ulbrich K, Etrych T, Caysa H, Mueller T and Mäder K. HPMA copolymer drug conjugates with pH-sensitive release. 76th Prague Meeting on Macromolecules: Polymers in Medicine, Prague (Czech Republic) 2012. (Oral presentation)
- Schädlich A, **Hoffmann S**, Mueller T, Caysa H and Mäder K: Is the accumulation of nanocarriers in the ovary a common phenomenon? 76th Prague Meeting on Macromolecules: Polymers in Medicine, Prague (Czech Republic) 2012. (Poster)
- England RM, Duro Castaño A, Conejos-Sánchez I, **Hoffmann S**, Mäder K and Vicent MJ. Well-defined polyglutamates with versatile architectures. MacroGroup UK International Conference on Polymer Synthesis, Warwick (UK) 2012. (Poster)
- **Hoffmann S**, Caysa H, Vystrčilová L, Ulbrich K, Etrych T, Mueller T and Mäder K. Polymers as promising drug carrier systems for targeted tumor therapy - in vitro characterization and in vivo analyzes. 15th International Conference "Polymeric Materials", Halle (Germany) 2012. (Poster)
- Caysa H, **Hoffmann S**, Luetzkendorf J, Mueller LP, Unverzagt S, Mäder K and Mueller T. Analysis of xenograft tumor growth, metastasis and therapy response by in vivo fluorescence imaging. Forschen im Verbund – Forschungstag 2012, UKH Halle (Germany) 2012. (Poster)

5.4 Acknowledgements

This work would not have been possible without the help, assistance and encouragement of many persons and I am firmly convinced that scientific work is impossible without cooperation and support of others. First of all, I would like to thank Professor Dr. Karsten Mäder for the opportunity to join his group and to work in such an interesting and challenging field of science. He ever was - and still is - an excellent and valuable mentor to me. Thank you, for your enduring assistance and never-ending trust in my work.

I very much want to acknowledge the work of all cooperation partners. Certainly they have contributed a great share to this work, but moreover they taught me about science. Special thanks are addressed to Tomáš Etrych (PhD), Lucie Schindler, Petr Chytil (PhD) and Prof. Karel Ulbricht (Dr.Sc.) from the IMC in Prague and to Fabiana Canal (PhD), Richard England (PhD) and Maria Vicent (PhD) for the synthesis of many polymers used in this work. Dr. Thomas Mueller and Dr. Henrike Caysa have a great share in all *in vivo* experiments and without their steady hands no mouse would have been intravenously injected within this work. Of inestimable value in this context were also Constanze Gottschalk, Martina Hennicke and Dr. Bernhard Hiebl, continuously caring for the welfare of my laboratory animals.

Furthermore I thank Anja Leimert and Patrick Kreideweiß for their assistance in the *in vitro* toxicity experiments, Hauke Lilie for the analytical ultracentrifugation, the group of Dr. Ströhl for NMR-measurements, Prof. Dr. Thomas Groth and Jürgen Vogel for the possibility to do the CLSM measurements and Erik Borski and Johannes Stelzner for donating their blood for my purposes. Johannes Stelzner earned special gratitude for being my diploma student and taking care for some research issues. Thank you for our fruitful discussions. Also Anne-Kathrin Heinrich shall not be forgotten, who joined the group at my very last weeks and nonetheless was a very precious help, taking over my last practical course and finishing the very last experiments. Mentioning the practical course I have to remember Juliane Frank and Claudia Kegel; it was always a pleasure and joy teaching the students with you. The Deutsche Forschungsgemeinschaft is acknowledged for financial Support (MA1648/7-1 and LSM:INST271/250-1). As a matter of fact this work would not have been possible without financial support. The Serumwerk Bernburg AG is acknowledged for the kind provision of carbohydrates.

A special thank goes to all members of the group of Professor Dr. Karsten Mäder. I will never forget the great atmosphere during lunchtime or our “class trips” and I doubt that something like that would be possible without you ever again. Very particular thanks go to Ute Mentzel for her continuous laboratory assistance and to Claudia Bertram, whose door was always open for me and who was always taking care for so many things for me. Further, I want to thank Martin Windorf, Dr. Hendrik Metz and Dr. Sabine Kempe for the fruitful discussions of my results, for the creativity and helpfulness. I also gratefully want to mention Dr. Andreas Schädlich, for his help getting started in my subject and the many inspiring discussions. Finally I want to thank Dr. Sabine Kempe, Dr. Henrike Caysa and Dr. Matthias Gundermann for their valuable corrections of the preliminary version of this thesis. I am deeply indebted for your diligent and meticulous help

Ultimately, I want to express my deep gratitude to my dear wife and my family, who supported me tirelessly on my way, always accepting the obligations I had. Without their strong backup I likely would have tumbled. And for one thing we must not forget: the greatest and most marvelous *in vivo* result are you, FJ.

5.5 Curriculum Vitae

Persönliche Daten

Name	Stefan Hoffmann
Geburtsdatum	15. November 1984
Geburtsort	Halle (Saale)

Ausbildung und Berufliche Entwicklung

Seit 11/2013	Wissenschaftlicher Mitarbeiter am Institut für Pharmazie der Martin-Luther-Universität Halle Wittenberg.
06/2013-10/2013	Wissenschaftlicher Mitarbeiter in der Arzneimittelsicherheit bei mibe GmbH Arzneimittel in Sandersdorf-Brehna
03/2010-11/2012	Teilzeittätigkeit als angestellter Apotheker (Chefvertretung) in der Apotheke im Magistralen-Carré in Halle
12/2009-05/2013	Wissenschaftlicher Mitarbeiter am Institut für Pharmazie der Martin-Luther-Universität Halle Wittenberg.
12/2009	Approbation zum Apotheker
11/2009	Dritter Abschnitt der Pharmazeutischen Prüfung (3. Examen)
05/2009-10/2009	Pharmaziepraktikant in der Detharding-Apotheke, Warnemünde
11/2008-04/2009	Diplomarbeit in der AG Pharmazeutische Technologie der Martin-Luther-Universität (Dipl.-Pharm.)
10/2008	Zweiter Abschnitt der Pharmazeutischen Prüfung (2. Examen)
09/2006	Praktikum bei Boehringer Ingelheim Pharma GmbH & Co. KG, Abteilung Quality Control in Ingelheim
09/2006	Erster Abschnitt der Pharmazeutischen Prüfung (1. Examen)
2004-2008	Pharmaziestudium in an der Martin-Luther-Universität in Halle
07/2004	Abitur an der Latina August Hermann Francke in Halle

5.6 Declaration of Original Authorship

Selbstständigkeitserklärung

Hiermit erkläre ich an Eides statt, dass ich die vorgelegte Arbeit selbstständig und ohne fremde Hilfe verfasst habe. Die Ergebnisse dieser Arbeit wurden unter Anleitung von Herrn Professor Dr. rer. nat. habil. Karsten Mäder selbstständig erarbeitet.

Weiterhin habe ich keine anderen als die angegebenen Quellen und Hilfsmittel verwendet und inhaltlich oder wörtlich übernommene Stellen als solche kenntlich gemacht. Beiträge von Kooperationspartnern zu den Ergebnissen dieser Arbeit habe ich eindeutig gekennzeichnet. Ich respektiere die Grundsätze guter wissenschaftlicher Praxis der DFG und habe keinerlei Daten gefälscht.

Ich habe bisher noch keine Promotionsversuche unternommen und diese Arbeit wurde keiner anderen Fakultät vorgelegt.

Halle (Saale), 10.01.2014

Ort, Datum

sgd. Stefan Hoffmann

Stefan Hoffmann